Summer 7-1-2017

High Precision Refractive Index Measurement Techniques Applied to the Analysis of Neutron Damage and Effects in CaF2 Crystals

Joseph P. Morris Ph.D.
University of New Mexico

Recommended Citation

Morris, Joseph P. Ph.D.. "High Precision Refractive Index Measurement Techniques Applied to the Analysis of Neutron Damage and Effects in CaF2 Crystals." (2017). https://digitalrepository.unm.edu/ne_etds/63

Joseph Paul Morris

Candidate

Nuclear Engineering

Department

This dissertation is approved, and it is acceptable in quality and form for publication:

Approved by the Dissertation Committee:

Adam Hecht, Ph.D., Chairperson

Gary Cooper, Ph.D.

Cassiano de Oliveira, Ph.D.

Jean-Claude Diels, Ph.D.

HIGH PRECISION REFRACTIVE INDEX MEASUREMENT TECHNIQUES APPLIED TO THE ANALYSIS OF NEUTRON DAMAGE AND EFFECTS IN CAF$_2$ CRYSTALS

by

JOSEPH PAUL MORRIS

B.S. Electrical Engineering, Ohio University, 2010
M.S. Optoelectronic Engineering, Ohio University, 2012

DISSERTATION

Submitted in Partial Fulfillment of the
Requirements for the Degree of

Doctor of Philosophy
Engineering

The University of New Mexico
Albuquerque, New Mexico

July, 2017

DEDICATION

To the Lord over all the Earth, and Savior of Mankind, Christ Jesus

"And whatsoever ye do, do it heartily, as to the Lord, and not unto men; Knowing that of the Lord ye shall receive the reward of the inheritance: for ye serve the Lord Christ."
Colossians 3:23-24

"Jesus saith unto him, I am the way, the truth and the life: no man cometh unto the Father, but by me."
John 14:6

"That if thou shalt confess with thy mouth the Lord Jesus, and shalt believe in thine heart that God hath raised him from the dead, thou shalt be saved."
Romans 10:9

ACKNOWLEDGEMENTS

Above all I am most grateful to the Lord and Savior of the world Christ Jesus for the sacrifice He made to give all life purpose and meaning. Without that sacrifice all the work I have completed here would be a vain attempt on my part to give myself meaning and purpose. He has blessed my family beyond measure during my time at the University of New Mexico. He has taught me, most importantly, to emulate and display the love and passion He has for all the people on Earth. I will continue to move forward offering my work and all that I am as a living sacrifice to Him, for He is worthy of all that I can give.

I bestow thanks upon Dr. Adam Hecht, who has served as my graduate advisor. He has provided valuable direction and resources necessary to completing this work. He has also provided many challenges along the way that I am grateful for. Additionally, I would like to thank the other members of my dissertation committee, Dr. Gary Cooper, Dr. Cassiano de Oliveira, and Dr. Jean-Claude Diels. Their technical knowledge and expertise has aided me in many ways during the pursuit of my doctorate degree.

I acknowledge the support of the Department of Energy, Nuclear Universities Consortium, and the INL-LDRD, Award Number: 0145662 Release No. 007. Additionally, I am grateful to the Department of Defense SMART scholarship program for educational funding and the Air Force Nuclear Weapons Center for supporting this pursuit. I would also like to acknowledge collaborative support of Maria Okuniewski, Sebastien Teysseyre of Idaho National Laboratory, and the Center for Advance Computing Research at the University of New Mexico.

I grant special recognition to James Hendrie. James was the cornerstone of the laser physics aspect of this work and is deserving of great thanks. Additionally, Sara Pelka was a crucial member of the research team and her assistance was greatly valued. I also bestow thanks upon Major Jon Rowland, a true friend, who provided encouragement, expertise, and prayer on my behalf.

I am deeply grateful for mother, Katherine Morris, late father, Dennis Morris. I am thankful to my sisters, brothers-in-law, and sister-in-law, Jeff and Bethany Buckner, Randy and April Massie, Michael and Linda Lacey, and Jessica Heim, as well as my father and mother-in-law, Walter and Beverly Heim. I am also grateful to my friends Tucker and Brittnee Barlow, grandparents-in-law Tom and Jeannie Heim, and many other family and friends for their continued support and prayer.

I would especially like to thank my beautiful wife and wonderful children, Rachel Morris, James, Isaiah, and John, for their continual love, support, and inspiration throughout all the areas of my life. Rachel was beyond gracious and self-sacrificing in my pursuit of this degree. She was extremely helpful in diagnosing some inconsistencies and difficulties in my work while inspiring me to emulate Christ more and more.

HIGH PRECISION REFRACTIVE INDEX MEASUREMENT TECHNIQUES APPLIED TO THE ANALYSIS OF NEUTRON DAMAGE IN CAF$_2$ CRYSTALS

by

Joseph Paul Morris

B.S. Electrical Engineering, Ohio University, 2010
M.S. Optoelectronic Engineering, Ohio University, 2012
Ph.D. Engineering, University of New Mexico, 2017

ABSTRACT

Neutron irradiation damages material by atomic displacements. The majority of these damage regions are microscopic and difficult to study, though they can cause a change in density and thus a change in refractive index in transparent materials. This work utilized CaF$_2$ crystals to track refractive index change based on neutron radiation dose. High precision refractive index measurements were performed utilizing a nested-cavity mode-locked laser where the CaF$_2$ crystal acted as a Fabry-Pérot Etalon (FPE). By comparing the repetition rate of the cavity and the repetition rate of the FPE, refractive index change was determined. Following several irradiation experiments, the change in refractive index was measured to examine correlation between dose and the change in refractive index.

An examination of the causal effects behind refractive index change was also performed by molecular dynamics simulations, leading to a statistical determination of the threshold displacement energy (TDE) in a CaF$_2$ crystal lattice. Additionally, damage cascade analysis suggests that the number of atomic displacements and vacancies caused by neutron irradiation increases linearly as a function of incident neutron energy.

Simulations were performed for a Primary Knock-on Atom (PKA) energy range of 100 eV to 5 keV, which was the upper limit of the computing constraints for this work. This finding is in line with the irradiation induced refractive index change theory for crystalline solids.

Light irradiation of crystalline solids was performed demonstrating noticeable trends in the change of refractive index when correlated to absorbed dose. Unfortunately, due to uncertainties in the data caused by several unknown factors, higher dose irradiations must be performed to confirm the trend. This type of experimental measurement of microscopic damage in the bulk of the material through the refractive index will supports several potential applications. This technique may be adopted and modified for dosimetry applications as well as being utilized as a nondestructive method for understanding microscopic neutron damage in bulk materials.

Table of Contents

List of Figures

List of Tables

Chapter 1: Introduction

1.1 Motivation

Neutron irradiation can cause atomic displacements (damage) in a material, which in turn, can cause swelling or compaction. This effect does not occur for gamma irradiation at typical reactor energies. This swelling or compaction causes a change in density, which manifests itself in transparent materials as a change in refractive index and can be measured. The great majority of the damage from neutron irradiation occurs in microscopic displacements, and these displacements account for the majority of the large-scale radiation effects. These displacements are difficult to measure through traditional methods [1], and are especially difficult to measure nondestructively in the bulk of the material. The primary goal of this work is to apply techniques for very high precision refractive index measurements to crystals that have been irradiated, towards using this technique as a mode of understanding radiation damage and dose through the material. This allows for a nondestructive assessment of radiation effects in a material that may be used to improve damage models. This may also open the door for a family of new materials for radiation detection, measurement, and dosimetry. Ultimately the hope of this effort is to demonstrate a novel technology that will enable high precision dosimetry in real time harsh radiation environments.

1.2 Overview

The work described in this dissertation is focused on material damage, effects, and refractive index change due to neutron irradiation of Calcium Fluoride, CaF_2. This work was completed utilizing modeling, simulation, and experimental analysis. The focus of the modeling and simulation aspects is the cultivation of an understanding of damage propagation within CaF_2. By extracting the Threshold Displacement Energy (TDE) of Ca and F atoms and modeling the damage cascades this work will inform future analysis linking large-scale property changes such as refractive index and density to these small-scale damage cascades. This is extremely important as most radiation induced effects of material properties are caused by microscopic defects [1], and defects below 5 nm are responsible for most the changes in material properties [2]. This is further exhibited by Sand *et al*. where it is shown that the frequency of defects generated per ion follows a power law in which the vast majority of defects impacting the material are microscopic and too small to detect visually [3] [4], as shown in Figure 1.2.1.

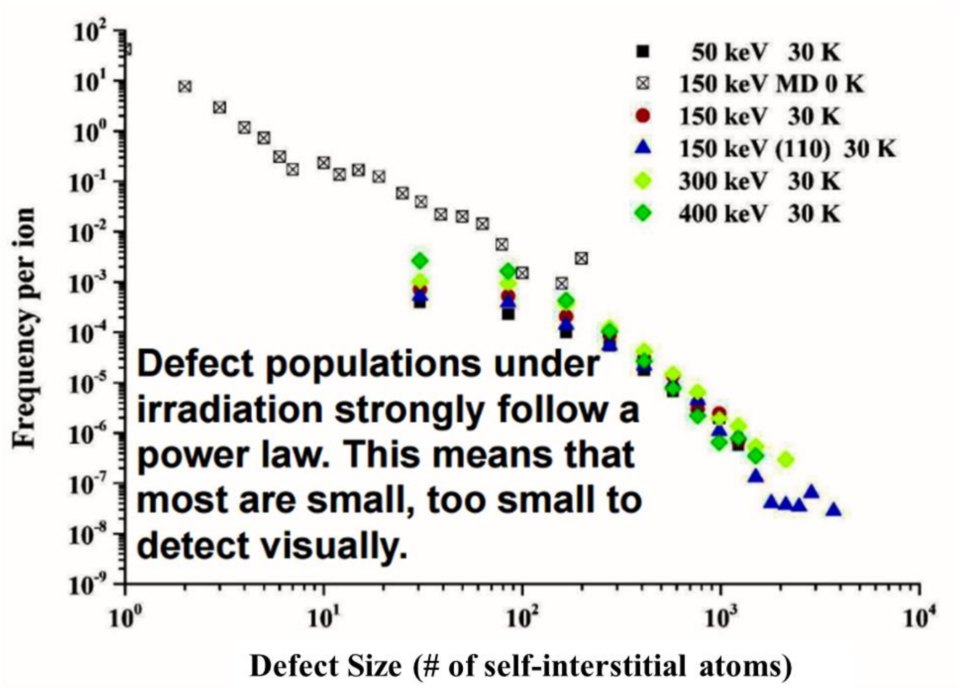

Defect populations under irradiation strongly follow a power law. This means that most are small, too small to detect visually.

Figure 1.2.1: Results of Sand et al. [3] work showing that the vast majority of defects in a material are too small to see visually.

The vast majority of defect populations under irradiation are very small and cannot be detected visually. This is precisely where the methods presented in this work are useful. This optical technique can examine the sum result of these microscopic effects in the material, which enhances the potential applications of this technique.

It is well established that neutron damage causes swelling or compaction and, in transparent materials, can cause a measurable change the refractive index. This was demonstrated with SiO_2 in 1958 by W. Primak [5] with data re-examined by S. Girard for SiO_2 [6]. Figure 1.2.2 demonstrates how strongly the density and refractive index track as a function of fast neutron fluence. This was also demonstrated for proton irradiation in silicate optical glasses using wave front interference methods by Gusarov *et al.* [7].

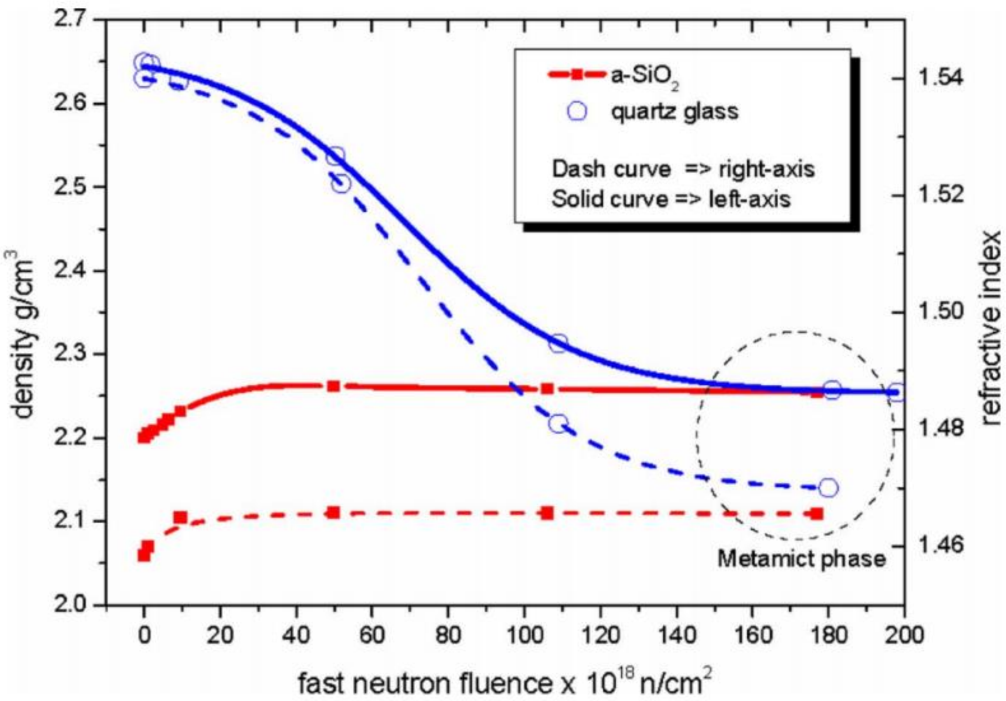

Figure 1.2.2: As higher energy particles enter a material they will naturally produce not just a single PKA, but rather will generate many PKAs that will in turn interact with other atoms within the lattice while the neutrons interact by collision with the nucleus

The purpose of the current research is to demonstrate that that the change of refractive index can be tracked in a crystal with the high precision technique developed by J.-C. Diels at the University of New Mexico [8]. A brief proof of concept for CaF_2 showed that this technique provides very high precision measurements of the change of refractive index [9]. The utilization of this optical technique is of paramount importance to this work and is described in detail in Chapter 3.

The work in this dissertation has been successful in measuring refractive index change following neutron irradiation. To set the stage for future applications, this could serve for active reading of crystals undergoing neutron damage by optically coupling the crystals to the optical analysis setup to be described, such as with optical fiber. In fact, Cheymol *et al.*, 2008, studied the effect of high level gamma and neutron irradiation on silica optical fibers [10]. Through the utilization of the CEA OSIRIS Nuclear Reactor they attained a fast neutron fluence of 1.3×10^{20} n/cm^2 with a dose of 16 GGy. While that work did not address refractive index, they examined the effects of radiation on transmission spectra in fibers, which is the difficulty with using optical fibers in radiation environments. They showed absorption minima in the near infrared (IR) and the IR region utilizing particularly high purity silica and hollow core photonic bandgap fibers. This is the wavelength range in which the optical technique demonstrated here operates, opening the future possibility of using it with fiber optics in a high radiation environment.

It should be noted that there are three primary types of instruments used to measure radiation fields: detectors, which give an active response; monitors, which often produce a vague response such as crossing a threshold; and dosimeters, which are usually integrating in nature and are used for a later read out. This research focuses on utilizing CaF_2 as an integrating dosimeter. By coupling the readout to the crystal while it is in the radiation field, such as with fiber optics, it will be possible for the crystal then to be used as a detector with a live-time readout.

1.3 Problem Description

Neutron irradiation damages materials by producing lattice dislocations, which create voids and in general causes swelling in a material, decreasing the material density. In some materials, there may be compaction and thus an increase of density. In either case the analysis contained herein would still apply. Swelling is correlated with a decrease in the index of refraction, which can be measured with high precision. In June 2015, our group measured the frequency ratio (described in more detail in Chapter 3), used in our technique to extract the refractive index, with a standard deviation of the mean of $3x10^{-8}$ [9]. With a goal as hopeful as enabling high precision neutron dosimetry, and moving towards high-precision real-time neutron dosimetry there are many challenges along the way. Here they will be presented beginning with radiation damage and concluding with crystal based dosimetry. Challenges that have been encountered, or are expected to be encountered, follow.

Modeling, simulation, and experiments were performed to understand radiation damage in CaF_2. For simulations, there is a significant lack of radiation damage molecular dynamics (MD) research on CaF_2. This requires a combination of potential energy files to analyze collisions at small atomic separations. Moving from the MD atomic lattice scale to the meso-scale also presented challenges as many of the meso-scale models do not take into account crystal structure and there is expected to be some error in the modeling.

The measurement of the dose in the crystals by subsequently measuring the refractive index utilizing a nested Fabry-Pérot Etalon (FPE) in linear laser cavity was the most challenging aspect to this research as inevitably, high precision results depend very heavily on high precision instruments and are thus very sensitive to uncertainties. These are detailed later in this work. The characterization and repeatability analysis of this method is essential for moving forward. The estimation of received dose in the crystal samples also presented a challenge. Although with the aid of MCNP, published neutron kerma factors, and accurate modeling of the radiation field, the estimation of dose is at the very least, consistent throughout the research.

The final challenge in the current work was irradiating CaF_2 samples neutrons and observing refractive index changes. This has been done over a range of neutron energy fluences and doses to examine trends in the refractive index.

1.4 Scope of this Dissertation

There were several primary goals of this research, in both calculation and experimentation. The first was to understand the collision physics within crystalline materials on the atomic scale. This was accomplished by determining the Threshold Displacement Energy (TDE) of both calcium (Ca) and fluorine (F) atoms in a CaF_2, face centered cubic (FCC) crystal structure and performing small-scale damage cascade analysis. This utilized LAMMPS Molecular Dynamics (MD) code and is discussed in thorough detail in Chapter 2. The second goal, which is the major goal of this work, was measuring the refractive index change from neutron irradiation of a sample. Doing this required a thorough characterization of the nested-cavity method of determining refractive index change. This is discussed in Chapter 3. Next, the design of the experimental irradiation method and dose calculation standard is presented in Chapter 4. The resulting effects of the neutron irradiation are discussed in Chapter 5 along with the correlation of the crystal damage, dose, and refractive index change. This is followed by the overall conclusions in Chapter 6. A brief discussion of the future steps to expand this research is contained in Chapter 7.

Chapter 2: Neutron Radiation Damage Modeling and Simulation

2.1 Overview

Understanding the propagation of radiation damage in a material is paramount to predicting the material damage effects. It has been assumed that the Displacements per Atom (DPA) value is the most accurate way to determine what will happen to a material in the large scale when considering a small-scale calculation. However, it has been shown more recently that the correlation between DPA and material effects is in many cases secondary or coincidental [1]. In fact, the expectation and demonstration from Dethloff [1] is that small defects, in a region of 5 nm or less, are responsible for the majority of the changes in material properties. Given this fact, it was necessary at the beginning of this work to study the propagation of damage and small scale defects in CaF_2. This can be approached with molecular dynamic (MD) simulations.

The modeling and simulation in this work is comprised of two primary components, both of which are detailed in this chapter. First, the method for determining the baseline properties of damage, namely, the TDE of Calcium and Fluorine atoms in CaF_2 is discussed. Second, the method for utilizing LAMMPS (Large-scale Atomic/Molecular Massively Parallel Simulator) [11] for basic damage cascade simulations, atom recoil energies up to 5 keV, and the extrapolation of that data to higher energies, is presented. All simulations were performed utilizing the Center for Advanced Research Computing (CARC) at the University of New in Albuquerque, NM. A major consideration of the damage cascade analysis is the expectation of what is termed self-annealing. This is a well-understood property of a crystalline material that allows for re-crystallization after a damage cascade occurs [12], and is examined in the short time scales of the MD simulations. Crystalline materials have been shown to hold up to the intense environments of radiation fields better that most materials specifically because of this self-annealing effect.

2.2 Radiation Damage & Recovery Background

2.2.1 Radiation Damage vs. Radiation Effects

The specific terminology used in describing irradiated materials is important to define. "Radiation damage" generally refers to atomic displacement, or the microscopic events that produce the appearance of large-scale changes in a solid [13]. In other words, damage occurs when there are individual interactions inside a material. For incident neutrons, this is primarily through nuclear scattering collisions. This may cause atomic displacements producing lattice vacancies and, where the displaced atom stops, interstitials. The field of radiation damage has benefited greatly from high power computer processing as much of this field relies on computer simulation of lattices to understand the damage cascades that take place on an atomic level when an incident particle collides and directly knocks an atom out of its lattice position. This displaced atom that recoils directly from the incident particle is referred to as a Primary Knock-on Atom (PKA), and there can be many PKAs from a single incident particle, but this distinguishes them from the cascade that often follows. There are several robust programs today that can be used to build lattice structures and simulate damage cascades. The primary program utilized in this research is called LAMMPS and was developed by Sandia National Laboratories.

"Radiation effects" on the other hand generally refers to the “macroscopic, observable, and often technologically crucial results of exposure of solids to energetic particles” [13]. Unlike radiation damage, radiation effects can be studied without the aid of computer simulations, though experimental research in this area is typically supported and substantiated by meso-scale simulations. These meso-scale simulations are beyond the scope of the current, primarily experimental, work.

The ultimate goal of each is to predict the large-scale effects of radiation on a material and specifically determine how its intrinsic properties will be changed as a result of irradiation. In many cases these models are aided by prior molecular dynamics simulation to determine baseline radiation damage properties of the material such as, in particular, the Threshold Displacement Energy of each of the types of atoms in the material.

The primary concern exploring radiation damage is in predicting the configuration and total number of vacancies and interstitial sites within a material based on the characteristics of the material and the bombarding particles. The field of radiation effects is primarily concerned with the bulk effects of radiation damage on large scale material properties, the macroscopic or large scale results of radiation exposure.

As mentioned, the terms "radiation damage" and "radiation effects" are frequently interchanged as if they mean the same thing but it is important in this research to distinguish between them early on. One key distinguishing factor between the two is time scale. Radiation damage takes place within 10s of picoseconds of a particle collision. The subsequent radiation effect processes that change material properties take much longer. That timing ranges widely and can be milliseconds for some diffusion processes, while in metals some processes take months to form noticeable effects [13]. This is important for the consideration of the long-term recovery of a material, which is one of the things that is explored in this research. The bulk of the modeling and simulation of this research is concerned with radiation damage and ultimately how damage propagates in single PKA systems. By focusing on this aspect several key factors can be extracted that can then inform the amount and type of defects that may form in a larger scale irradiation.

2.2.2 Types of Scattering and the PKA

In radiation damage the incident particle collides with an atomic nucleus in a lattice structure, the PKA. The energy transferred to the PKA varies greatly depending on the energy of the incident particle and the angle of the collision.

There are three primary types of neutron interactions: capture, elastic scatter, and inelastic scatter. In capture, when a neutron collides with a nucleus it can be absorbed into the nucleus. Elastic scatter is a dominant neutron interaction for <1 MeV neutrons, especially in low-Z materials [14]. In an elastic collision, all kinetic energy is conserved. A depiction of a classical elastic collision is given in Figure 2.2.1. Finally, at energies above the excitation energy of the target nucleus, usually on the order of 1 MeV for light nuclei, it can scatter inelastically [15].

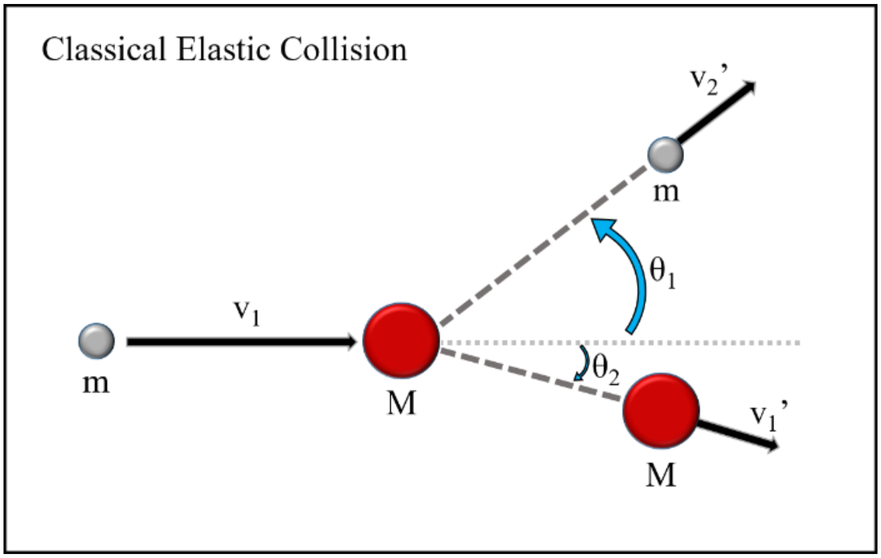

Figure 2.2.1: Depiction of a classical elastic collision between two particles of different mass.

The classical elastic collision is defined in which there is no loss of kinetic energy. As depicted in Figure 2.2.1 the neutron (or other particle) with mass, m, collides with an atom with mass, M, and they scatter in separate directions but the resulting velocities can be determined using equation 1, derived using conservation of kinetic energy [13],

$$\frac{1}{2}m_1v_1^2 = \frac{1}{2}m_1v_1'^2 + \frac{1}{2}m_2v_2'^2 \quad \text{(Eq. 1)}$$

with a maximum energy transfer of ΔE = 4mM/(m+M) and an average ΔE of half of that for neutrons. This will play into the kinematic equations used later and in simulations. With small lattice potential energies holding the atoms in place compared with the kinetic energies, the majority of the interactions used here can be approximated as elastic. For the duration of this work, lattice potential energies are commonly referred to as simply, lattice potentials or potentials. Using the law of conservation of momentum, the angles can be determined using Equations 2 and 3.

$$m_1 v_1 = m_1 v_1' \cos\theta_1 + m_2 v_2' \cos\theta_2 \qquad \text{(Eq. 2)}$$

$$0 = m_1 v_1' \sin\theta_1 - m_2 v_2' \sin\theta_2 \qquad \text{(Eq. 3)}$$

In an inelastic collision, kinetic energy is not conserved and therefore Equation 1 no longer applies however conservation of momentum is still in effect. An inelastic collision occurs when, upon scattering of the neutron, some kinetic energy is lost from the system such as when leaving the nucleus in an excited state which later decays [15].

In capture, the neutron is absorbed in the target nucleus, which may de-excite through subsequent particle or photon emission. In the case of radiative capture, the neutron is absorbed into the nucleus of the target atom and deexcites by emitting a photon. Other capture reactions may result in emitting an electron, gamma ray, alpha particle, etc. For example, within CaF_2, when non-radioactive fluorine (^{19}F) absorbs a neutron it becomes ^{20}F which is unstable, having a half-life of only 11.16 seconds. It decays by ejecting a beta particle causing it to turn into ^{20}Ne which is stable and will not decay further. While capture does in fact happen in the CaF_2 crystals, and inelastic scatter occurs more readily at higher energies, elastic scatter is much more dominant at the neutron energies used and is the only interaction examined in the simulations.

2.2.3 Molecular Dynamics Models for Radiation Damage Analysis

In scattering events, as higher energy neutrons enter a material they will produce not just a single PKA, but rather will generate many knock-on atoms, referred to as, secondary knock-ons, that will in turn interact with other atoms within the lattice. While the neutrons interact by collision with the nucleus of the PKA, the recoiling atom is a charged particle and may interact through the Coulomb interaction, causing both atom recoils and ionization. Spaces left where atoms used to be in their lattice positions are called dislocations, and atoms that are then not between lattice locations are called interstitials. This multiple atom dislocation event is generally referred to as a damage cascade. The ability to understand how a damage cascade forms, propagates, and persists in a material is of paramount importance in understanding what the effect will be on the material. Radiation damage calculations are usually performed using modeling software that simulates a given materials structure and tracks a PKA, its collisions, and the subsequent lattice collisions produced by the numerous displaced atoms, which will collide with many other atoms. This type of simulation assumes elastic collisions with the nuclei, a reasonable approximation at these energies. It also takes into account the other potential forces acting upon an atom in the lattice and thermal vibrations, which, in turn, allows for simulation of a crystalline material's ability to self-anneal. Self-annealing is a crystals ability to return to its original lattice structure after it has been deformed. This is of course not a complete return, especially in the case of radiation damage, which will cause atoms to be displaced significantly in a lattice; even to a point where returning to their original lattice site requires more energy than remaining where they are. In this way, semi-permanent defects are created.

Atomic scale modeling of this structure and simulation of this type of damage, can be performed by a wide range of software. The general categorical name for these types of simulations is Molecular Dynamics (MD). The key to successful MD is accurately being able to state the potential energy and forces acting upon each atom in a given structure. Thus, MD generally deals with small spatial and time scale simulations due to the computational overhead. Considering the energies required for damage cascades to form, large simulations are required, and thus large computing resources are also required. For example, in a calcium fluoride (CaF_2) crystal lattice, one must define the potential and force acting between each atom pair based on distance. Thus, one must define Ca-Ca interactions, Ca-F interactions, and F-F interactions for a range of separation distances, and must model a series of these lattice locations which, expanded in three dimensions, requires extensive computation.

Defining proper lattice potential energies is not simple. While potential energy files and potential energy coefficients for MD are abundant [16] there are several things in this research that make the overall selection process more difficult. Due to the potential being a key component of any MD simulation, the process used to determine which potentials to use and how to use them is critical [17]. This work focuses on crystal structures in general, and specifically on CaF_2. While CaF_2 is a common compound, and thus many of its characteristics and properties have been studied thoroughly [18] [19], literature does not show that it has been looked at extensively for high energy radiation damage simulations. There are a large variety of pair-wise potential energy equations meant to define the potential energy between two atoms in lattice. Each of these styles of expressing potential energy are intended for different types of MD simulation. The most relevant potential energy styles for this research were the Buckingham, Born-Mayer-Huggins (BMH), Coulombic, and Ziegler-Biersack-Littmark (ZBL) potential. These potential energies and others are outlined well considering the radiation damage simulation requirements by B. Cohen in "On force fields for molecular dynamics simulations of crystalline silica" in 2015 [20]. The generation of the potential energies for this research are discussed in greater detail in Section 2.3.1.

2.2.4 The Threshold Displacement Energy (TDE)

The threshold displacement energy, TDE, is the energy, typically measured in eV, that must be transferred to an atom in order to displace it from its lattice site. In crystals, a different TDE exists for each crystallographic direction. The displacement threshold has been defined for a variety of materials, particularly metals and some semiconductors. For most materials, the TDE is stated to be between 10-50 eV [21]. The vast majority of research in this area has been accomplished utilizing either classical [22] [23] [24] or quantum mechanical [25] [26] molecular dynamics computer simulations. These simulations give very good approximations of TDE, especially in the case of covalent materials and low refractive index crystals [25]. In general the TDE can be used to estimate higher-energy damage production such as estimating the total number of defects produced. This can be done using the Kinchin-Pease or NRT equations [27] [28]. Another way to utilize this value is for input into computer codes like SRIM to estimate overall damage. However, extreme caution must be used when dealing with nuclear energy depositing more that $2E_{d,ave}/0.8$ at which point there will be error due to thermally activated recombination and other recombination effects [21].

The TDE of a material can be determined through simulation. There are two ways of accomplishing this task in LAMMPS. LAMMPS (Large-scale Atomic/Molecular Massively Parallel Simulator), a code developed by Sandia National Laboratories, is the primary code utilized in this research. For the first, a periodic increase of PKA energy is performed and at each energy a large number of random three dimensional angles are selected one at a time in order to statistically determine the probability that displacement will occur at that energy. This method will produce the average TDE given a large variety of incident angles. This method is exhibited well by B. Cowen [29] for SiO_2. Another way of obtaining this value when the incident angle is of interest is performing a large number of simulations for each energy at a number of specified angles. The former is the method utilized in this research and the average TDE is determined using the data produced.

2.2.5 The Damage Cascade

Beyond TDE, Monte Carlo codes can be used to simulate radiation damage cascades [30] [31]. There are a variety of codes available though some are specifically tailored to simulate damage cascades. Though LAMMPS is not specifically designed to be used for radiation damage it is a long-standing well-developed and flexible tool that can be used for damage cascade research. Before diving into the simulations, however, it is important to understand the basics of the theory behind displacements cascades brought on PKAs. The most simple theoretical basis for damage cascades is attributed to Kinchin and Pease [32]. There are six primary assumptions in their model:

1. The cascade is defined as a sequence of collisions based on two-body elastic theory.
2. The spread displacement probability is ignored, so if the Energy > TDE then the displacement probability is set to 1.
3. The TDE is neglected in calculating kinetic energy transferred to target atom.
4. PKAs with energy greater than a cutoff energy are ignored until their energy is decreased to less than the cutoff by electronic stopping forces.
5. Energy transfer cross-sections are derived through the “hard sphere” model
6. Crystal structure is ignored, so there is no opportunity for self-annealing and no difference in behavior due to direction of travel.

Making these assumptions allows for basic calculation of displacement cascades. Naturally in progressing through cascade theory some of these assumptions must be reconsidered to increase accuracy in calculations. In some cases, the assumptions must be relaxed and in some cases they are ignored altogether, such as in the calculation of a displacement spike [13]. Calculations of basic energy transfer can be completed using Equations 1 – 3 while adhering to these assumptions. Early theory of cascade development follows these equations, assuming a very dense region of interactions, and is represented visually following a PKA in Figure 2.2.2.

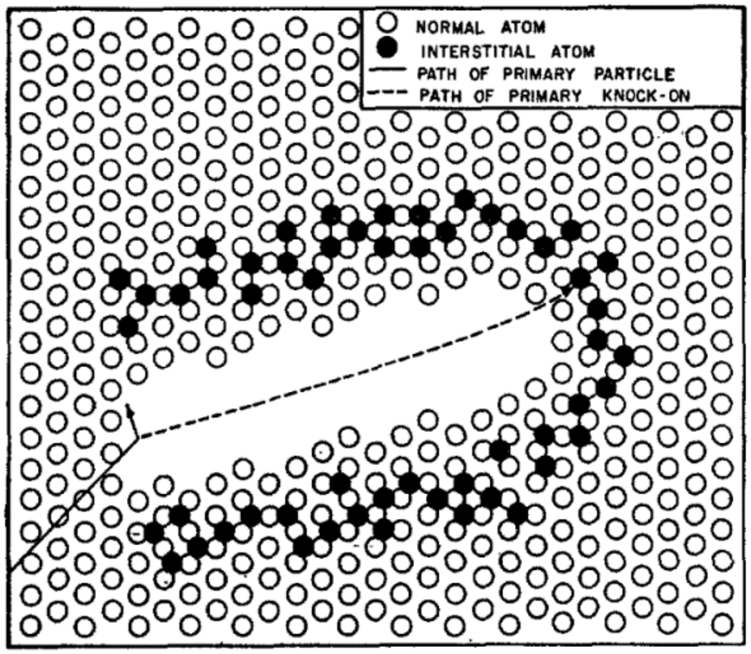

Figure 2.2.2: Early theory depiction or radiation induced PKA displacement cascade [33].

Applying these events to crystalline structures becomes much more complicated, as atoms may not dislocate neighboring atoms with as high a probability as thought, and as crystalline structures have very strong directionally dependent bonds that tend to exhibit the process of self-annealing as discussed earlier. Thus, it was discovered that this early understanding of radiation induced PKA displacement cascades was incomplete. Atoms, including the PKA, may travel some distance before displacing another atom. This is due to the low probability of an atom striking, or transferring enough energy to displace that other atom. The more probable paths of a PKA and secondary atoms is described well by Seeger [34] and later by Olander [13] who also performed computer simulation of displacement spikes showing the very randomized path PKAs and secondary knock-ons take in a crystalline structure. Seeger’s updated theory on PKA caused displacement is shown in Figure 2.2.3, while Olander’s simulation is shown in Figure 2.2.4.

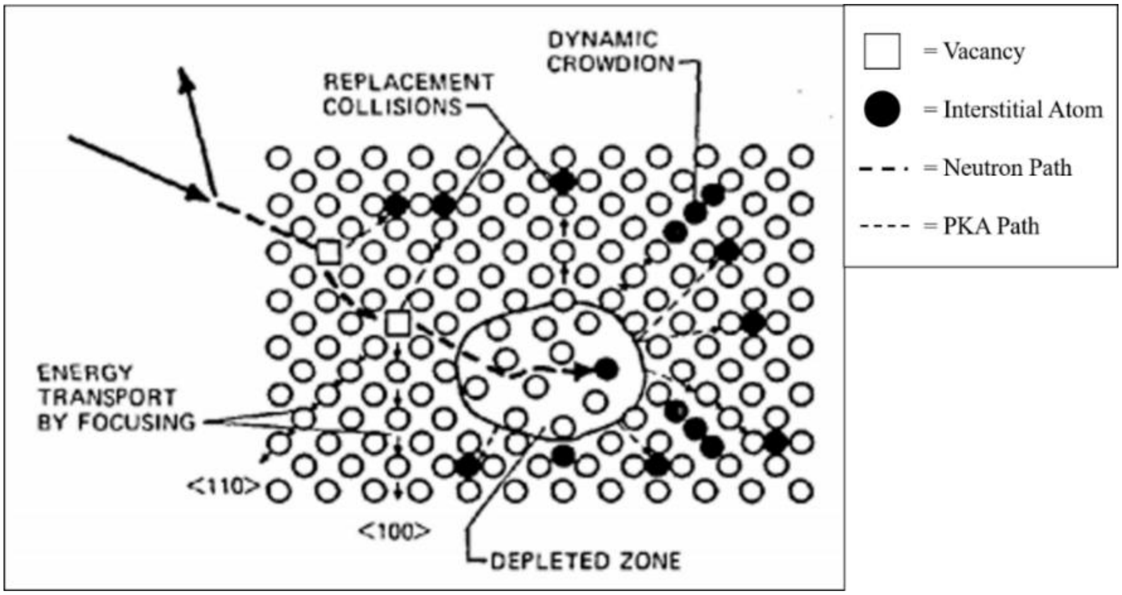

Figure 2.2.3: Later quantitative version of radiation induced PKA displacement spike presented by Seeger [34].

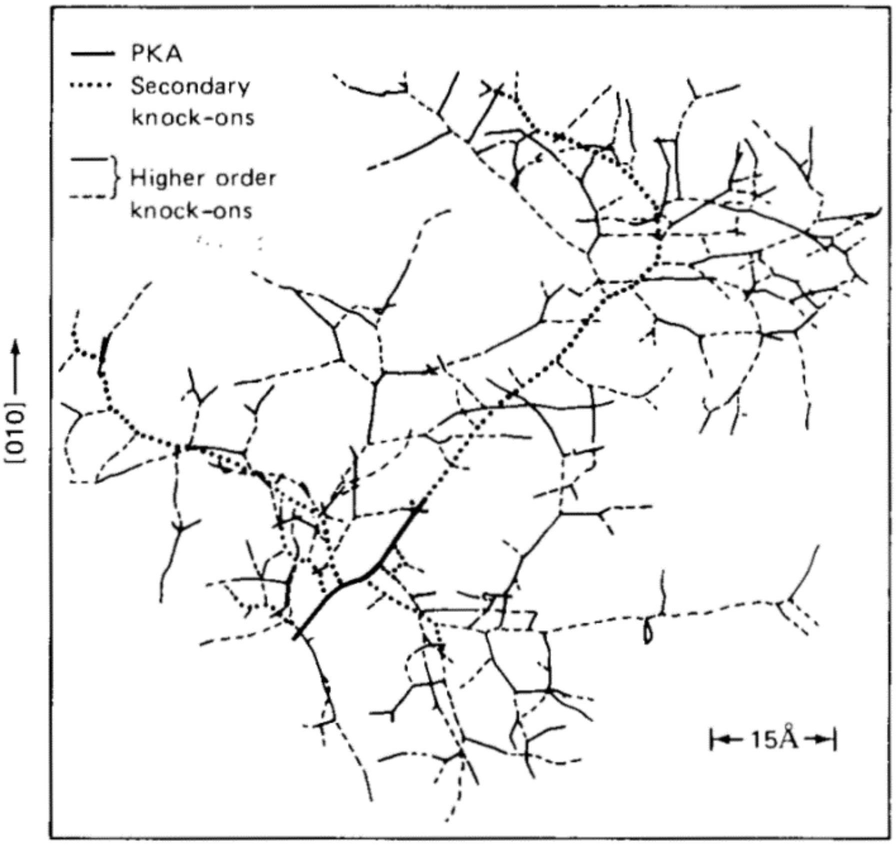

Figure 2.2.4: Radiation induced displacement cascade as simulated by Orlander displaying the PKA path, secondary knock-on path, and higher order knock-ons [13].

Figure 2.2.3 and Figure 2.2.4 suggest the vast complexity of tracking damage cascades in a material due to the fact that a PKA may travel a large distance before displacing another atom, several PKAs may be produced at different locations from the incident neutron, and secondary atoms may also displace yet further atoms. Although, the work here is at lower energies, the fact that Coulomb effects are negligible for charged particles traveling at high energies (in fact, displacement efficiency is higher for lower energies) compounds the complexity. This is where MD codes, like LAMMPS, provide great help in analyzing these problems. When specified properly the potential files used to simulate the crystal structure with LAMMPS grant a view of the damage as it occurs showing what is likely to be taking place on the atomic scale. MD codes typically operate on very short time scales, allowing for analysis of the short-term effects of damage cascades. However, due to this time scale, MD codes are not ideal for analyzing long term effects of damage cascades. Provided the simulation size is large enough to contain the entire cascade, which is a function of the PKA energy, the effects on the crystal structure can be analyzed closely. Figure 2.2.5 demonstrates these phenomena well.

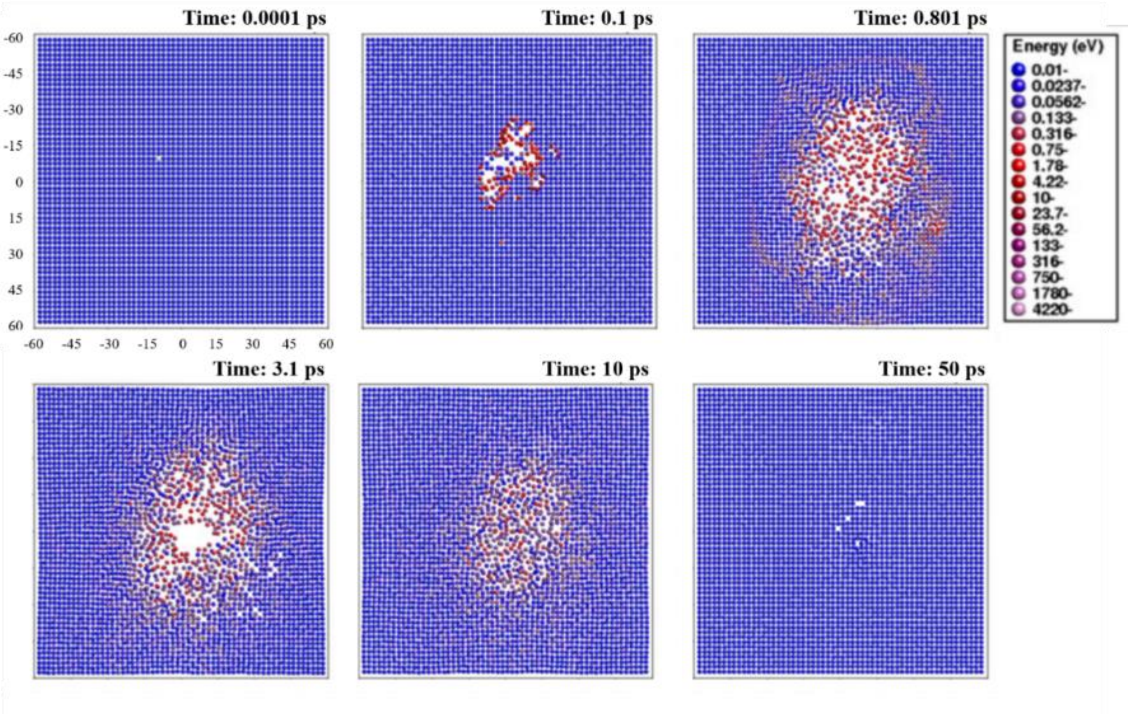

Figure 2.2.5: Depiction of a sample damage cascade caused by a 10 keV gold (Au) atom within a gold Face-Centered Cubic (FCC) lattice, similar to CaF_2 [35].

Figure 2.2.5 demonstrates the effect of a PKA within a lattice at various time periods after the PKA begins its cascade. At 0.0001 ps it shows only one displacement which is the PKA. However, by 0.1 ps through a number of collisions the energy brought in by the PKA begins to affect the local structure of the material. This effect is intensified and maximized at 0.801 ps before beginning the initial stages of self-annealing. At 3.1 ps self-annealing is beginning to become evident and continues through the 10 ps image. What is seen at 50 ps is the semi-permanent damage within the crystal after the self-annealing process is completed. This is the point at which the material will remain unless a specific amount of energy is applied giving the displaced atoms enough energy to return to their original lattice sites. One way that this could be accomplished is through thermal annealing, by placing the sample in a furnace and heating it to a specific temperature for a period of time. This, however, is not part of this current research but is certainly of interest if the CaF_2 samples used are required to be reused after irradiation.

2.3 LAMMPS Modeling Set Up

2.3.1 Atomic Potential File Exploration

The first and most important step in developing a model in LAMMPS is the exploration and definition of a potential energy, simply called potential here following the standard in manuals. The potential in a LAMMPS simulation defines the potential energy between pairs of atoms in a structure, in this case a CaF_2 crystal lattice. The most important aspect in utilizing the LAMMPS package is the determination of which potential files to use. The potential files define the interactions between all atoms in the material. These potentials, when combined with Coulombic interactions built into LAMMPS, define and keep the crystal structure that is built at the onset. When defined well, after equilibration the atomic lattice constant and the density of the material will mirror the physically tested properties. In this research one complication is due to the use of a compound, specifically that of CaF_2, therefore three categories of potentials must be defined. These three categories are the interactions of the calcium with calcium (Ca-Ca interactions), calcium with fluorine (Ca-F interactions), and fluorine with fluorine (F-F interactions). Each of these categories has a potential defined for a specific set of atomic separations (the distance between the two atoms). There are a large variety of ways in which to define a potential. For this work, several potentials were considered. It is clear, after searching through literature, that CaF_2 is a well explored material. There are several good representations of CaF_2 material potentials each of which were explored as a possible adaptation for this research. These potentials have been defined and used to simulate various activities within CaF_2 and those works provide a good baseline for analysis of the potentials in this effort. These previously defined potentials considered for this work were (1) Born-Mayer-Huggins (BMH) [36] [37], (2) Buckingham [38], and (3) a modified Buckingham [39], referred to as different "styles" of potential.

A BMH potential style defines the potential energy between atoms with Equation 4.

$$E = Aexp\left(\frac{\sigma - r}{\rho}\right) - \frac{C}{r^6} + \frac{D}{r^8} \qquad \text{(Eq. 4)}$$

A Buckingham potential style defines the potential energy between atoms with Equation 5.

$$E = Ae^{-r/\rho} - \frac{C}{r^6} \qquad \text{(Eq. 5)}$$

A Modified Buckingham potential style defines the potential energy between atoms in a similar way as the Buckingham but adds an additional term shown with Equation 6

$$E = Ae^{-r/\rho} - \frac{C}{r^6} + \frac{D}{r^{12}} \qquad \text{(Eq. 6)}$$

In these equations r is the variable that defines the distance in Angstroms (Å) between two atoms while, ρ, A, C, and D, are coefficient parameters defined specifically for each potential style. Lastly, in equation 4, σ is the diameter (the value of r, at which E=0). These coefficients were taken from previous works and are outlined in Table 2.3.1.

Table 2.3.1: Published pair wise potential style parameters for BMH, Buckingham, and Modified Buckingham styles for interactions within CaF_2.

	Ion Pair	ρ(Å)	A (eV)	C (eV)	D (eV)
Born-Mayer-Huggins	Ca^{2+} - Ca^{2+}	1	0	0	0
	Ca^{2+} - F^-	0.3360	674.3	0	0
	F^- - F^-	0.2930	1808	109.100	0
Buckingham	Ca^{2+} - Ca^{2+}	1	0	0	0
	Ca^{2+} - F^-	0.2997	1272.8	0	0
	F^- - F^-	0.1201	$9.97\text{x}10^{-7}$	17.024	0
Modified Buckingham	Ca^{2+} - Ca^{2+}	0.1690	44898.1	0	0
	Ca^{2+} - F^-	0.2997	1273.8	0	0
	F^- - F^-	0.2753	1127.7	15.830	15.830

When considering small atomic separations of atoms there are errors associated with the BMH and the Buckingham potential styles. The modified Buckingham takes these errors into account but is not defined within the LAMMPS code as a valid potential style and therefore to use it the LAMMPS code would require extensive editing. Thus, the initial experiment was looking at the equilibration of the BMH potential compared to the Buckingham. Both performed well for equilibration but the Buckingham provided a density value closer to the published data for CaF_2. The next aspect to consider was the error in both the BMH and the Buckingham when considering the small atomic separations. Unfortunately, because of this error, one potential style is not able to define the entire region necessary for this work. The approach that was necessary due to the unique requirements of high energy particles (which in terms of molecular dynamics is as low as 1 keV) is, a combination of multiple potential styles. Without this combination, some interactions incorrectly plummet to extremely large attractive potentials at small atomic separations. If not corrected for this will cause the simulation to fault when atoms become close enough to each other because, instead of being repulsed by one another, they will be attracted. Furthermore, in the simulation, as the attraction increases and they get closer to one another they may fuse together, which is clearly not physical. What most of these potentials do not take into account is the extremely repulsive Coulomb force nuclei have at very small atomic separations. This behavior, ultimately, is not difficult to correct for. The solution is utilizing different potential styles at different distances [29]. One style is used to define the potentials at small separations and one to define the potential at larger separations. A subsequent spline of the potentials is necessary to define the final potential.

In literature the Lennard-Jones standard utilizes a ZBL potential for small atomic separations [30]. However, due to the restrictions of this work however a different option had to be considered.

Therefore, both the BMH and Buckingham potentials were splined together with a standard ZBL potential for small atomic separations using a python code called “atsim.potentials” created by M.J.D. Rushton [40]. Contrary to the previous comparison between the BMH and Buckingham, the BMH when splined with the ZBL was a near perfect match resulting in a density within 1% of the scientifically reported standard for CaF_2. The Buckingham/ZBL spline however did not combine well and caused a decrease in stability of the simulation cell. Given this fact and the long-term stability of the BMH/ZBL spline, the BMH/ZBL potential was used in conjunction with LAMMPS injected Coulombic interactions for all of the LAMMPS work done in this research.

The BMH and ZBL potentials are shown with the spline created between them in Figure 2.3.1, thus enabling radiation damage simulations at small atomic separations.

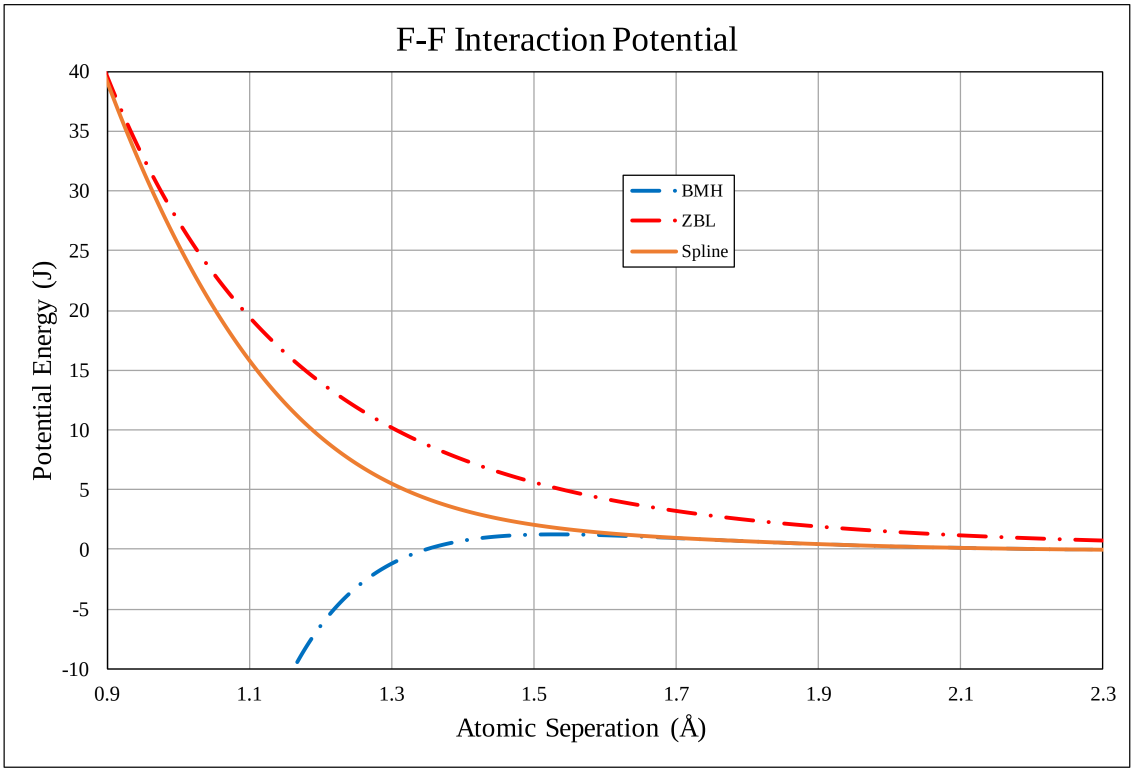

Figure 2.3.1: Plot of the fluorine-fluorine interaction potentials demonstrating the error in the BMH potential for small atomic separations (the exponentially attractive force in the negative direction), the error in the ZBL potential at large atomic separations (the excess repulsive force), and the spline potential generated by atsim.potentials to create a more correct overall potential.

Figure 2.3.1 shows the error in the BMH at small atomic separations is shown in the dashed blue line which begins to plummet towards an attractive (negative) force at about 1.5 Å. The ZBL, while more accurate in this region is less accurate for separations greater than 1.5 Å. Thus, by splining the two a resultant potential combines the accurate region of both potentials into a single potential. Figure 2.3.2 shows the spline characteristics for the Ca-F interactions. It should be noted that for this pair of potentials there is not large attractive force seen for the BMH potential at small atomic separations. There is however a maximum repulsive force that serves as the limit as the BMH potential approaches the atomic separation of 0 Å. Due to this fact, it is still necessary to perform a spline between the ZBL potential for small atomic separations and the BMH at larger separations.

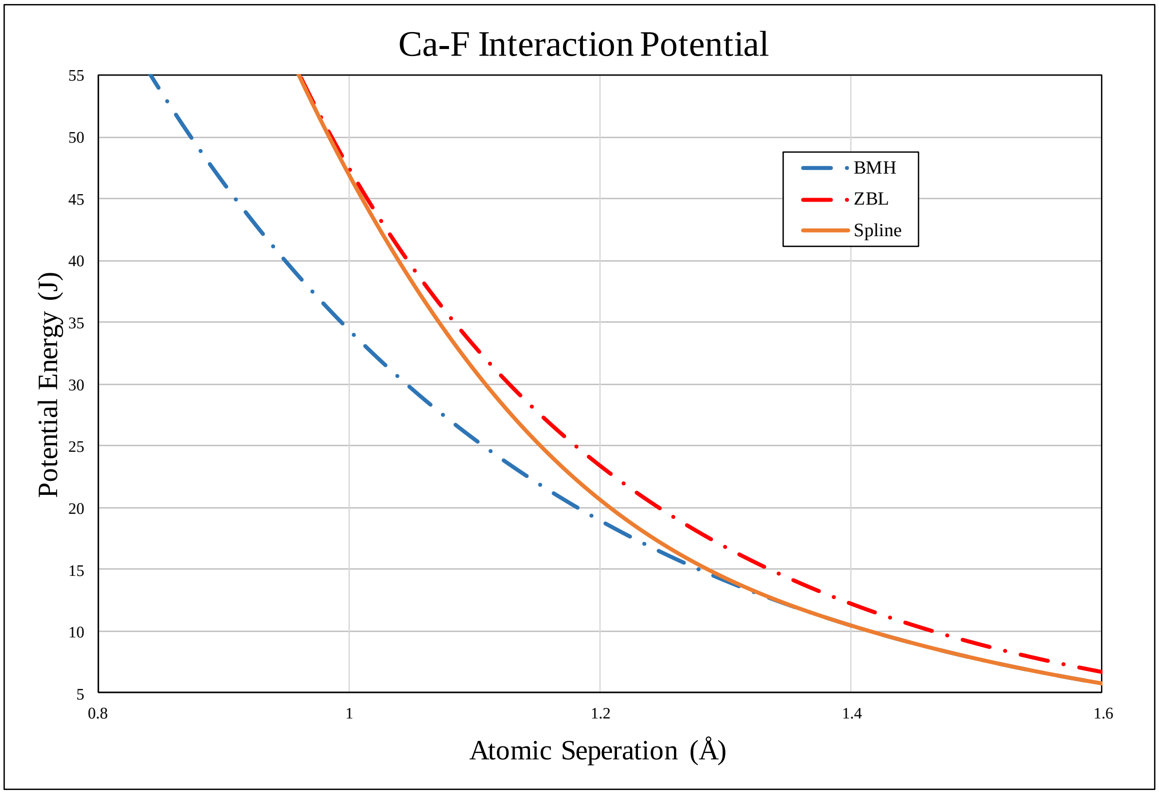

Figure 2.3.2: Plot of the calcium-fluorine interaction potentials demonstrating the error in the BMH potential for small atomic separations (not as repulsive as it should be at smaller separations), the error in the ZBL potential at large atomic separations (not as attractive as it should be at larger separations), and the spline potential generated by atsim.potentials to create a more correct overall potential.

The Ca-Ca interactions were a bit different. The BMH potential (as shown in Table 2.3.1) assumes there is no interaction between Ca atoms [36] due to the relatively large atomic separations of the Ca atoms with other Ca atoms in the lattice. But this doesn't mean there is no interaction at all. In fact, there is still a potential that dominates at small atomic separations that can be modeled by the ZBL potential, and a Coulombic potential that dominates at larger separations. Because of this fact the initial input potential was simply the ZBL potential style and the simulation added in the Coulombic interactions as part of the larger simulation.

2.3.2 LAMMPS input file setup

To move forward, several aspects of the simulation must be defined. These aspects of the code are broken into sections, the initialization, atom definition, force field definition, grouping, initialization, and equilibration. Within the initialization section of the code the units, dimension, boundaries and atom style of the simulation are defined. For this research the set of units used are called "metal" in LAMMPS. The units that are used when setting the simulation units to "metal" are as follows:

- Mass = grams/mole
- Distance = angstroms (Å)
- Time = picoseconds
- Energy = eV
- Velocity = angstroms/picosecond
- Force = eV/Angstrom
- Torque = eV
- Temperature = kelvin (K)
- Pressure = bars
- Charge = multiple of electron charge (1.0 is a proton)
- Electric Field = volts/angstrom

- Density = gram/cc (simulation dimension)

Three dimensions are used with periodic boundaries in each dimension and the "atom style" selected in LAMMPS was "charge", denoting that the atom charges will need to be considered through Coulombic interactions. The atom definition follows with the specification of the lattice constant (5.444 Å for CaF_2) and the placing of one lattice cell of atoms which is then replicated, with each cell containing 8 full F atoms, 4, ½'s of Ca, and 8, ¼'s of Ca. For the damage cascade simulation, each unit cell is replicated 60 times in each dimension, resulting in a 60x60x60 lattice simulation. The TDE simulation does not require as many atoms and therefore was kept to 6 unit cell replications in each dimension. Given that there are twelve atoms per lattice cell in CaF_2 thus the damage cascade simulation contained 2,592,000 atoms while the TDE simulation contained 2,592 atoms. The LAMMPS atom definition section also contains the definition of mass and charge of each atom type. The force field section is next where the potential files are specified. Additionally, a hybrid potential file was created using the Coulombic interactions along with the spline that was created earlier. This accounts not only for atomic interactions but also charged interactions between each atom type. The next LAMMPS section follows with the definition of regions and groups. The definition of regions and groups allows for greater tailoring in tracking displacements. By defining a group of atoms one can extract the collision information for only that group and thus save significant amounts of hard drive space, because each time a dump is created information for nearly 2.6 million atoms is recorded. In the initialization section, all compute commands are defined. These commands define to computational aspects to be run during the simulation. Additionally, the initial crystal velocity, time step, and output styles are set. The equilibration phase is completed using NPT fix command in LAMMPS to set the appropriate temperature and pressure in the simulation cell, and then the simulation is run for a defined number of time steps. Example input files for both the TDE and damage cascade simulations are included in Appendix A.

2.3.3 LAMMPS equilibration verification

As a general check for how the simulation is behaving after the equilibration is completed, it is crucial to compare the density of the material and lattice constant with the defined experimental values. The standard values for CaF_2 are 3.18 g/cc for density, and 5.444 Å for the lattice constant. The equilibrated result from the cascade simulation described here resulted in a density of 3.056 g/cc and Lattice Constant of 5.535 Å. These values are within 10% of the standard values which is in general acceptable. However, these parameters were further refined for the Threshold Displacement Energy (TDE) calculations given that the simulation size could be much smaller for that purpose than for a cascade simulation where some characteristics had to be relaxed for the simulation to be completed in a reasonable amount of time. For the TDE simulations the density and lattice constant were brought within 1% of the standard values resulting in a density simulated at 3.163 g/cc and a lattice constant of 5.473 Å.

2.4 LAMMPS Determination of TDE

2.4.1 Methodology for Determining TDE

The determination of the probabilistic TDE closely followed the theory, and used a similar method, laid out by B. Cohen [29]. The determination of TDE involved a periodic increasing of energy of a PKA for both Ca and F PKAs. At each PKA energy the simulation ran for 5 picoseconds passed within the simulation, utilizing a NPT fix with a randomized seed allowing the lattice to relax between each simulation and to ensure randomized atomic interactions. Similar to the work completed by B. Cohen [29], this simulation was designed to follow the Monte Carlo method in which the direction of the PKA was randomized for a series of PKA energy values to obtain the results. Each simulation was repeated a minimum of 1000 times in order to obtain a statistical value for the probability of displacement for a particular PKA energy within the CaF_2 lattice.

2.4.2 Calcium and Fluorine TDE Results

The results generated were compiled using Matlab within which an atom was considered displaced if its total displacement was greater than 0.8 Å. From there a simple determination of probability of displacement is generated and plotted. The data for the displacement of a Ca atom in CaF_2 is demonstrated in Figure 2.4.1. Similarly, the probability of displacement was determined for F atoms in CaF_2. The results of these simulations are demonstrated in Figure 2.4.2.

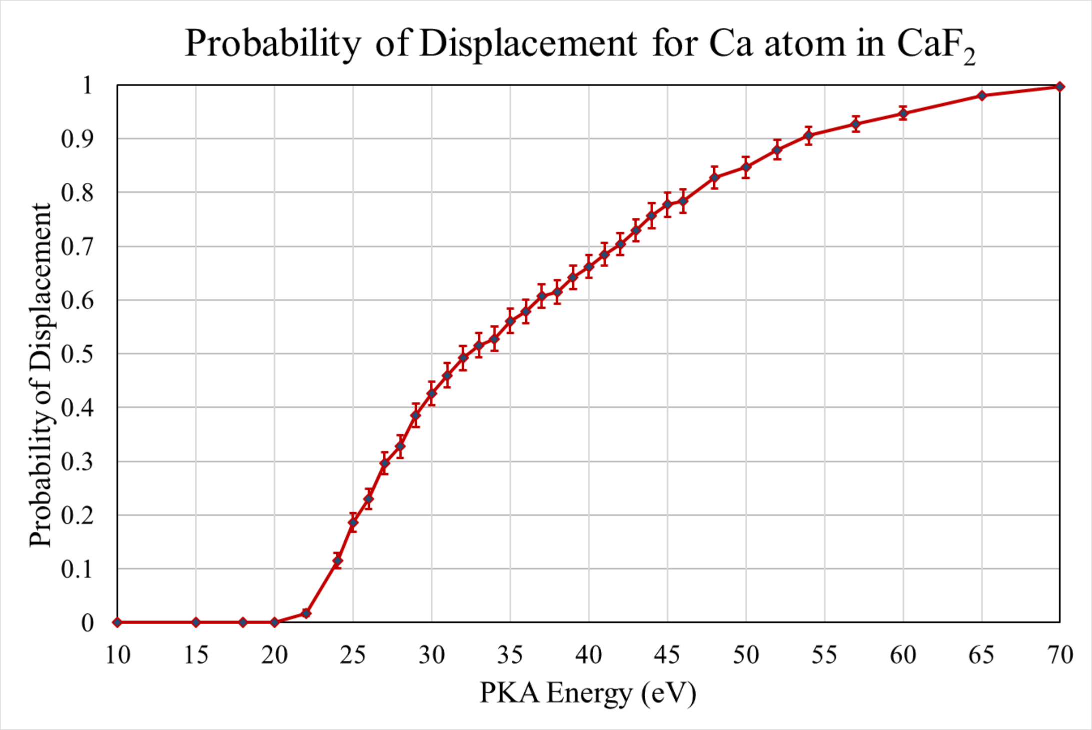

Figure 2.4.1: Statistical determination of probability of displacement for a Ca atom within a CaF_2 crystal lattice.

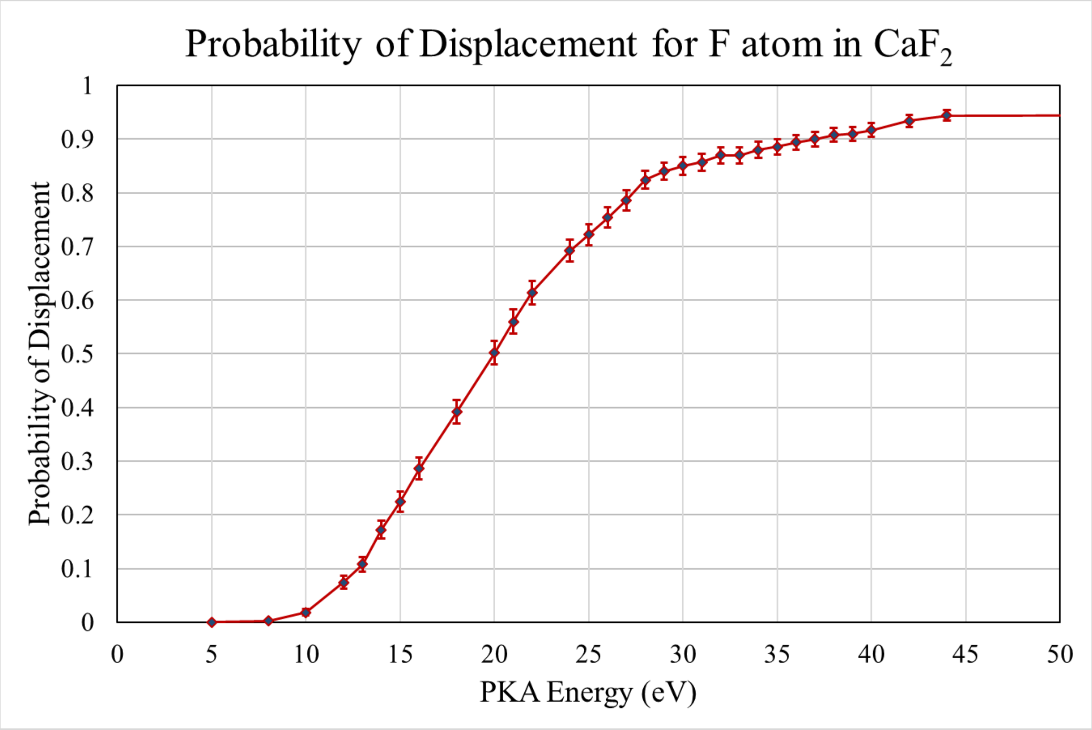

Figure 2.4.2: Statistical determination of probability of displacement for a Ca atom within a CaF_2 crystal lattice.

2.4.3 TDE Conclusions

To date, no current literature had shown the TDE of Ca and F atoms in CaF_2 through molecular dynamics and simulated statistical analysis. As such, the determination of these values is a critical and key accomplishment of this work. Defining the TDE value as the energy at which 50% of the atoms are displaced, as can be seen in Figures 2.4.2 and 2.4.3, the statistical determination for the TDE of Ca, in a CaF_2 lattice, yields a result of 32 eV. Examining F in a CaF_2 lattice yields a TDE of 20 eV. The result of this effort will ultimately aid in further meso-scale simulation of radiation effects and will also serve to set up a follow-on research study into a more detailed and complicated way of approaching the meso-scale damage effects.

2.5 LAMMPS Damage Cascade

2.5.1 LAMMPS Damage Cascade Methodology

After the successful equilibration of the 60x60x60 simulation cell, the damage simulation was set up. To do this the system is changed from NPT (constant Number of particles, Pressure, and Temperature) to NVE (constant Number of particles, Volume, and Energy, thus creating a system consistent with the microcanonical ensemble), but only for the core of the overall lattice, with an exterior “buffer” layer retaining the NPT. Throughout these simulations the damage cascade was watched by tracking the number of vacancies and interstitial sites in the lattice over a period of time (generally about 20 picoseconds). Cascades were produced for a variety of PKA energies for both Ca and F PKAs. To provide the most accurate results, a timestep function was inserted to analyze the velocity of atoms in the material and the timestep was adjusted to ensure atoms were not moving too fast. By doing this the integrity of the potential file is ensured. While the original intention was to do this for a variety of angular momenta this was simply not feasible given simulation times.

2.5.2 PKA Energy Calculation

The first step in modeling radiation damage using LAMMPS was to determine the energy transferred to a PKA from a colliding neutron. Because of the nature of these collisions, relativistic effects do not have to be considered but rather classical mechanics can be utilized to calculate the velocity of a PKA atom. As previously discussed, many of the collisions at these energies are inelastic, meaning that some kinetic energy is lost. However, following the assumptions laid out in Section 2.2.5, a conservative approximation can be made using classical mechanics assuming an elastic collision. This assumption will of course mean that the kinetic energy calculated is likely slightly larger than what will be experienced in nature, but this will provide a good estimate for the energy transferred. Equation 7 shows the calculation of kinetic energy from the mass and velocity of a particle,

$$KE = \frac{1}{2}mv^2 \qquad \text{(Eq. 7)}$$

where KE is the kinetic energy, m is the particle mass, and v is the velocity of said particle. Rearranging the equation allows for calculation of velocity based on a given energy, shown in Equation 8.

$$v = \sqrt{\frac{2KE}{m}} \qquad \text{(Eq. 8)}$$

In the case of a high energy (multiple MeV range) neutron it is likely kinetic that the energy transferred to a PKA will be much greater than LAMMPS is able to simulate in this work due to restrictions on simulation size. The PKAs and subsequent recoils may leave the region contained in the calculation. Given this fact, the work presented here focuses on a variety of PKA energies up to the maximum LAMMPS can handle with the current simulation size, which are about 5000 eV for both Ca and F PKAs. For this setup, the PKA velocity is converted to angstroms/picosecond. A table of PKA energies used for the LAMMPS damage simulation are provided in Table 2.5.1.

Table 2.5.1: A table showing the velocity of a PKA in Angstroms/Picosecond based on the desired PKA energy.

Desired E (eV)	Desired E (J)	Ca PKA Velocity (A/ps)	F PKA Velocity (A/ps)
5000	8.01×10^{-16}	1551.59	2253.60
2500	4.01×10^{-16}	1097.14	1593.54
1000	1.60×10^{-16}	693.89	1007.84
750	1.20×10^{-16}	600.93	872.82
250	4.01×10^{-17}	346.95	503.92
100	1.60×10^{-17}	219.43	318.71
75	1.20×10^{-17}	190.03	276.01
50	8.00×10^{-18}	155.16	225.36
40	6.41×10^{-18}	138.78	201.57

2.5.3 Calcium PKA Cascade Results

The energies in Table 2.5.1 were applied to Ca PKAs in a 2.5 million atom simulation to generate radiation damage statistics. One primary statistic tracked over time was the total number of lattice vacancies/interstitial sites in the simulation cell over a period 11 ps. In the time of the simulation, and consistent with radiation damage timeframes [41]

[42] [43] [44] [45], collisions due to high energy radiation have a very fast self-annealing time, typically on the order of a few picoseconds. This is shown in Figure 2.5.1 where the total lattice vacancies are plotted over time in picoseconds. It is seen here that the initial self-annealing for these energies occurs very quickly and stabilizes into semi-permanent damage after about 3-5 picoseconds depending on the PKA energy. It is a natural assumption based on this plot that the initial self-annealing timeframe would increase at higher energies. It is worth noting, as well, that the initial self-annealing for all simulations was a nearly 90% recovery of the total initial number of vacancies.

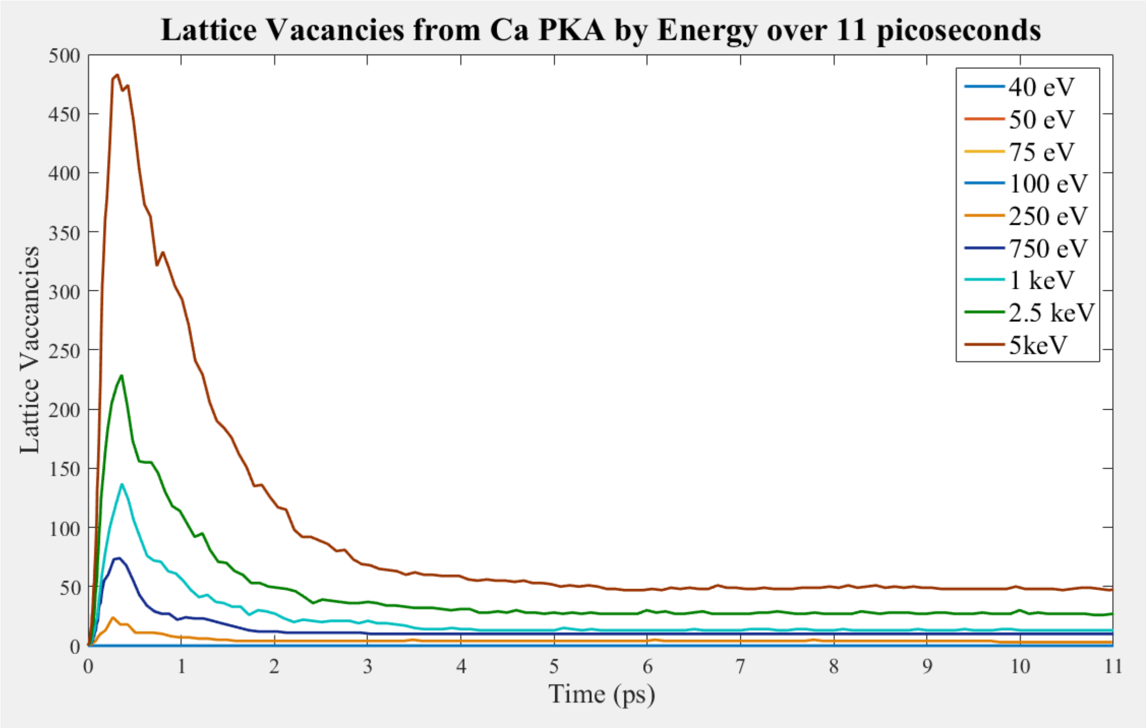

Figure 2.5.1: Plot of lattice vacancies by Ca PKA with varying energies from 0 to 11 picoseconds.

In order to make this information more useful, a plot of persistent or semi-permanent damage was created utilizing the number of vacancies that persisted in the material 11 ps after the initial collision. Figure 2.5.2 demonstrates this subset of data. It is clear, at least for the energies in this range of simulation, that the number of vacancies produced by a single PKA at a specific energy increases linearly with the energy transferred to the PKA. Naturally, there would be a limit to this, however that limit is not present in this data set. Using this data an extrapolation can be made for higher energies based on the equation given in Figure 2.5.2. This equation was determined through a curve fit of the data.

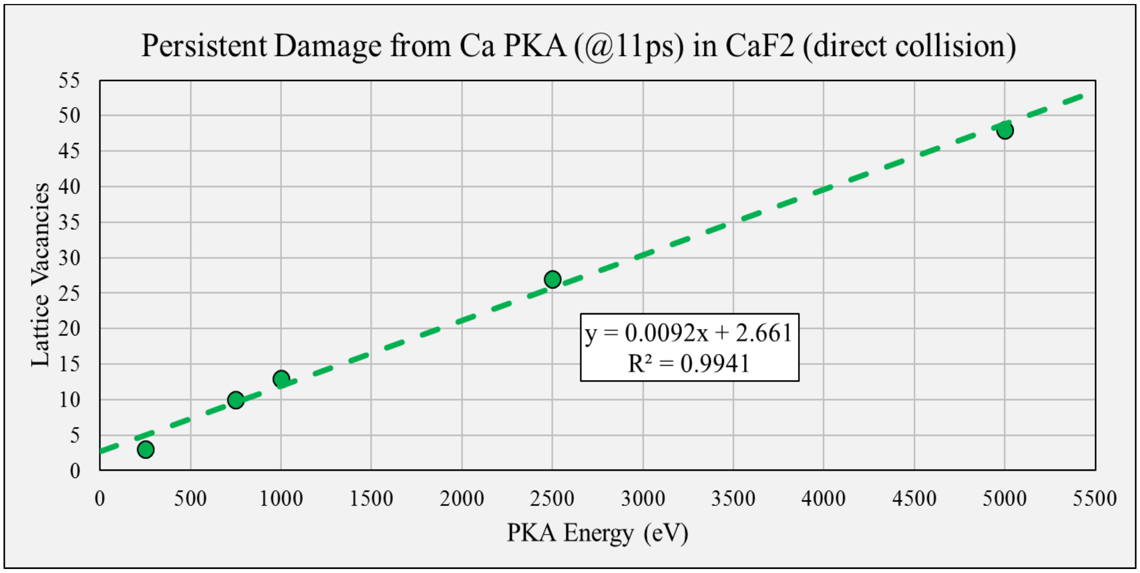

Figure 2.5.2: Plot and trendline for persistent damage at 11 picoseconds after initial self-annealing events. Equation and R^2 value define the trendline.

2.5.4 Fluorine PKA Cascade Results

Similar to the Ca PKA simulation, the listed energies in Table 2.5.1 for F were applied to F PKAs in a 2.5 million atom simulation to generate radiation damage statistics. Again, the total number of lattice vacancies/interstitial sites in the simulation cell over a period 11 ps. The results of this simulation are depicted in Figure 2.5.3.

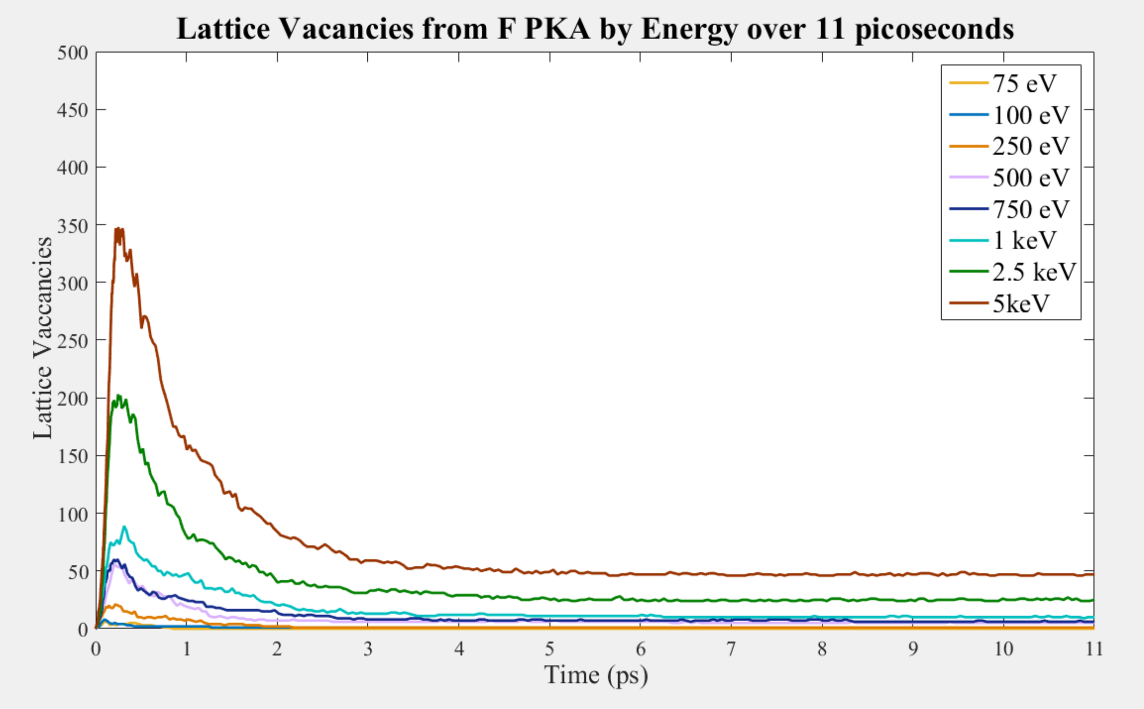

Figure 2.5.3: Plot of lattice vacancies by F PKA with varying energies from 0 to 11 picoseconds.

Figure 2.5.3 shows similar behavior to the vacancies plotted for a Ca PKA. There is an initial spike of damage that is not quite as dramatic as the spike produced by the Ca PKA, which is expected given the smaller mass of the F PKA in comparison to the Ca PKA. What was unexpected however was that the persistent damage due to PKAs of different type but the same energy was very similar despite the initial damage spike from the Ca PKA being about 28% greater. The F cascade had a recovery rate average of 85% compared to the 90% recovery rate from the Ca cascade. It is worth noting that the damage and recovery of the F PKA was much more erratic than that of the Ca PKA as is also clear from the plots. Figure 2.5.4 takes the persistent damage at 11 ps and applies a trendline to the data for an extrapolation of damage at higher energies. Similarly, an extrapolation was made for higher energies based on the equation given in Figure 2.5.4. This equation was determined through a curve fit of the data.

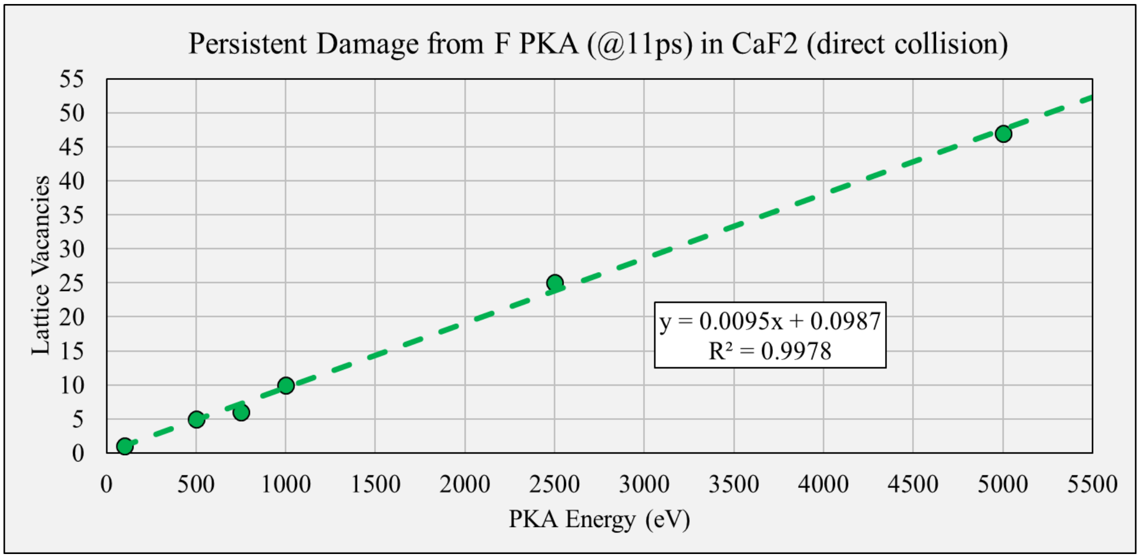

Figure 2.5.4: Plot and trendline for persistent damage from F PKA at 11 ps after initial self-annealing events. Equation and R^2 value define the trendline.

2.5.5 *LAMMPS Cascade Modeling Conclusions*

This simple analysis of a damage cascade within CaF_2 due to both Ca and F PKAs has produced some noteworthy results. It has been shown, for the PKA energy range between 100 eV and 10 keV, that the persistent damage existing after the self-annealing of the crystal structure is a linear function of the energy of the PKA. This suggests that when entering the MeV range, as would be the result of PuBe source neutrons and fusion neutrons seen later, that the higher the energy the more recognizable the damage should be. It should be noted again that extrapolating to high energies is likely to produce error as it is expected that, although the data suggests a linear relationship at very high PKA energies, there is likely a limit to the amount of damage that can be incurred due to the physical structure of the material.

In the experimental portion of this research the neutron energies that will be used are within the average energy of 3-5 MeV for the NH-3 Neutron Howitzer, reactor energies of a few MeV, and 2.5 MeV and 14.1 MeV for the Sandia Laboratory irradiations. It was discovered shortly after completing the first few runs within a LAMMPS simulation that, despite having access to the Center for Advanced Research Computing (CARC), high energy particles could not be simulated due to simulation size restrictions. The current simulation contains just over 2.5 million atoms and it can simulate PKAs with energies up to about 5 keV before atoms leave the simulation region. However, this simulation mostly exhausts the available resources and thus the best that can be accomplished is an extrapolation of the radiation damage to more relevant energies. It should be noted that this behavior may or may not be consistent at higher energies. It is, nevertheless, the best that can be done in the time frame required for this research. The maximum energy that can be transferred to a calcium (Ca) atom from a 5 MeV neutron is about 476 keV. Similarly, the maximum energy that can be transferred to a fluorine (F) atom from a 5 MeV neutron is about 950 keV. Given these energies as an approximate maximum for all but the 14.1 MeV source, and the extrapolation determined for both Ca and F PKAs, an approximate maximum expected number of persistent vacancies in CaF_2 would be 7,040 for Ca PKAs and 9,123 for F PKAs.

2.6 Modeling and Simulation Conclusions

Through probabilistic Monte Carlo analysis it was demonstrated that the TDE for Ca and F in CaF_2 are 32 eV and 20 eV, respectively. This determination of the TDE values enables continued research into understanding the connection between neutron damage and CaF_2 density, and thus refractive index change. Additionally, it was shown for PKAs within the energy region of 100 eV to 5 keV that the relationship between persistent damage, after initial self-annealing, has a linear relationship with the PKA energy at low energies. This may be nonlinear at higher energies, but is beyond the scope of the current simulation work.

Chapter 3: Measuring Refractive Index Change Optically

3.1 Overview

The basis of the research on relating refractive index change to neutron irradiations is a technique for high precision index of refraction measurements invented by Professor Jean-Claude Diels, who is leading the optics portion of this research. Through the utilization of a nested-cavity mode locked laser, the change of refractive index in a material can be measured with remarkable precision. Due to the nature of radiation damage caused by neutrons, this technique is ideal for tracking changes due to neutron irradiation. Because of the incident particle energy and momentum required to displace atoms in a lattice leading to the change of refractive index, this technique ignores the effects of gamma radiation; thus, this is a technique for gamma blind neutron characterization. This technique is ideal for scenarios where other detectors/dosimeters are blinded by the number of gamma rays in a system making it difficult to measure neutrons. This chapter will focus on the theory, setup, and calibration of nested-cavity mode-locked laser designed specifically for the purpose of measuring the change of refractive index in a material due to neutron irradiation.

3.2 Optical Methods for Measuring Radiation Effects

A primary portion of this research includes making a measurement of the changes in a crystal structure due to exposure to neutron radiation. The purpose of this research is to demonstrate that this can be done by tracking the change in the refractive index of a crystal. The general principle being that as radiation is absorbed in the crystal the density is changed and thus the refractive index changes. This generalization is well established and specifically for the application of radiation damage and effects was shown already in 1958 by W. Primak [5] with data plotted by S. Girard for SiO_2 [6]. Figure 3.2.1, shown previously and below, demonstrates how strongly the two track. This illustration follows electromagnetic theory on the correlation of dipole strength, here through the density of dipoles, which is related directly to the material density, and the magnitude of the refractive index. This is discussed in the next subsection. The damage and refractive index correlation is clear in other studies as well, such as with proton induced damage demonstrated by Gusarov [7].

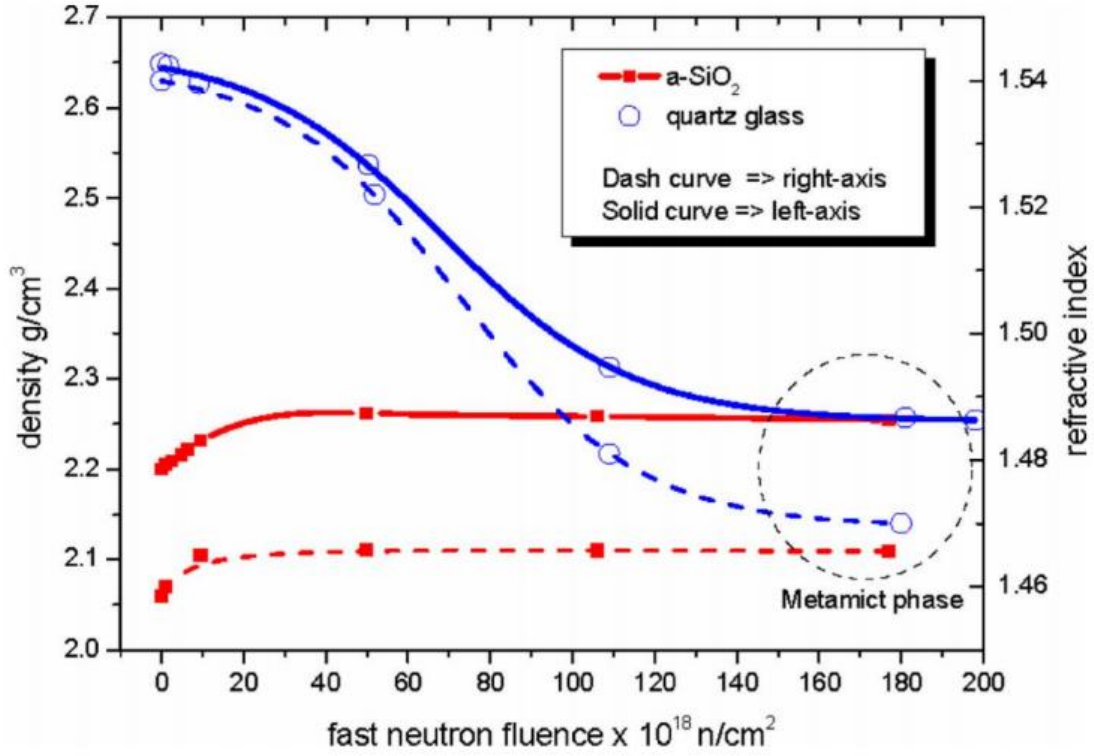

Figure 3.2.1: As higher energy particles enter a material they will naturally produce not just a single PKA, but rather will generate many PKAs that will in turn interact with other atoms within the lattice while the neutrons interact by collision with the nucleus

Utilizing a nested mode-locked laser cavity it is possible to measure the change in refractive index in a transparent material to a very precise degree. A brief proof of concept for CaF_2 was demonstrated to show that this technique provides very high precision measurements of the change of refractive index [9]. The utilization of this optical technique is of paramount importance to this work.

3.2.1 Refractive Index Overview

A critical piece of this research is the measurement of the change in refractive index. To better understand this concept this section will outline a couple basic optical science quantities of interest. It has been well established that when an electro-magnetic (EM) wave passes through a material the molecules within the medium are polarized by the oscillating electric field at the frequency of the propagating wave. The overall effect of this is that the EM wave is slowed down in comparison to its free propagation in a vacuum [46]. Each nonmagnetic dielectric medium has its own relative permittivity, ε_r with respect to the permittivity of a vacuum, ε_o. When defined with the absolute permeability, μ_o, the phase velocity of an EM wave can be defined by Equation 9.

$$V_p = \frac{1}{\sqrt{\varepsilon\mu}} \qquad \text{(Eq. 9) [47]}$$

Where $\varepsilon = \varepsilon_r \varepsilon_o$ and $\mu = \mu_r \mu_o$. Furthermore, the term phase refractive index is simply the ratio of the speed of light in free space and a waves velocity inside a medium or as the square root of the relative permittivity as shown in Equation 10.

$$n_p = \frac{c}{V} \approx \sqrt{\varepsilon_r} \qquad \text{(Eq. 10) [46] [47]}$$

The difficulty and the reason for the approximation in equation 10 is the fact that the n and ε are dependent upon frequency on the microscopic level. The fact that n is dependent on the wavelength of the EM wave is an effect termed dispersion. The index of refraction n is typically used to relate to the velocity of the oscillating wave, the phase, $n_p = v_p/c$ which should be specified as n phase, or n_p. Likewise, the velocity of the group of waves, the wave bunch, may be related via $n_g = v_g/c$.

Since perfect monochromatic waves exist only in theory, one must consider the velocity and index of a group of waves and how the dynamics change these quantities. Thus, the wave packet (containing an oscillating field) travels at a velocity defined as the group velocity shown in Equation 11,

$$v_g = \frac{d\omega}{dk} \qquad \text{(Eq. 11)}$$

where ω is the mean frequency of the oscillating field whose amplitude is modulated by the varying field of frequency $d\omega$ and dk is the wavevector within which the maximum amplitude moves [46]. ω is defined as

$$\omega = Vk = \left[\frac{c}{n(\lambda)}\right]\left[\frac{2\pi}{\lambda}\right] \qquad \text{(Eq. 12) [46]}$$

where n(λ) is written to explicitly show the dependence of the refractive index on the wavelength of light passing through it. After solving for v and differentiating to get v_g, Equation 13 is obtained,

$$V_g = \frac{c}{n - \lambda\frac{dn}{d\lambda}} \qquad \text{(Eq. 13) [46]}$$

where

$$n_g = n - \lambda \frac{dn}{d\lambda} \qquad \text{(Eq. 14) [46]}$$

These four quantities will be the building blocks in comparing the repetition rate of the FPE and the repetition rate of the laser cavity to determine the change in refractive index of a crystal sample due to irradiation damage. Phase velocity relates with the movement of the waves and the phase index of refraction, which is what is generally thought of when discussing the index of refraction. The group velocity is more clear in a classical dynamics sense when discussing movement of wave packets or bunches.

It has been shown already that refractive index and density are strongly correlated. This effect is actually secondary, as the primary reason for the correlation is the fact that density increases overall dipole density, or polarization density. This is a quantity of classical electromagnetism defined as the vector field in a dielectric material that expresses the density of induced electric dipole moments, where a dipole moment is the measure of the separation of the negative and positive charges in a system. Generally, as the density of a material increases or decreases (as is the case with neutron irradiation) the separation of the charges changes in a direct correlation with the density. In the case of decreasing density, the dipole moments become further apart (albeit on an extremely small scale but still significant). The increased spacing of the dipole moments decreases the capacitance and the polarization density which ultimately affect the permittivity of a medium. As stated previously in Equation 10 the refractive index of a material is approximately equivalent to the relative permittivity, ε_r, of a material. The permittivity of a material is determined using Equation 15,

$$\varepsilon_r = \varepsilon_0 * (1 + \chi) \qquad \text{(Eq. 15)}$$

where, ε_0, is the constant permittivity of free space and χ is the susceptibility, the macro-scale quantity of polarizability. Thus, in summary the reason changes in refractive index decreases with neutron irradiation is because neutron irradiation causes the atoms in a structure to become more spread out that they normally are. As such, the dipole moments are further separated causing a decrease in polarization density which in turn decreases the relative permittivity of a material, which is the essential building block of the refractive index.

3.2.2 Mode-locked laser cavity

The standard laser cavity is made up, minimally, of an optical resonator with two end mirrors and a laser gain medium. There are typically many modes contained within the optical resonator and the total output of the laser varies based on time, frequencies, amplitudes and relative phases of the oscillating modes [48]. For waves within a cavity of length L the allowed wavelengths, or frequencies, must satisfy the resonance condition of the cavity in order to achieve mode-locking, which, in the frequency domain, creates a frequency comb resembling a picket fence. The resolution of the resonance condition of the cavity along with that of the inserted FPE are detailed in Section 3.3.1.

A laser is said to be mode-locked when “the oscillating modes are forced to maintain equal frequency spacing with a fixed phase relationship to each other” with the output over time varying in a well-defined manner [48]. A mode-locked laser is made to produce extremely short pulse trains typically on the order of picoseconds with some in the range of single digit femtoseconds [49].

A mode-locked laser generates a frequency comb (an ultrashort pulse train that arises from the broadband spectrum) [50]. The modes of a frequency comb, f_m, are defined by two variables, f_0 and f_{rep}, the repetition rate and the carrier to envelope offset, respectively. This relationship is shown in Equation 16.

$$f_m = f_0 + mf_{rep} = \frac{\Delta\varphi}{2\pi\tau_{rt}} + m\frac{1}{\tau_{rt}} \qquad \text{(Eq. 16) [8]}$$

where τ_{rt} is the repetition rate of the cavity and $\Delta\varphi$ is the "carrier-to-envelope phase slippage." Because $\Delta\varphi$ comes about as a result of the difference between the phase and group velocity, the offset frequency, f_0, can be redefined as a function of the perimeter of the cavity, P, shown in Equation 17.

$$f_0 = \frac{\Delta\varphi}{2\pi\tau_{rt}} = \frac{\left(\frac{1}{v_g} - \frac{1}{v_p}\right)\omega_l P}{2\pi\tau_{rt}} = \frac{(n_g - n_p)\omega_l P/c}{2\pi\tau_{rt}} \qquad \text{(Eq. 17) [8]}$$

A general pictorial image of a frequency comb is depicted in Figure 3.2.2. In this image the time domain phase slippage relates directly to the frequency domain carrier-to-domain offset frequency, f_0, and the mode spacing in the frequency domain is inversely related to the repetition rate of the cavity, f_{rep} [8], where f_{rep} is defined simply as

$$f_{rep} = \frac{c}{2L}$$

where c is the speed of light and L is the length of the cavity. In other words, it is the inverse of the time it takes a laser pulse to make one round trip in the cavity.

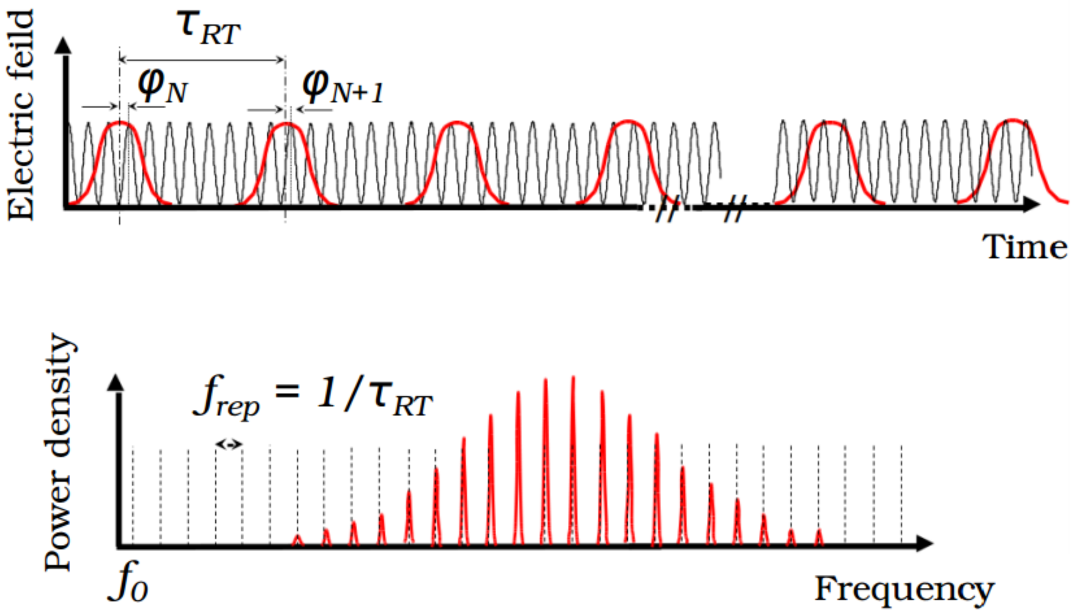

Figure 3.2.2: f_0 in this figure is the frequency domain representation of the round trip phase slippage, $\Delta\varphi$. The mode spacing is representative of the cavity repetition rate, f_{rep} [8].

A remarkable and key feature of the frequency comb generated in a mode-locked laser is that all present modes are evenly spaced according to the repetition rate (f_{rep}) of the cavity. They are also shifted by the carrier envelope offset f_0. Due to the fact that these quantities completely characterize the frequency comb they can be manipulated in such a way as to make “an ultra-sensitive measurement of a differential intracavity pulse shift” [8]. Another fact that is crucial to this research is the ability to lock the group index of refraction of the cavity, n_g, utilizing the counter propagating pulses generated by the mutual saturation of the pulse envelopes. Keeping n_g constant or at least consistent throughout experimentation allows for the isolation of n_p, the phase index of refraction. This ultimately allows for the determination of the change in the phase index of a Fabry-Pérot Etalon inserted into the cavity, which, for this work is a CaF_2 sample.

3.2.3 The Fabry-Pérot Etalon

One way to extract information about the propagating light waves is through interferometry, a technique in which waves are superpositioned. The first multiple beam interferometer was constructed in the late 1800's by Charles Fabry and Alfred Pérot. This type is now referred to as a Fabry-Pérot (FP) interferometer. An FP device, in general, consists of "two plane, parallel, highly reflecting surfaces separated by some distance d" [47]. The space between the mirrors can be filled with vacuum, air, or a transparent dielectric medium [51]. This is, however, the most simple form of a FP. Today there are many different, unique, forms in which a FP is built, depending on the application. When these mirrors are fixed in place and adjusted to maintain parallelism it is referred to as a Fabry-Pérot Etalon (FPE) [47]. This is the case for a single material with two parallel surfaces acting as a FP, as is done in this research with CaF_2. Because of the high resolution and simple design of a FPE it is commonly used as a high performance optical filter and a high-resolution spectrometer [8]. In this research the FPE is utilized within the laser cavity as a nested-cavity which allows for several very unique comparisons in the round trip time of the overall cavity, τ_{rep}, and the round trip time of the laser in the FPE, τ_{FP}.

This work utilizes a combination of these approaches to create a "nested cavity mode-locked laser". By placing an FPE into a laser cavity in this way a spectral modulation of the output from the laser is introduced. This produces several unique characteristics of the laser and the generated frequency comb that ultimately leads to a greater ability to perform high precision spectroscopy [8].

3.2.4 Generation of High Frequency Pulse Trains

As previously mentioned, a basic mode-locked laser cavity generates singular pulses in the time domain, separated in time by a factor determined by the length of the cavity. A general representation of the basic time domain output of a simple mode-locked laser cavity is depicted in Figure 3.2.3 where FM, depicts the focusing mirrors.

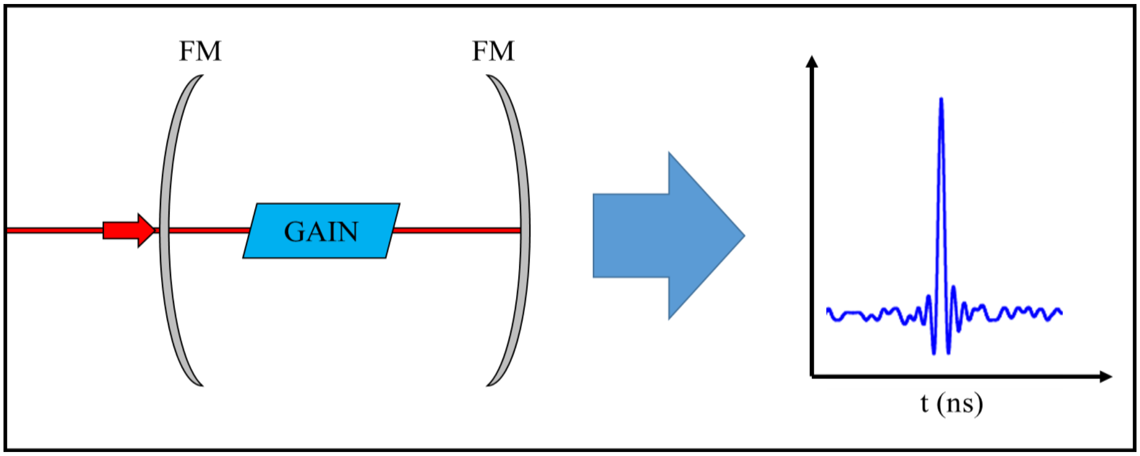

Figure 3.2.3: Demonstration of general function of a mode-locked laser cavity generating singular pulses in the time domain at a rate determined by the cavity length. The pumping laser enters from the left [8].

This pulse generation changes dramatically when inserting an FPE into the cavity. By inserting an FPE at an angle into the basic cavity above, a pulse bunch is created similar to the depiction in Figure 3.2.4.

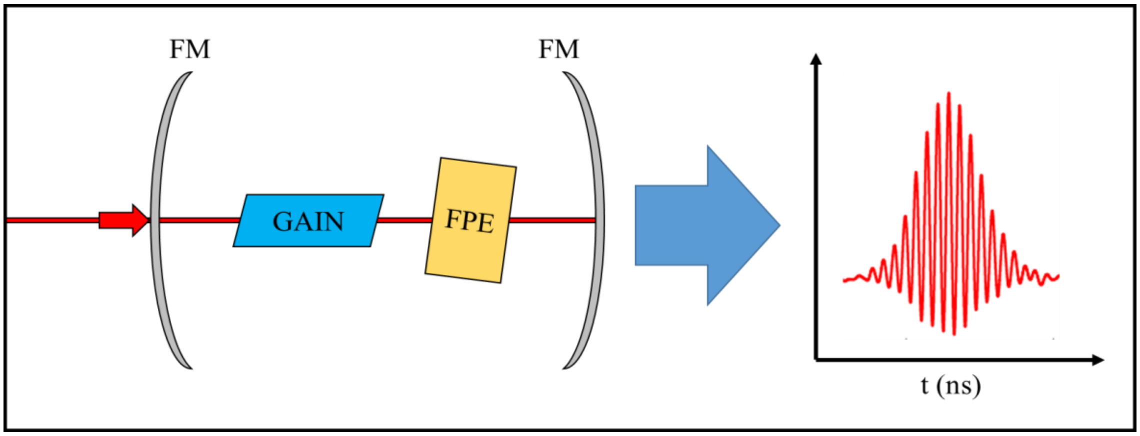

Figure 3.2.4: Depiction of general function of a nested cavity mode-locked laser cavity generating pulse bunches in the time domain at a rate determined by the cavity length. The separation of the peaks within the bunch corresponds to the effective length of the FPE [8].

The pulse bunch is due to the original cavity pulse from Figure 3.2.3 passing through the FPE. Through a series of internal reflections many pulse peaks leave the FPE in sequence; the intensity of the leading peak in the bunch is pushed back further in the bunch. The expected pulse shape is a sawtooth pattern, as shown in Figure 3.2.4, but after several passes with the intensity of each of the peaks diminished, a Gaussian shaped pulse bunch is created, as in Figure 3.2.4. The Gaussian shape was determined to be correct by Koji [52]. The generation and characterization of a high frequency pulse bunch within a nested-cavity mode-locked laser are performed in great detail by K. Masuda in his dissertation Intracavity coherent interaction of mode-locked pulse train with resonant medium [8]. This work will be briefly reviewed here for the purpose of understanding its impact on precisely measuring the change of refractive index. Short pulses passing through a FPE, with pulse widths smaller than the round trip reflection time within the FPE, are transformed into pulse trains by this internal reflection, as in Figure 3.2.5.

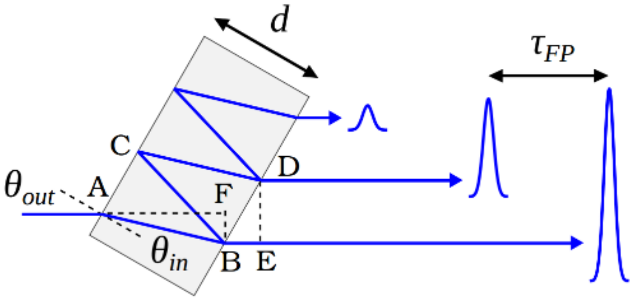

Figure 3.2.5: Pulse Propagation in an FPE assuming pulse duration is much shorter than the round trip time of the FPE [8].

The generation of the pulse bunch is a result of internal reflections of the laser pulse propagating through an FPE. The beam enters the FPE at point A in Figure 3.2.5. Each time the pulse encounters a face of the FPE, such as point A, B, C, D etc. in Figure 3.2.5, a portion of the beam is transmitted and a portion reflected. The portion that passes to B may transmit, giving the earliest pulse out of the FPE, or be internally reflected. The internally reflected portion from B may reflect off the first face, C in the figure, and return to the second face, D, where part of it may transmit, giving the second pulse out of the FPE, and part of it reflect. This continues for several internal reflections, with some of each portion transmitted in the direction of the first pulse, creating a pulse bunch. The intensity is expected to drop quickly as a function of pulse number within the bunch, but due to the multiple passes back and forth and the intensity thus being pushed back from the front pulse, many pulses become observable in the bunch, making this very useful for study.

If the pulse duration is much shorter than the round trip time of the FPE then the pulses are separated within the bunch and may be studied. There is a slight time separation of the pulses in the train due to the travel time within the crystal for the internal reflections.

When the pulses are sufficiently short, no interference occurs between pulses and the delay between pulses can be written as:

$$\tau_{fp} = \frac{2n_p d\ \cos\theta_{in}}{c} \qquad \text{(Eq. 18) [8]}$$

where $\tau_{fp}$is the round trip time of the FPE. Each subsequent reflection is displaced slightly from the optical axis; the displacement is a function of FPE angle. The repetition rate of the overall cavity will change with angle as well. Moreover, at a certain angle, depending on the type and thickness of the FPE used the nested-cavity mode-locked laser will transition to single-pulse mode-locking due to the fact that at this point the cavity loss of the multiply reflected pulses exceeds the gain.

Utilizing a fused-silica FPE, Masuda demonstrated that a standard nested-cavity mode-locked laser generates a somewhat Gaussian shaped pulse bunch [8]. A simulation of this is demonstrated by J. Hendrie who has shown that, due to the internal reflections in an FPE, along with the gains and losses of the cavity a Gaussian pulse bunch is generated. Due to reflection losses, this simulation for fused silica demonstrated an attenuation by a factor of $(0.04)^2$ [52] for each successive pulse reflection passing through the FPE.

With regard to the round-trip time of the cavity, this pulse bunch travels in a similar fashion to the pulse in a standard mode-locked laser. This behavior is shown in Figure 3.2.6 where a partially resolved intensity profile of individual pulses is demonstrated [8]. In this example, the cavity repetition time of 6.4 ns corresponds with a repetition rate of 156 MHz and the FPE repetition time of 148 ps corresponds with a repetition rate of 6.76 GHz.

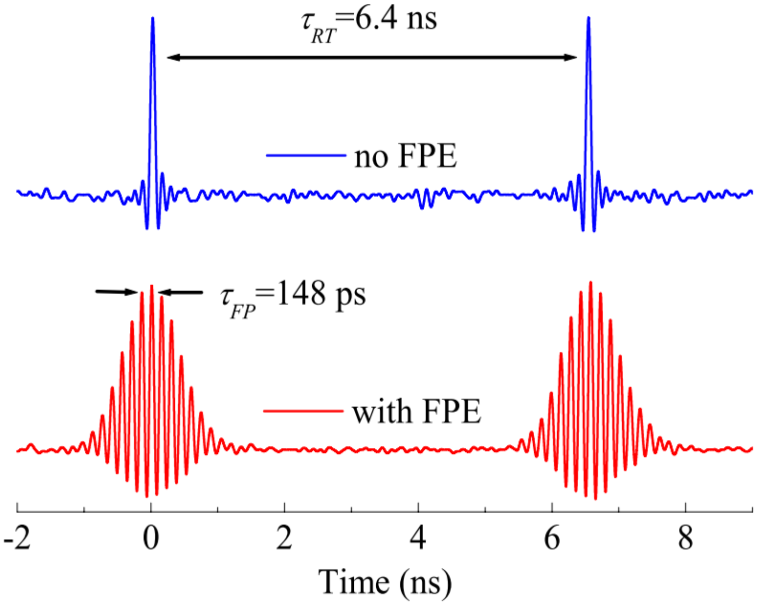

Figure 3.2.6: The output of a nested-cavity mode-locked laser (bottom) as it is compared to that of an identical cavity not containing an FPE (top) [8].

The frequency space representation of the simple mode locked laser pulsing without the FPE is a frequency comb, as in the top of Figure 3.2.7. When measuring the frequency space representation with the FPE, with pulse bunches, the frequency comb has an envelope, as seen in the bottom of Figure 3.2.7.

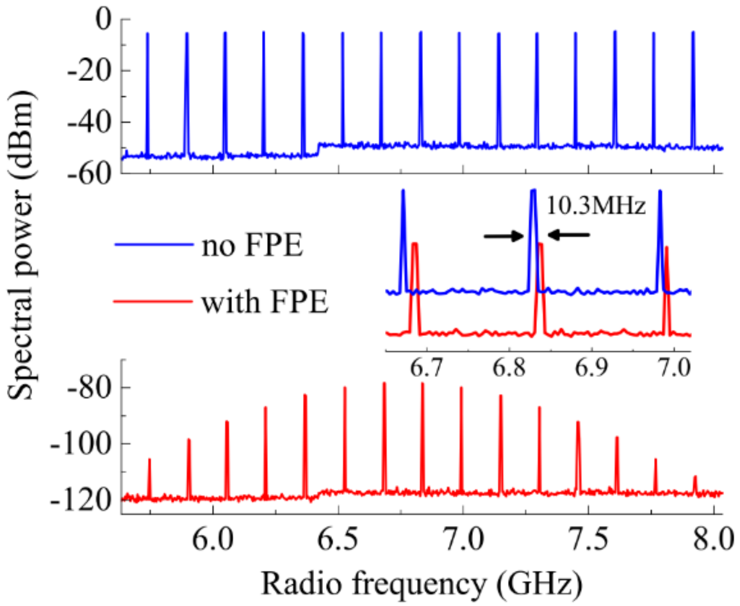

Figure 3.2.7: The RF spectrum of a single mode-locked laser (Top) containing no FPE. The RF spectrum of a nested-cavity mode-locked laser (Bottom) with 15 mm fused silica FPE. The repetition rate of both lasers were set to the same value. The inset plot (Middle) demonstrates train shift resulting from the formation of pulse bunches [8].

The width of the envelope pictured in the bottom of Figure 3.2.7 is determined by the time domain extension of the pulse bunch. The frequency offset shown in the inset figure in Figure 3.2.7 is a consequence of the differences in velocity of the pulse bunch envelope and the individual pulses. For this example, from our research group's work in [44], the center of the envelope is at 6.76 GHz, following the FPE behavior, and the spacing between teeth of the comb is 0.156 GHz, following the cavity behavior.

In the current work the FPE utilized is CaF_2, with a thickness of 15 mm and a diameter of 25.4 mm and 20.3 mm depending on the experiment. The thickness is the only parameter of great importance here as that determines where in the frequency space the representation of the pulse bunches will appear. The more thin an FPE is the shorter the

FPE repetition rate and the higher the frequency will be. With frequency considerations and the 27 GHz spectrum analyzer we were able to acquire for this research, a 15 mm thickness was deemed appropriate. A picture of the standard FPE utilized in this work is shown in Figure 3.2.8.

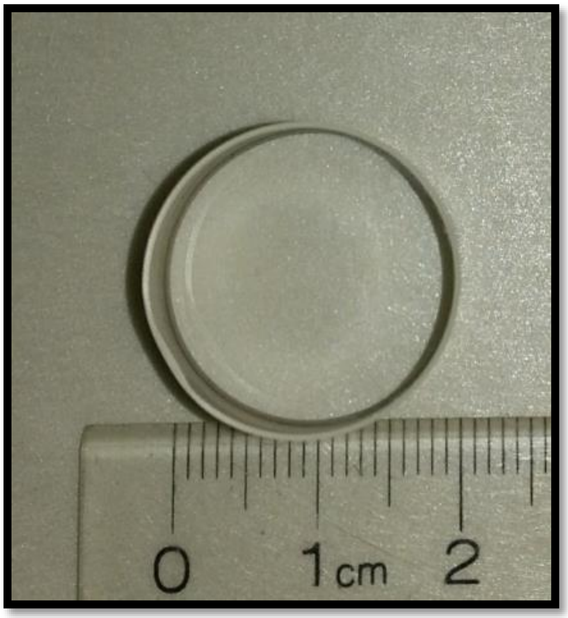

Figure 3.2.8: Picture of a CaF_2 FPE utilized in this research. This FPE is the 20.3 mm diameter sample.

3.3 Measuring the Change of Refractive Index Optically

3.3.1 Coupling Resonance Conditions of an FPE in a nested-cavity

As discussed earlier the resonance condition is an equation that must be satisfied in order to achieve mode-locking in any laser cavity. However, in a nested cavity such as the one discussed in this work, to achieve mode-locking the resonance condition of the FPE and the laser cavity must be satisfied at the same time. These two resonance conditions are [52]:

$$\frac{2\omega_0 L n_{p-l}}{c} = 2\pi N_l \qquad \text{(Eq. 19)}$$

$$\frac{2\omega_0 d n_{p-fp}\cos\theta}{c} = 2\pi N_{fp} \qquad \text{(Eq. 20)}$$

where ω_0 is the mode frequency, L and d are the lengths of the laser cavity and the thickness of the FPE, respectively, n_{p-l} and n_{p-fp} are the phase refractive indices of the cavity and the FPE, respectively, and N_l and N_{fp} are integer values, the mode numbers for the resonance of the cavity and FPE, respectively. Each of these is a function of the conditions of the system, the laser cavity length, and the PFE thickness and angle. When the ratio of the two conditions is compared, it leads to the resonance condition of the combined FPE-laser cavity system [52]:

$$\frac{L}{d\cos\theta} = \frac{n_{p-fp}N_l}{n_{p-l}N_{fp}} \qquad \text{(Eq. 21)}$$

Remarkably, this condition is satisfied passively in a free-space configuration described in [52]. The round trip travel time for the FPE (τ_{fp}) and the cavity (τ_l) are given by

$$\tau_{fp} = \frac{2d n_{g-fp}\cos\theta}{c} \qquad \text{(Eq. 22)}$$

$$\tau_l = \frac{2L n_{g-l}}{c} \qquad \text{(Eq. 23)}$$

where n_{p-fp} is the phase index of refraction of the FPE. Also, n_{g-c} and n_{g-fp} are the group indices of refraction of the laser cavity and the FPE, respectively. The inverse of these round trip times are the low (ν_l) and high (ν_{fp}) frequency components, respectively, described above. Taking the ratio of the frequencies and substituting L from equation 21 gives:

$$\mathcal{R} = \frac{\nu_l}{\nu_{fp}} = \frac{c n_{p-l} N_{fp}}{2d\cos\theta\, n_{p-fp} N_l n_{g-l}} \frac{2d n_{g-fp}\cos\theta}{c} = \frac{n_{p-l} n_{g-fp}}{n_{g-l} n_{p-fp}} \frac{N_{fp}}{N_c} \quad \text{(Eq. 24)}$$

Equation 24 is also referred to the LF/HF ratio. Unlike the previous equations, the ratio is not explicitly dependent on the FPE thickness or angle or the cavity length, though those play into the particular resonance condition integers, but on the various refractive indices and resonance modes. While the modes, N_{fp} and N_c, are integers, the ratio N_{fp} / N_c is a constant but not necessarily an integer [52]. Additionally, n_{g-fp}, n_{g-l}, n_{p-l}, the group index of the FPE, the group index of the laser cavity, and the phase index of the laser cavity, respectively, do not vary significantly compared to the expected change in n_{p-fp} due to irradiation. This allows for the isolation of n_{p-fp} and ultimately a determination of the change of the phase index of refraction in the FPE.

3.3.2 Mode-Locked Laser Cavity Pulse Width

A mode-locked laser cavity depends on a number of cavity characteristics, s discussed in the theory Section 3.2.2. One such characteristic needed to ensure optimal operation with a Fabry-Pérot Etalon inserted into the cavity is the laser pulse width in time. Minimizing the laser cavity pulse width has been a subject of experimentation for several decades resulting in some astonishing feats [49]. To date there have been publications of pulses smaller than 1 femtosecond [53]. For this work, however, single picosecond range pulses will suffice. A one picosecond pulse corresponds to a length of approximately 0.3 mm in a vacuum. The thickness of the CaF_2 FPE samples in this research is 15 mm. In order to produce stable frequency combs, the single length of a pulse must be able to be contained within the FPE, leading to a more relaxed pulse length requirement. Laser beam pulse widths can be measured precisely utilizing technique developed by J.C. Diels referred to as an interferometric autocorrelation [54] [55]. Figure 3.3.1 demonstrates the results of this type of autocorrelation with the figure scaled to clearly depict the pulse width of the linear laser cavity used in this research before the insertion of the FPE.

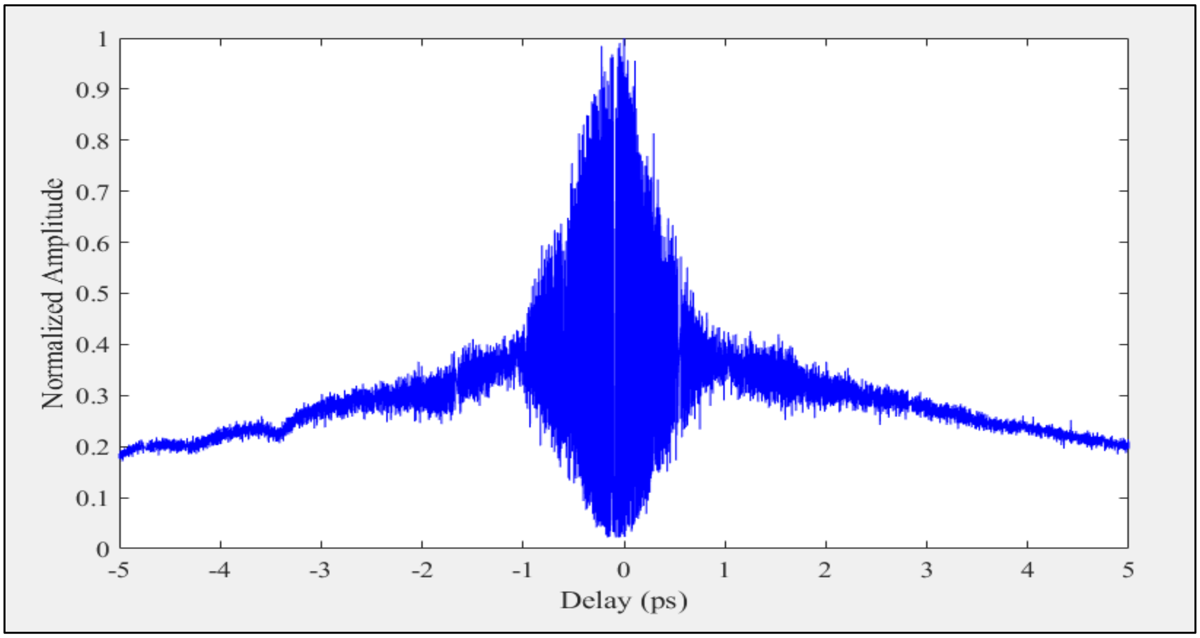

Figure 3.3.1: Plot of an Interferometric Autocorrelation of the linear laser cavity without an FPE operating at 7.01W and 790nm.

Figure 3.3.1 demonstrates a pulse width of less than 2 picoseconds prior to FPE insertion. This measurement meets the requirements for this research and provides a stepping point for FPE insertion and a repeat of the pulse width measurement with the FPE inserted. Figure 3.3.2 demonstrates the results of the autocorrelation with multiple pulses.

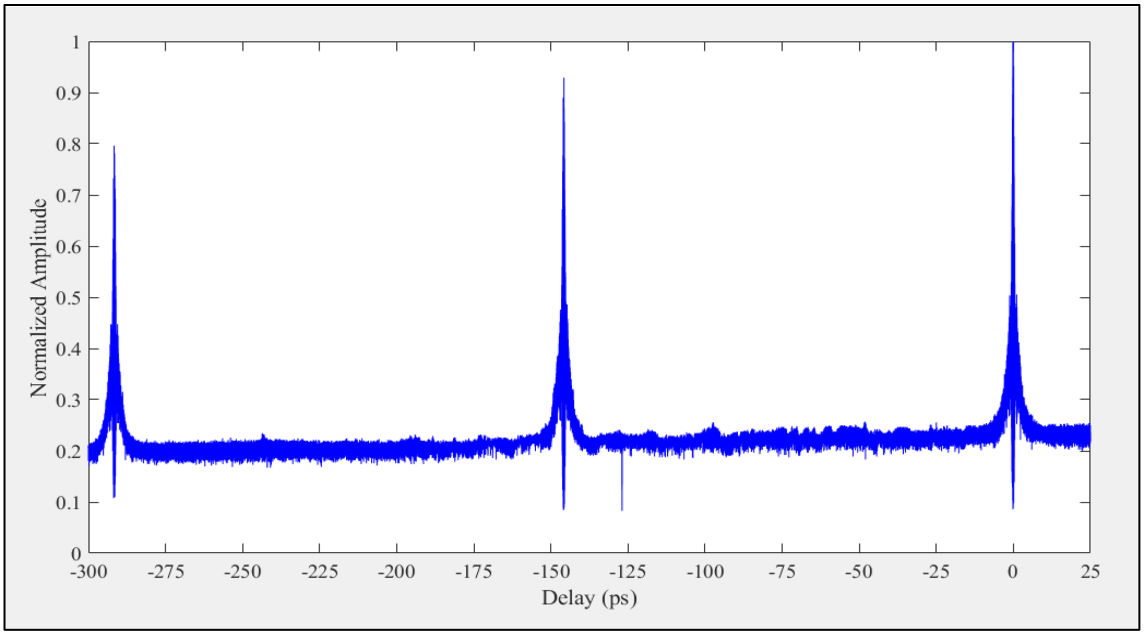

Figure 3.3.2: Autocorrelation plot showing the multiple pulse train caused by the insertion of the CaF_2 *FPE insterted at an internal angle of 8 mrad into a linear laser cavity operating at 7.01W and 790nm.*

Notice in Figure 3.3.2 that the separation in picoseconds corresponds to the repetition rate of the FPE, which is approximately 145.75 ps, corresponding to a frequency of 6.861 GHz. This is mirrored in the frequency comb separation when viewing the frequency space representation of the pulse train. The addition of the FPE to the cavity necessarily changes some of the cavity characteristics and it was appropriate to run another autocorrelation after FPE insertion to ensure that the pulse width is still within a manageable range. A close-up view of the autocorrelation conducted after the FPE was added into the laser cavity is shown in Figure 3.3.3.

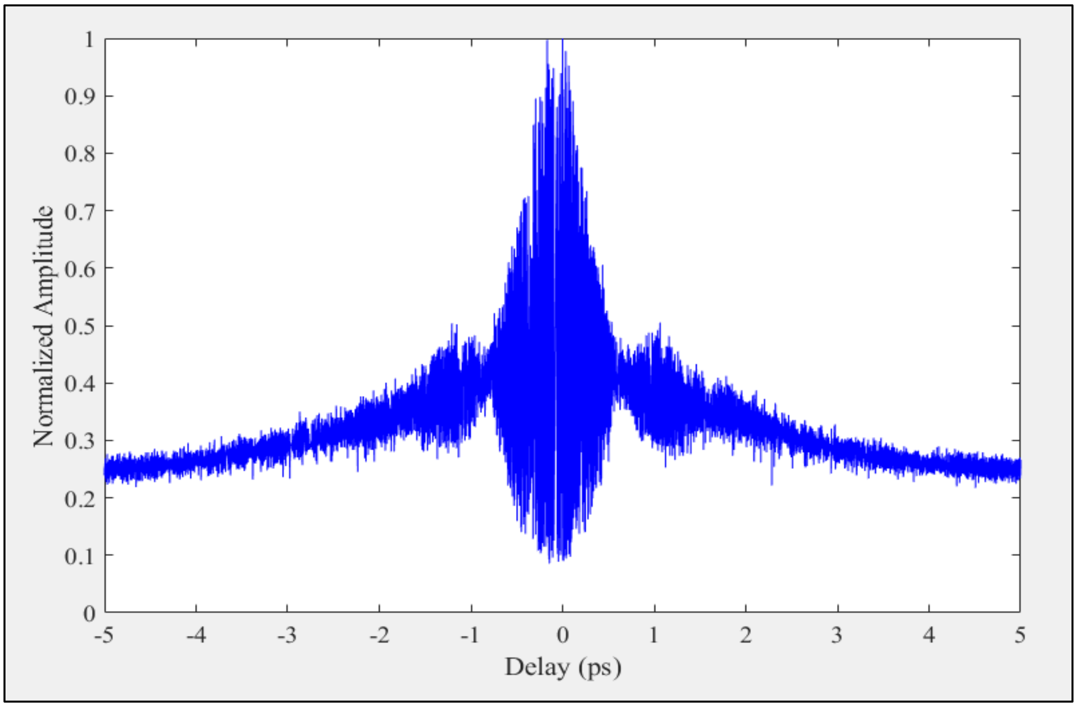

Figure 3.3.3: Enhanced plot central pulse of an Interferometric Autocorrelation of the linear laser cavity operating at 7.01W, 790nm, with a CaF_2 FPE inserted at an internal angle of 8 mrad.

Figure 3.3.3 shows that with the insertion of the FPE the pulse width has decreased slightly and is approximately around 1 to 1.5 picoseconds. This is still well within the necessary range and thus the next aspect of the research commenced with the examination of the pulse bunches in the time domain and frequency space.

3.3.3 Nested-Cavity Pulse Bunches and Frequency Combs

The time domain output of this setup is represented well in Figure 3.3.4 showing two laser pulses within the cavity occurring about 8.5 ns apart corresponding to a frequency value for the repetition rate of the laser cavity of approximately 117.582 MHz. Another point worth noting in this image is the separation between each peak corresponds to the repetition rate within the Fabry-Pérot which directly depends on the refractive index.

Tracking the change in both quantities is what allows for the high precision measurements of change in refractive index to be accomplished.

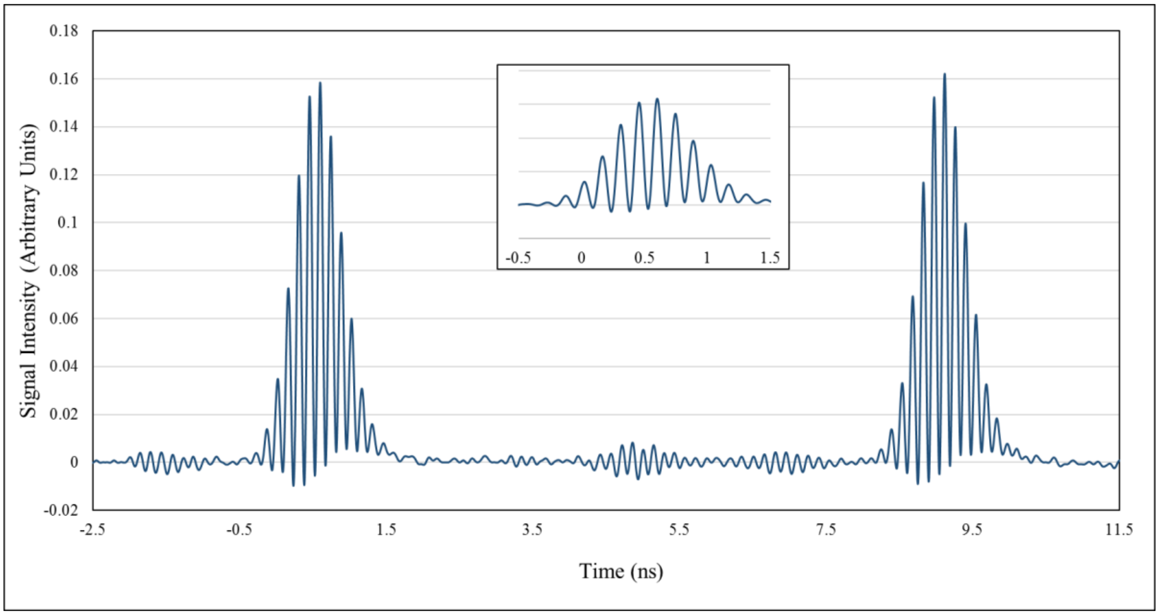

Figure 3.3.4: Time domain representation of two pulse bunches within the laser cavity setup. The inset plot shows a close up of the first pulse bunch.

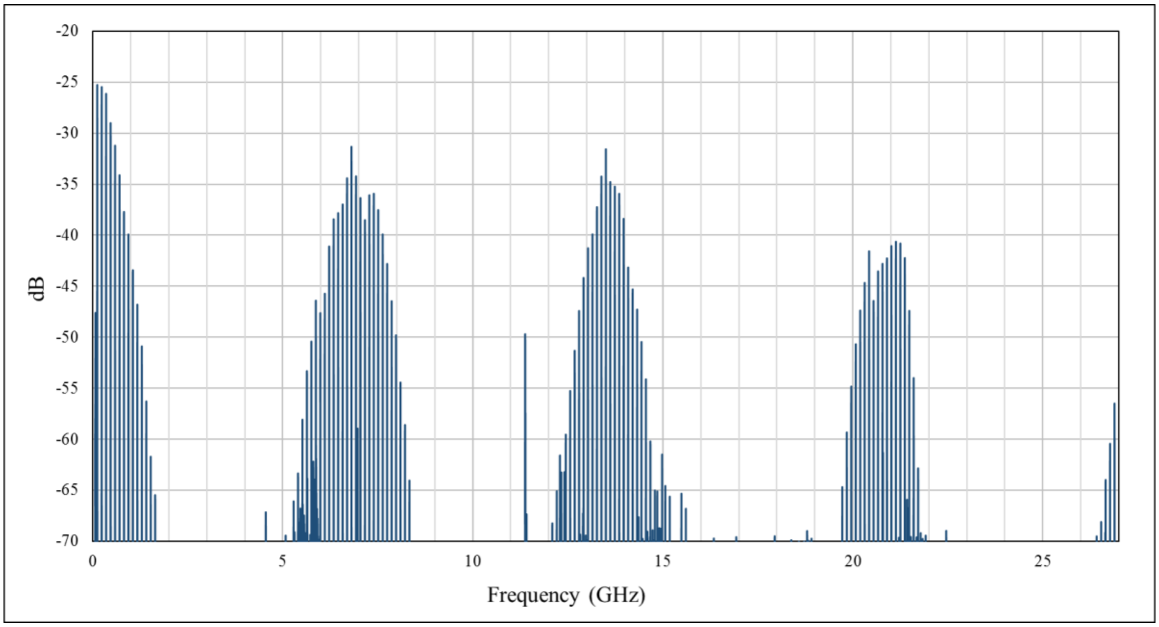

Figure 3.3.5: Frequency domain representation of the pulse bunches within the laser cavity, featuring well defined frequency combs whose central peaks correspond directly to the repetition rate of the FPE.

The frequency domain output of this setup is represented in Figure 3.3.5 which now shows the frequency combs characteristic of a mode locked laser with the envelopes caused by the addition of the FPE. The separation of the center peak of each envelope is equal to the repetition rate (referenced in Section 3.3.1 as 6.861 GHz) of the pulse from the FPE in frequency space. When the either the angle or length of the laser cavity is changed while keeping everything else constant the location of the observed peaks to the right and left of the center peak in the bunch move further away from the central peak at increasing rates depending how far the observed peak is away from the central peak. This also changes with a swelling of the crystal and thus a change in phase refractive index. This allows for comparison of a pre- and post-irradiated sample. As a result, when comparing the pre- and post-irradiated sample as the FPE angle or cavity length are changed the ratio of the frequency ratios will correspond directly to the change in refractive index.

3.3.4 Quantifying the Change in Refractive Index

The next vital step to this research is the ability to utilize the low-frequency to high-frequency ratio in Equation 24 to extract the change in the refractive index of a material after a sample is irradiated. This can be accomplished only when keeping all parameters (primarily the cavity gain and losses) in the cavity constant except for $n_{p,fp}$, the phase refractive index of the FPE. In order to extract this quantity a comparison of the pre-irradiated sample and the post irradiated sample must be performed. The frequency ratio can then be compared before and after crystal damage occurs to measure the change of refractive index in the FPE. This comparison, shown below in Equation 25 in a ratio of the LF/HF ratios from Equation 24, is to be called a super ratio for this work. This is a function only of the phase index of refraction of the FPE - the crystal sample - if all other values can be kept constant. The super ratio for crystal 0 and 1 (for example representing pre- and post-irradiation ratios) then is expressed as

$$\mathbb{R} = \frac{\mathcal{R}_0}{\mathcal{R}_1} = \frac{n_{p,fp,1}}{n_{p,fp,0}} = \frac{n_{p,fp,0}+\Delta n_{p,fp}}{n_{p,fp,0}} = 1 + \frac{\Delta n_{p,fp}}{n_{p,fp,0}} \qquad \text{(Eq. 25)}$$

This super ratio can also be utilized to correct for long term shifts such as thermal effects on cavity length and assess the error in such a correction as it is applied to the super-ratio of the pre- and post-irradiated sample.

The desired quantity to be extracted is $\Delta n_{p,fp}$, the change in the refractive index of a material. The change in refractive index can then be extracted by adjusting Equation 25 to give:

$$\Delta n_{p,fp} = (\mathbb{R} - 1)\, n_{p,fp,0} \qquad \text{(Eq. 26)}$$

3.3.5 Angular and Cavity Length Dependence

The super-ratio can be taken in a point by point comparison of ratios between two samples. There are two primary ways to keep all parameters (except $n_{p,fp,1}$) unchanged while taking several measurements. This can be accomplished with an angle scan, depicted in Figure 3.3.6, in which the overall length of the laser cavity is kept constant while the internal angle of the FPE is gradually changed from a relatively high angle (about 20 mrad for CaF_2) to the zero angle of the FPE at which point mode-locking in the laser cavity does not exist. The scan can be taken from some high angle, through zero, which is extremely clear in the laser behavior, all the way to the same relative point on the other side of the zero angle, but this is not necessary to make the comparison required by this research.

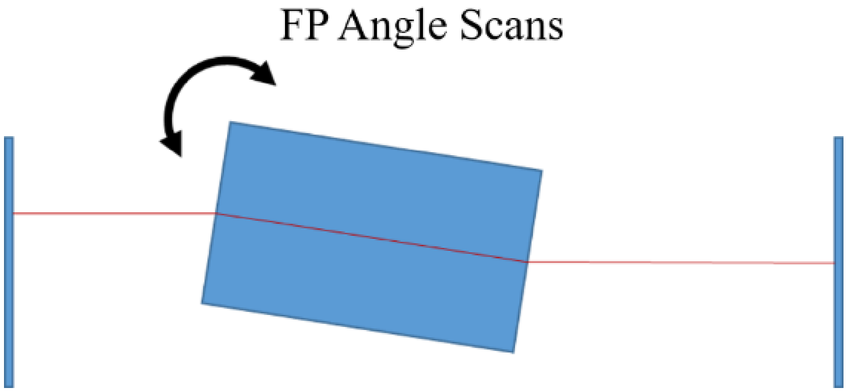

Figure 3.3.6: A simplified depiction of a laser cavity emphasizing the constant cavity length requirement for an angle scan to determine the refractive index change of an FPE.

In a similar fashion, the other method of obtaining the necessary parameter consistency while taking several different data points, is varying the length of the laser cavity while keeping the FPE angle constant. A difficulty in this measurement is ensuring that the angle of the scan is always the same between trials. When removing the sample from the laser cavity for irradiation it is difficult and improbable that when a sample is placed back in the cavity it will be at the identical location and angle as it was previously. In order to ensure repeatability to an acceptable degree of error an angle scan must first be completed in order to determine the zero angle of the FPE. Upon completion of this step the required angle position can be calculated. At this point the angle is only subject to the error of the motor driving the micrometer screw that sets the angle of the FPE, which has a quoted bi-directional repeatability of < ±1.5 μm, corresponding, in this experimental setup to a tilt angle of ±0.275 mrad [56]. A simplified depiction of a cavity length scan is shown in Figure 3.3.7. A detailed comparison of the accuracy and error of angle scans and cavity length scans is contained in Section 3.5.

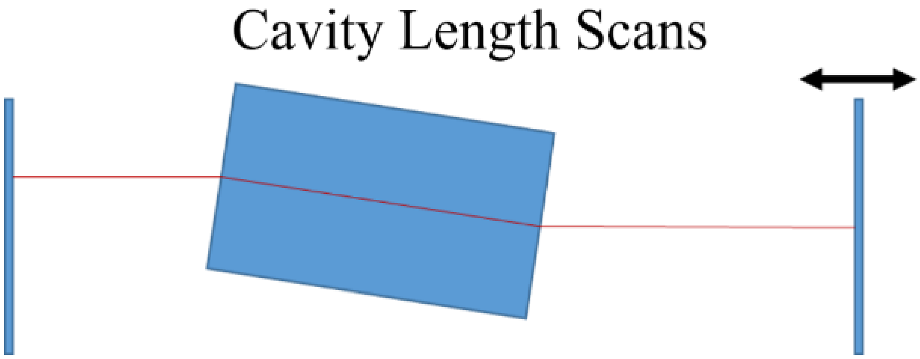

Figure 3.3.7: A simplified depiction of a laser cavity emphasizing the constant FPE angle requirement for a cavity length scan to determine the refractive index change of an FPE.

It should also be noted that it is possible to perform this analysis by taking numerous data points at one particular angle and cavity length. However, due to the current laser cavity setup and the difficulty in returning to the precise cavity length it is better to take a series of data points while systematically changing the cavity length. This is primarily due to the fact that the majority of the laser cavity is passing through an air medium, and the quality, content, and attributes of the air such as, humidity, temperature, and pressure all affect the effective cavity length. For a portable version of this system a fiber may take the place of an open air cavity.

3.3.6 Finding the FPE Zero Angle

While the cavity length scan has been shown through careful examination in this research to be a more accurate method of gathering data to determine the change in the refractive index there is an additional complexity to ensure the accuracy and precision of the measurement. This complexity is the determination of the Zero Angle. The Zero Angle of the FPE is the point at which the laser will stop mode-locking in a cavity due to the beam interference caused by the extremely small internal angle of the FPE. While in a typical laser cavity mode-locking will actually stop at a series of internal angles surrounding the zero angle it is the actual zero angle that must be determined accurately in order to determine the actual position of the zero angle. Fortunately, there are several ways to accomplish this. The method settled on for this research utilizes a photodetector to determine the strength of the laser beam. Figure 3.3.8 demonstrates the placement of the photodetector outside of the cavity.

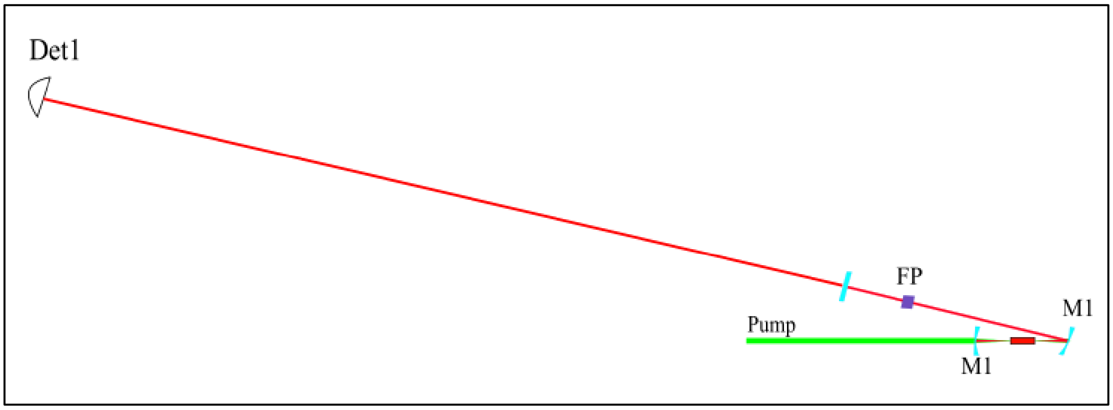

Figure 3.3.8: Demonstration of the position of the Photodetector (Det1) with respect to the standard laser cavity comprised of two focusing mirrors (M1) and a Fabry-Pérot Etalon (FP).

In order to increase accuracy of zero angle determination a photodetector is placed at a position as far from the cavity as possible to allow for greater precision measuring the reflections from the FPE as they begin to overlap at small internal angles. When approaching zero angle the response the photodetector will continue to get stronger until the internal reflections of the FPE begin to interact. Due to their interaction, the intensity of the light will diminish locally creating a valley in the detected voltage. Zero Angle is determined to be at the local minimum of the detected voltage from the photodetector. Figure 3.3.9 provides a generalized representation of this data.

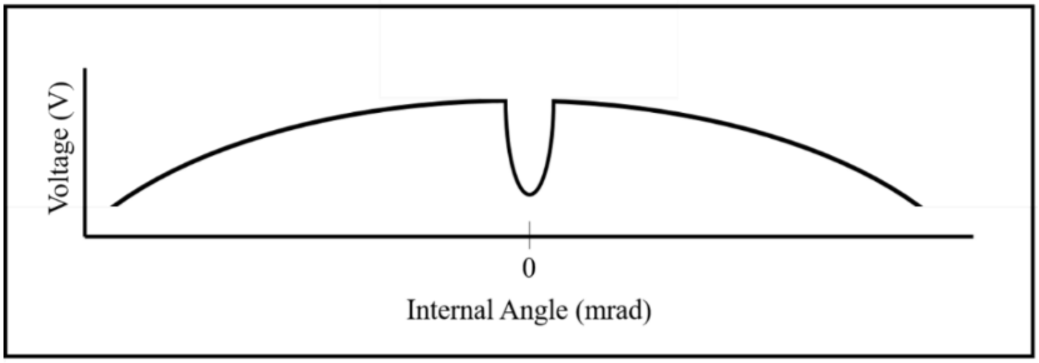

Figure 3.3.9: Generalized ideal depiction of the photodetector data as the internal angle of the FPE is adjusted from a high positive internal angle to a high negative internal angle.

It is only after performing a long scan through FPE internal angles that the zero angle can be determined. After the zero angle in determined, then a cavity length scan can be performed by utilizing the zero angle to determine the position of the internal angle of interest and setting the FPE to the desired angle.

3.3.7 Reproducing Cavity Length Range

Although it is not quite as crucial it is certainly important to ensure that the cavity length remains similar between all experimental results. The necessity of this is diminished by performing cavity length scans instead of performing scans at only one specific cavity length. At the start of each cavity length scan the repetition rate of the cavity is compared to that of a previous scan. This ensures that the cavity length is similar between all measurements.

3.4 Experimental Setup

As discussed in the theory Section 3.2, the setup for measuring refractive index change in a material consists of a laser cavity containing two parallel end mirrors, a gain medium, and a FPE. A more detailed rendering with the additional components included in this setup is shown in Figure 3.4.1.

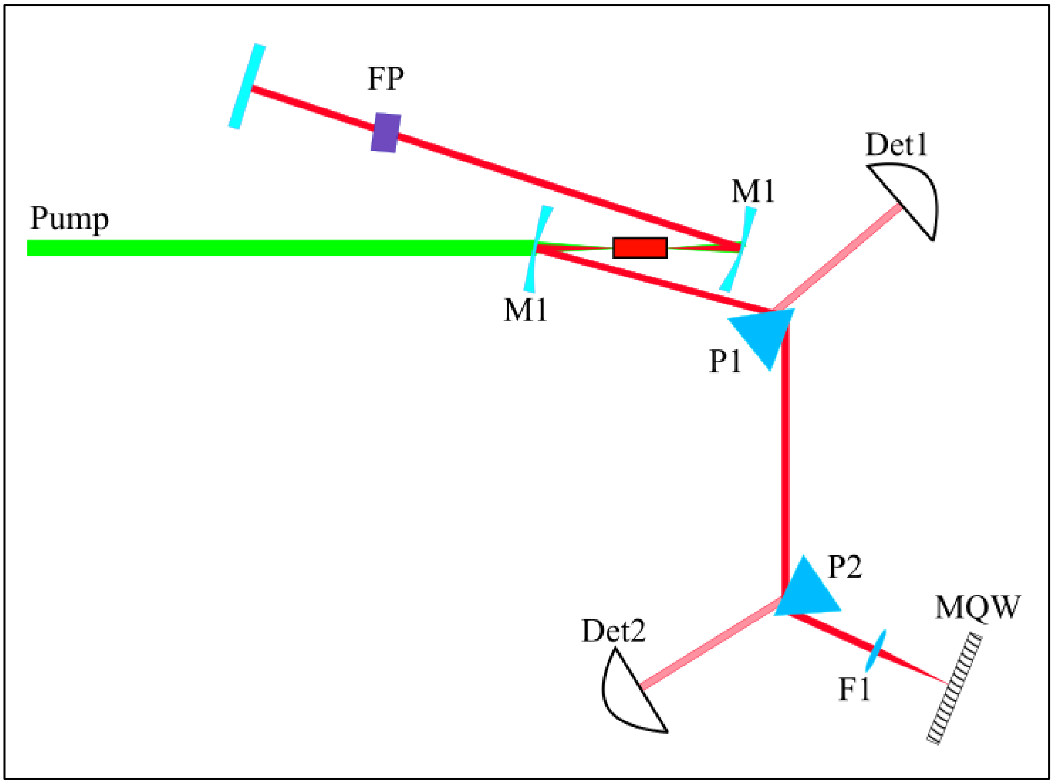

Figure 3.4.1: A detailed rendering of the laser cavity setup for measuring refractive index change in a material, where M1 is the focusing mirror, P1 and P2 are prisms, MQW is the Multiple Quantum Well, F1 is the Focussing Lense, Det1 and Det2 are the Low Frequency and High Frequency detectors, and FP is the Fabry-Pérot Etalon.

Figure 3.4.1 shows more components than discussed previously in the theory sections. This includes the presence of a multiple quantum well (MQW), an end mirror, two prisms, two focusing mirrors, and two detectors. The MQW acts as one of the two end mirrors and due to the associated energy band gaps of the material acts to stabilize the laser beam within the cavity. The prisms act to decrease the dispersion of the light within the cavity, allowing only a narrow wavelength band along the correct path, also aiding in stability the laser beam as well as the frequency combs in frequency space. The focusing mirrors focus the beam into the gain medium. Lastly, one detector is used to measure the repetition rate of the cavity and one is utilized to measure the repetition rate of the FPE.

3.5 Laser Cavity Calibration and Repeatability Measurements

3.5.1 Cavity Length Scans vs. Angle Scans

In order to be able to quantitatively state that the refractive index has changed, both stability and noise must be assessed. A set of experiments were completed to measure the repeatability of the data taken using unirradiated crystals in preparation for the irradiated sample measurements. The experiments consisted of both cavity length scans and FPE angle scans. Four trials consisting of four scans each were completed. In between each trial the CaF_2 FPE was removed from its holder in the laser cavity and placed back in a few moments later to test placement repeatability and associated changes in the data. For true irradiation measurements, the samples will need to be removed in order to be taken to be irradiated and thus this measurement is a critical one in demonstrating repeatability. In addition, this set of experiments was completed over a period of 2-3 different days to track the noise due to environmental changes from day to day.

The angle scans were completed varying the internal angle of the FPE from about +8 mrad to -4 mrad, where the zero angle, previously discussed, is defined as 0 mrad. The following figures demonstrate a function of the frequency ratios, where the repetition rate of the FPE in Hz is divided by the repetition rate of the laser cavity in Hz (recall Equation

24). In order to assess the stability more clearly for this particular experiment the LF/HF frequency ratio was inverted to HF/LF. (This is the only experiment which required the inversion of the frequency ratio and as such when the frequency ratio is quoted in the remainder of this work it generally refers to the repetition rate of the cavity divided by the repetition rate of the FPE). The ratio was then multiplied by the ratio of the number of modes in the FPE to the number of modes in the cavity and is subtracted by one in order to more clearly address the stability of the data. By multiplying out the ratio of modes the only values remaining are the ratio of the phase and group indices for the cavity and the FPE. Because the ratio of the indices will be a value minimally greater than one by subtracting one the assessment of stability is much more clear. The equation is presented below:

$$\frac{1}{\mathcal{R}}\frac{N_{fp}}{N_c} - 1 = \frac{n_{g,c}n_{p,fp}}{n_{p,c}n_{g,fp}}\frac{N_c}{N_{fp}}\frac{N_{fp}}{N_c} - 1 = \frac{n_{g,c}n_{p,fp}}{n_{p,c}n_{g,fp}} - 1 \qquad \text{(Eq. 27)}$$

The figures in this section have the y axis label “Inverted Frequency Ratio – 1” in reference to Equation 24. This step would not be done in the case of Equation 25 because the order is intrinsically divided out of the equation when taking the super-ratio. Figure 3.5.1 shows the average ratio of each trial point by point, plus and minus the standard deviation of each respective trial from March 8, 2016. The four separate colors represent the average of each of the four separate trials demonstrating the variation in each of the trials, after which the sample was removed and placed back into the cavity to test placement stability. Figure 3.5.2 shows the overall average ratio for the four trials of four angle scans each on March 8, 2016, presented point by point in blue plus and minus the overall standard deviation with boundaries in red.

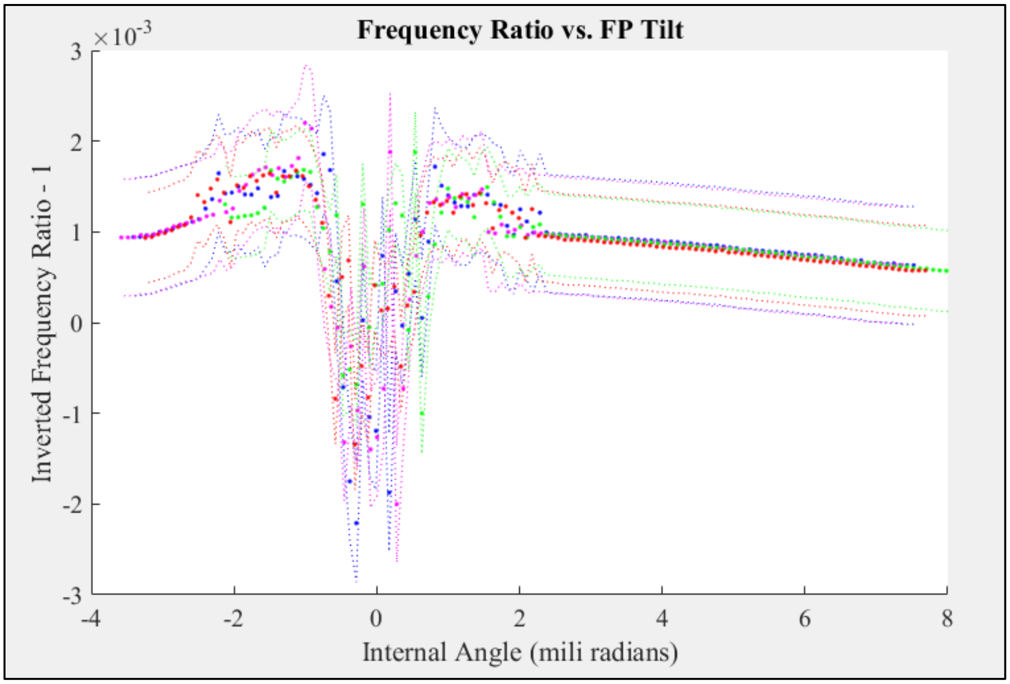

Figure 3.5.1: Frequency ratio data for each of four separate angle scan trial on March 8, 2016, each represented by a different color and associated dotted line representing the standard deviations of each point in the trial.

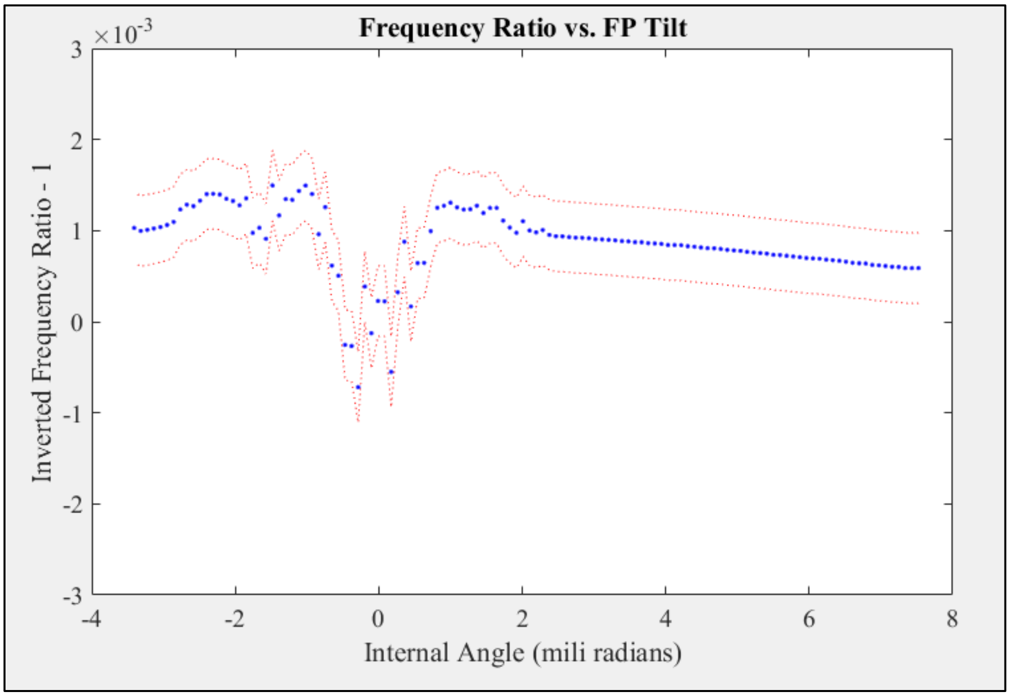

Figure 3.5.2: Overall average frequency ratio data with overall standard deviation from angle scans on March 8, 2016.

Due to the instability of the detection of the repetition rate around the zero angle statistical analysis for the angle scans had to be completed in the region from about 2 mrad to 8 mrad to accurately portray the statistical data. Figure 3.5.3 shows a close up of these angles from Figure 3.5.2.

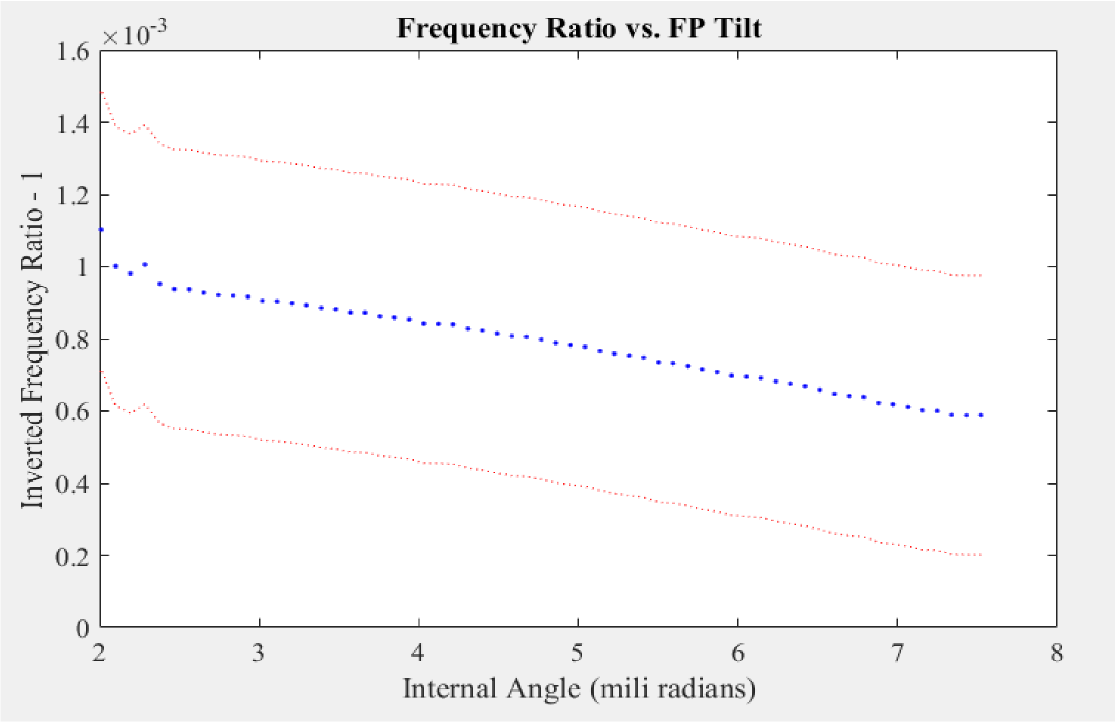

Figure 3.5.3: Close up of Figure 3.5.2 region of interest with statistical analysis boasting standard deviation of 3.869x10^{-4}*.*

Figure 3.5.4 shows the average ratio of each trial point by point, plus and minus the standard deviation of each respective trial from March 9, 2016. The four separate colors represent the average of each of the four separate trials demonstrating the variation in each of the trials, after which the sample was removed and placed back into the cavity to test placement stability. Figure 3.5.5 shows the overall average ratio for the four trials of four angle scans each on March 9, 2016, presented point by point in blue plus and minus the overall standard deviation with boundaries in red.

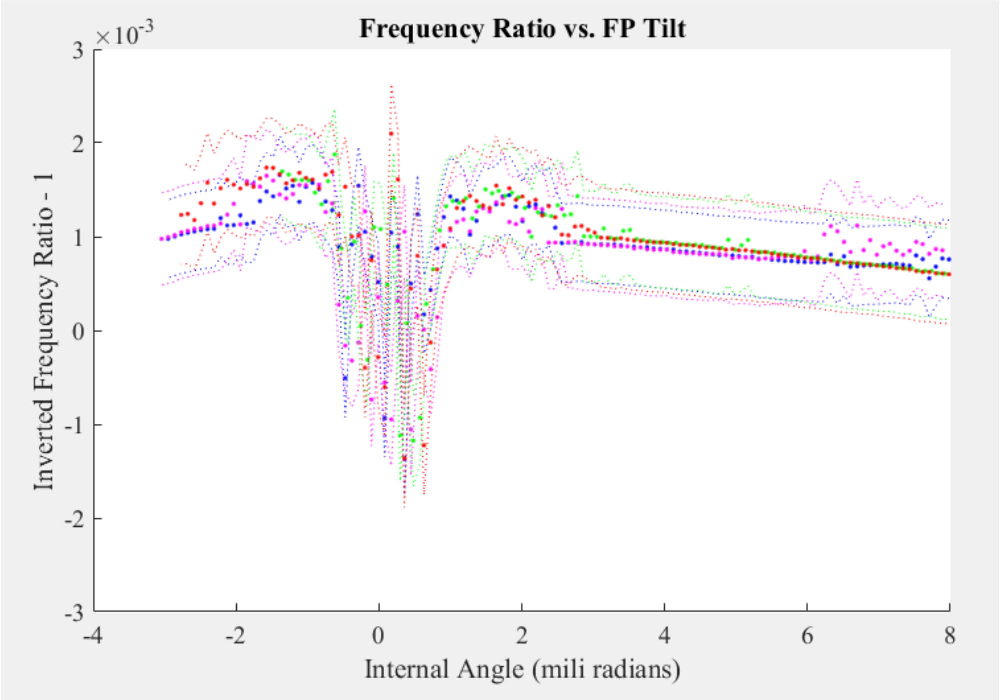

Figure 3.5.4: Frequency ratio data for each of four separate angle scan trial on March 9, 2016 each represented by a different color and associated dotted line representing the standard deviations of each point in the trial.

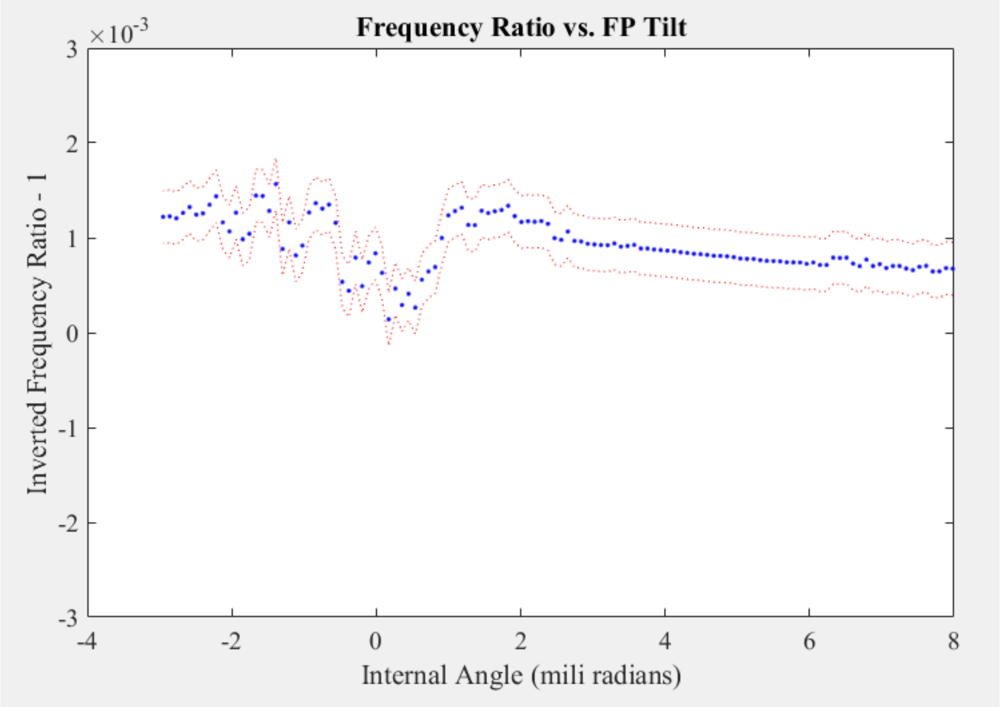

Figure 3.5.5: Overall average frequency ratio data with overall standard deviation from angle scans on March 9, 2016.

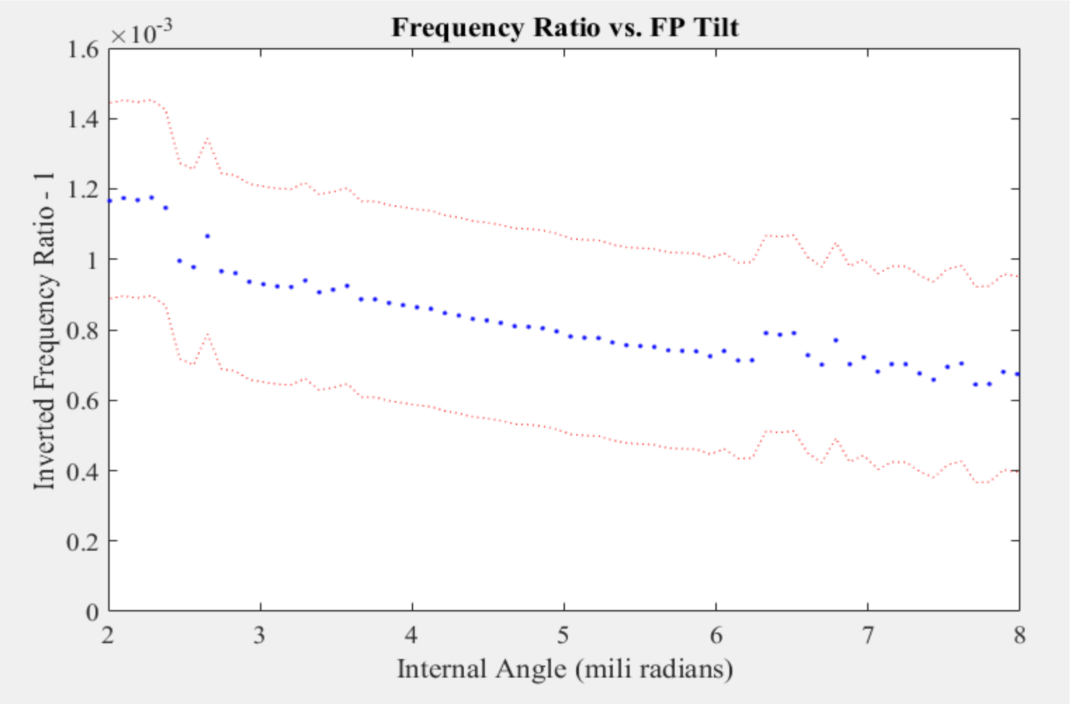

Figure 3.5.6: Close up of Figure 3.5.5 region of interest with statistical analysis boasting a standard deviation of 2.781x10^{-4}.

Again, because of the instability of the detection of the repetition rate around the zero angle statistical analysis for the angle scans had to be completed in the region from about 2 mrad to 8 mrad to accurately portray the statistical data. Figure 3.5.6 shows a close up of these angles from Figure 3.5.5. The experiment from March 8 produced data with a 3.869x10^{-4} standard deviation while the experiment from March 9 gave a 2.781x10^{-4} standard deviation.

On March 9, 10, and 11, 2016, cavity length scans were performed for a similar statistical analysis while keeping the FPE internal angle constant at 4 mrad. The results of this experiment are shown in Figure 3.5.7 to Figure 3.5.12. The overall cavity length was changed from +0.5 mm longer to -0.5 mm shorter than the cavity length at which the angle scans were performed. Figure 3.5.7 shows the results for 16 data runs averaged into 4 separate trials for data taken on March 9. Figure 3.5.8 shows the overall average and standard deviation of the data from the 4 trials shown in Figure 3.5.7. Figure 3.5.9 shows the results for 16 data runs averaged into 4 separate trials for data taken on March 10. Figure 3.5.10 shows the overall average and standard deviation of the data from the 4 trials shown in Figure 3.5.9. Figure 3.5.11 shows the results for 16 data runs averaged into 4 separate trials for data taken on March 11. Figure 3.5.12 shows the overall average and standard deviation of the data from the 4 trials shown in Figure 3.5.11.

Notably, in Figure 3.5.7 there was considerable instability in the measurements when the cavity length was changed in the positive direction above zero. The spikes in all of these plots represent a data dropout point in which either the frequency peaks representing the repetition frequency of the cavity or the repetition frequency of the FPE went to zero because of the signal drop out. Thus, the program selected the highest peak in the region leading to the instability. This instability can be corrected and was in the case of the measurements completed on March 10 and March 11, demonstrated by the significant lack of data variation. All of these plots for cavity length scans were plotted in the same axis range as the angle scans for comparison.

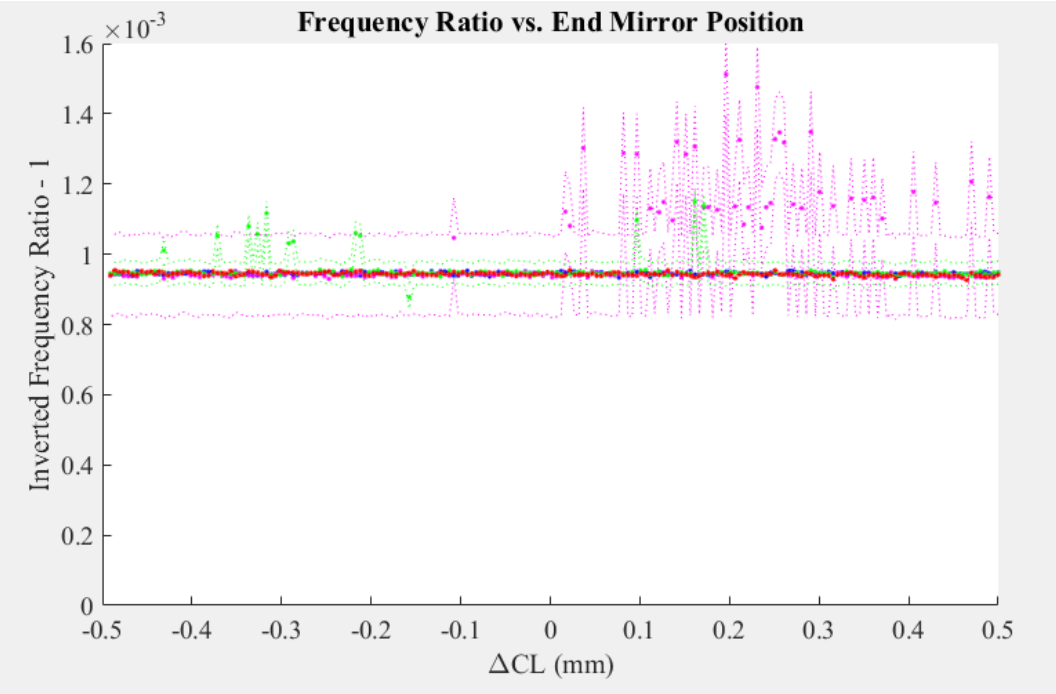

Figure 3.5.7: Frequency ratio data from four separate trials on March 9, 2016 with an overall cavity length change of 1 mm.

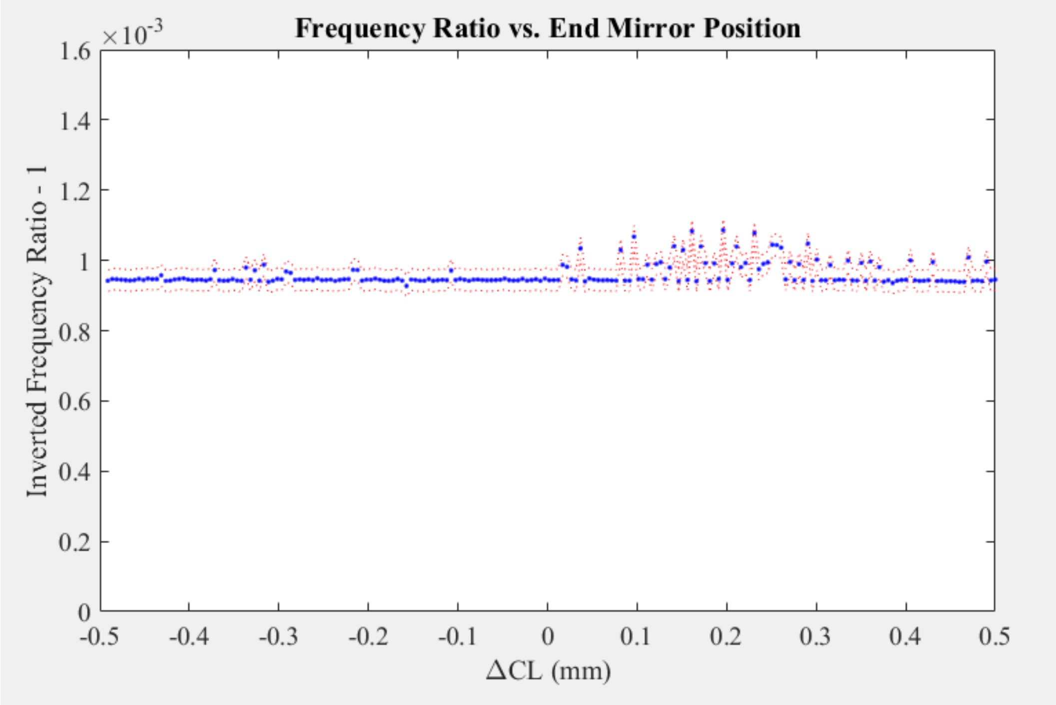

Figure 3.5.8: Overall average frequency ratio data (all four trials) with overall standard deviation from cavity length scans on March 9, 2016. Statistical analysis shows a standard deviation of 3.066x10^{-5}

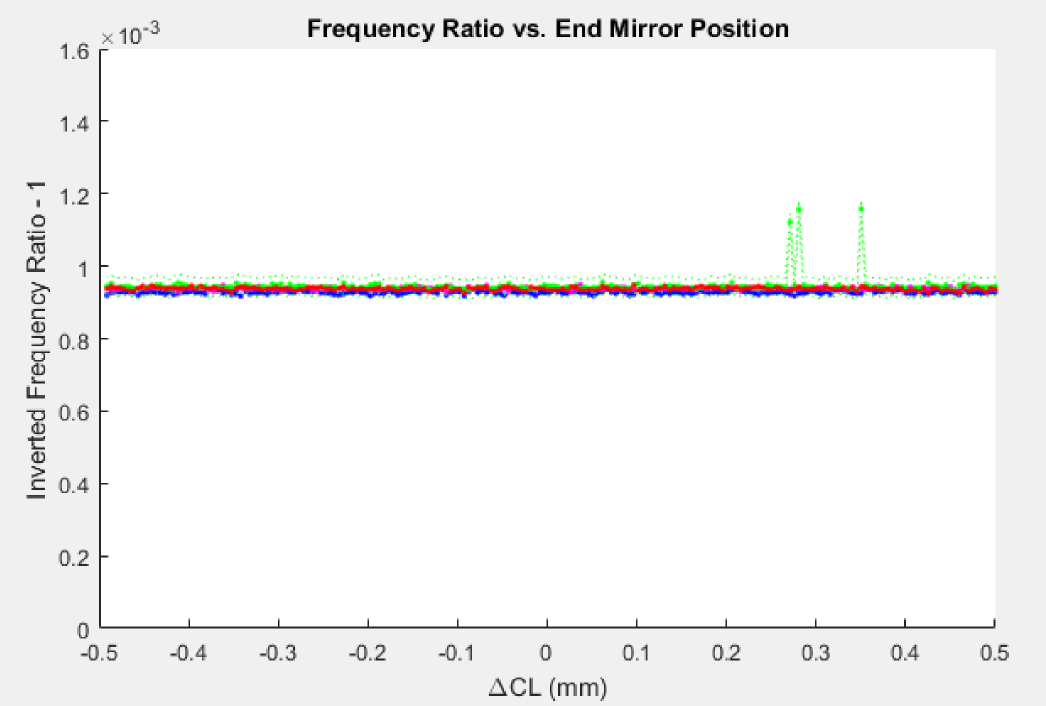

Figure 3.5.9: Frequency ratio data from four separate trials on March 10, 2016 with an overall cavity length change of 1 mm.

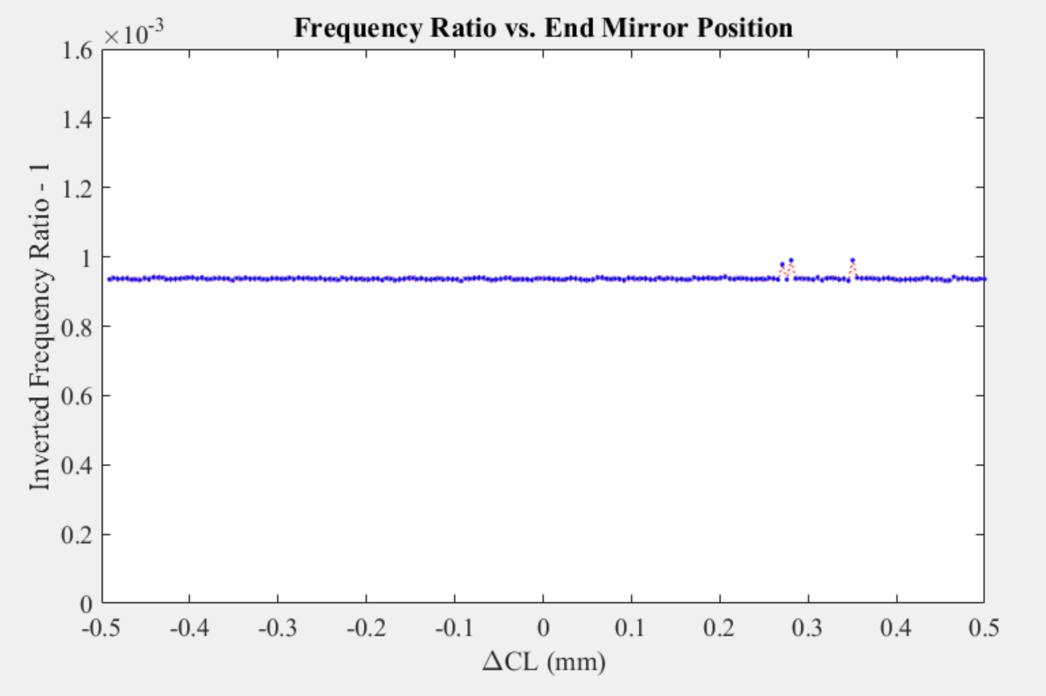

Figure 3.5.10: Overall average frequency ratio data (all four trials) with overall standard deviation from cavity length scans on March 10, 2016. Statistical analysis shows a standard deviation of $6.443x10^{-6}$

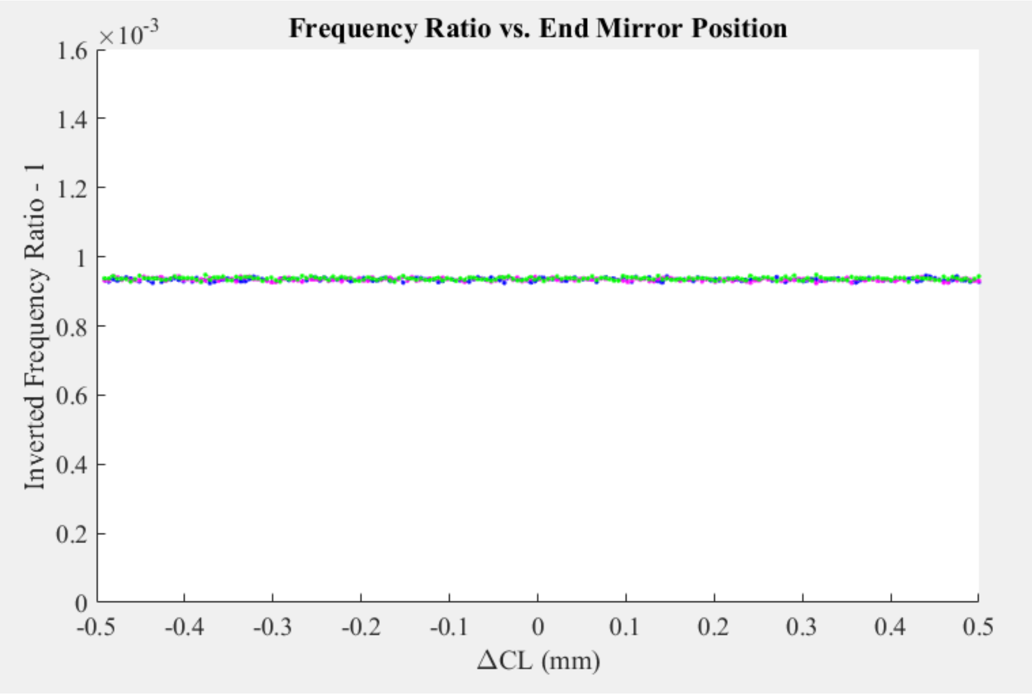

Figure 3.5.11: Frequency ratio data from four separate trials on March 11, 2016 with an overall cavity length change of 1 mm.

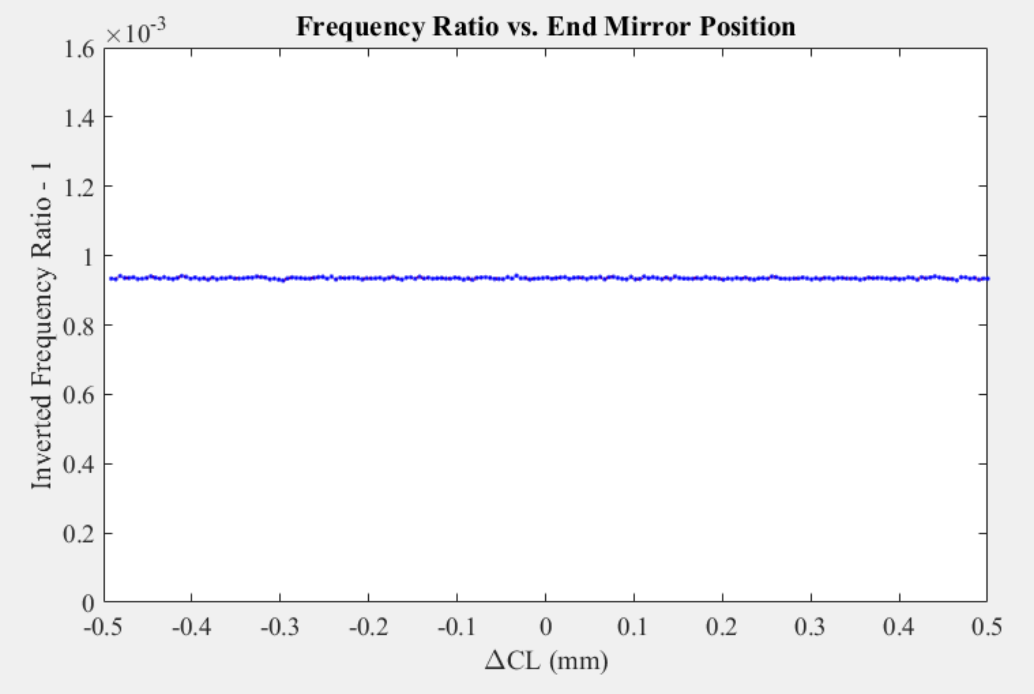

Figure 3.5.12: Overall average frequency ratio data (all four trials) with overall standard deviation from cavity length scans on March 11, 2016. Statistical analysis shows a standard deviation of 2.397x10^{-6}

The overall standard deviations for March 9, 10, and 11, 2016, were $3.066\text{x}10^{-5}$, $6.443\text{x}10^{-6}$, and $2.397\text{x}10^{-6}$, respectively. It is evident that the standard deviations are lower for length scans than for angle scans. The cavity length scans produce a more accurate result nearly two orders of magnitude better than the angle scan. Therefore, the cavity length scan is the primary method used to determine the change in refractive index.

Figure 3.5.7, Figure 3.5.8, Figure 3.5.9, and Figure 3.5.10 demonstrate the instability mentioned earlier corresponding to data drop outs primarily due to a difficulty in tracking the high frequency signal, also known as, the repetition rate of the FPE. This is a phenomenon that was corrected by adjusting the focusing mirrors in the cavity in order to shorten the pulses, thus enhancing the ability to mode-lock effectively. Overall, as a result, this phenomenon has been minimized and the frequency combs appear to be much more stable.

The primary take away from these experiments is that of the vast superiority of performing a cavity length scan instead of an angle scan. The stability in the measurements corresponding directly to the stability of the inverted frequency ratio and the original frequency ratio leads to a standard deviation in the results nearly 100 times smaller in the cavity length scans than for the angle scans.

3.5.2 Finding the Zero Angle

As mentioned in Section 3.3.6 being able to locate the zero angle of the FPE is essential to repeatability in any refractive index change experiment. By utilizing the method described in Section 3.3.6 it is possible to pinpoint with high accuracy the zero angle. This is completed by performing an angle scan from a large positive internal angle to a large negative internal angle, where the local minimum when plotting the intensity of the beam indicates the zero angle. This voltage minimum occurs because of deconstructive wave interference as the laser beam interacts with the FPE with normal angle reflections. This scan result is shown for control sample A15-1 in Figure 3.5.13.

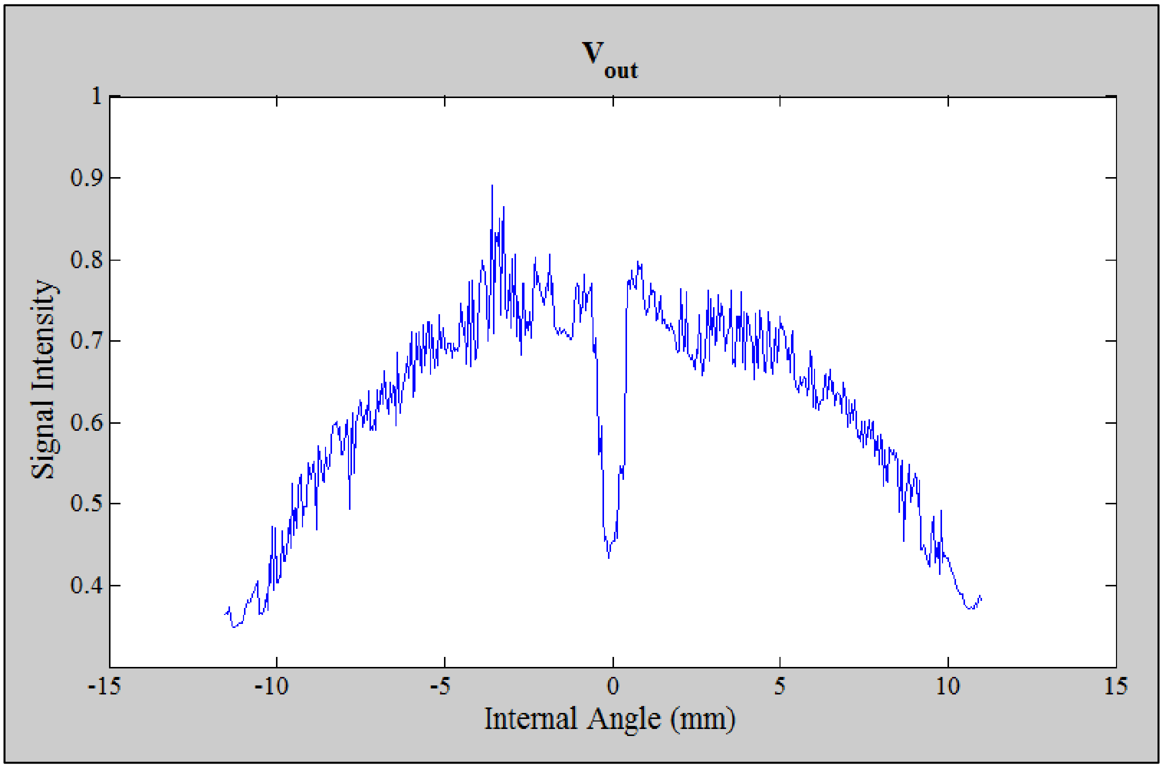

Figure 3.5.13: Demonstration of the determination of the zero angle as measured for sample A15-1. The local minimum in the center reveals the zero angle. The minimum point in theory is the exact zero angle.

After determining the zero angle a simple calculation is performed to find the micrometer position that corresponds to the desired FPE internal angle. In the case of refractive index change portion of this research the desired angle is 8 mrad while performing cavity length scans.

3.5.3 Crystal Rotation Experiment

During the initial rounds of this research it became apparent that there were some irregularities in the measurement of the repetition rate of the cavity, the repetition rate of the FPE, and their ratio. It seemed initially that the rotation of the sample within the mount may have a large effect on measurements. First, it seemed that the rotation affected greatly whether the envelopes of frequencies as seen in the frequency space representation of the system with the FPE (Figure 3.3.5) would appear at all. Second, the stability of laser mode locking was changed significantly as the sample was rotated within the mount. Lastly, the signal for each measurement was either stronger or weaker depending on the sample rotation. Given the incredible necessity for this laser cavity to be stable and repeatable within this research it was crucial to perform a short study to examine the full effects of the sample rotation upon the quantities in question.

The rotation was examined first by applying a motor to the rotational mount allowing for a consistent rotation of two rotations per minute (RPM) which corresponded to approximately three rotational degrees per second, requiring about 2 minutes to complete one full rotation. The resulting data was plotted and examined in Figure 3.5.14.

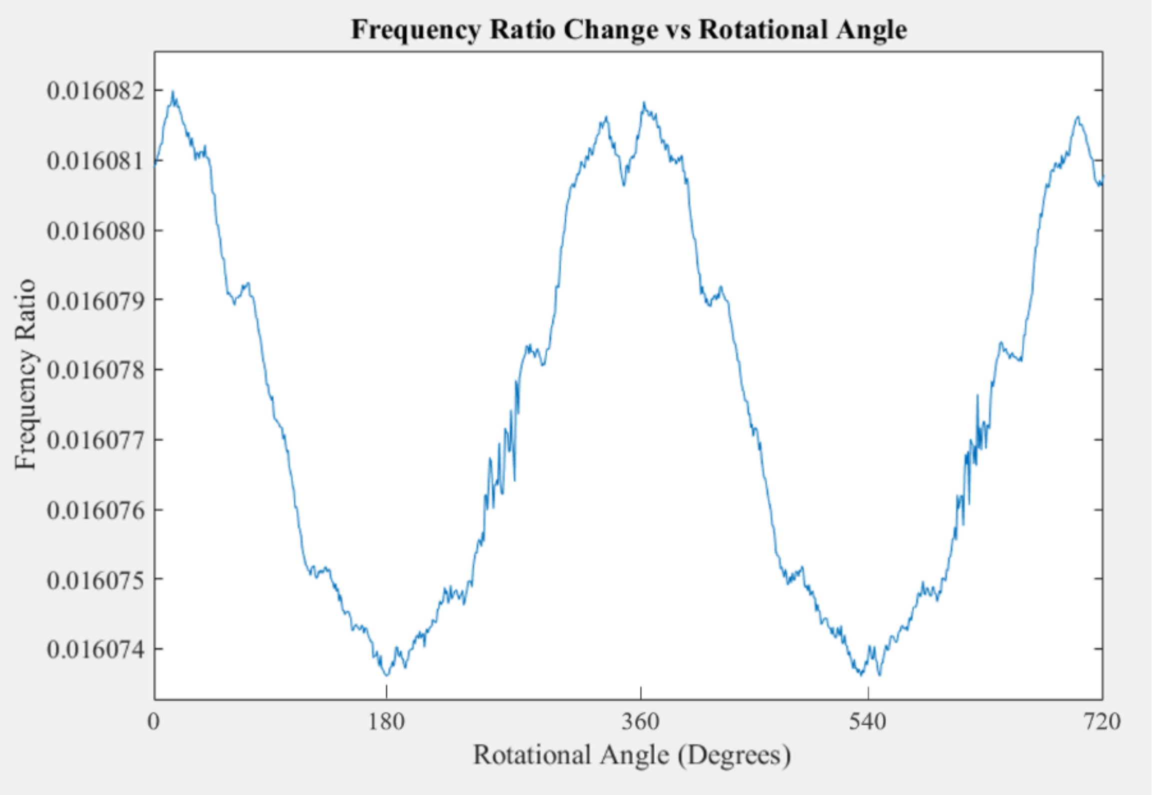

Figure 3.5.14: Plot depicting the LF/HF frequency ratio as a function of rotational angle when rotated with a 2 RPM motor.

This figure demonstrates the observed change in frequency ratio as the crystal sample was rotated. There is a strong periodic behavior overlaid with jagged noise. The non-uniformity of the data was due primarily to the coil connecting the motor to the rotation mount coupling in vibrations. The crystal structure and thus refractive index differences at different rotations - birefringence - were considered. Both amorphous SiO_2 and crystalline CaF_2 showed the same periodic behavior, so birefringence is not the explanation for the rotational periodicity. The next prevailing thought was that this was measuring the slight difference in thickness of the samples as a function of position, though the crystals were made with very parallel faces. In order to determine this, measurements had to be taken at a variety of rotational angles ensuring that the angles in every dimension (pitch, yaw, and roll) were the same between measurements (something that couldn't be accomplished utilizing the motor from the previous test). A representation of the mount utilized along with the assignment of the pitch, yaw, and roll directions is shown in Figure 3.5.15. The roll angle is also referred to as the rotation angle, and pitch angle as tilt angle.

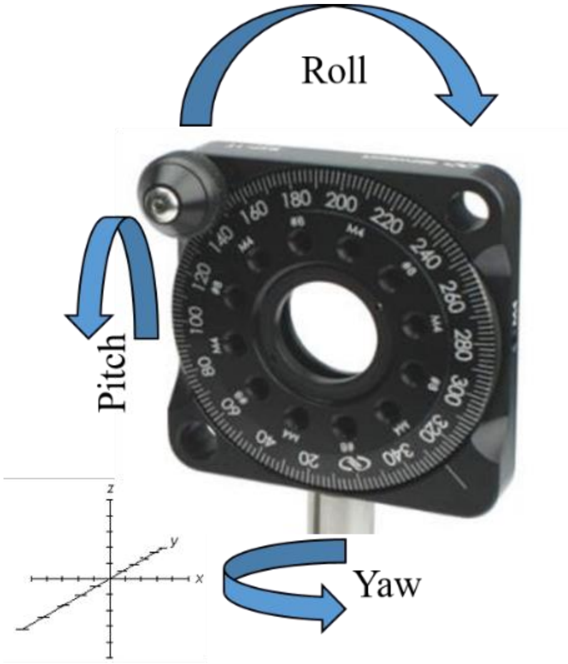

Figure 3.5.15: Depiction of the rotational mount with descriptions of the pitch, yaw, and roll directions used for these experiments.

Data was recorded every 20 degrees of rotation, ensuring that both the yaw and pitch of the sample remained constant. At each point all dimensions were corrected for each measurement to ensure the identical FPE angle was used. This data was generated and plotted to show the change in LF, HF, LF/HF ratio, and zero angle as a function of rotational degree. This data is shown in Figure 3.5.16 and Figure 3.5.17. The change in tilt to find the zero angle was also plotted for each rotational angle. The term delta utilized in Figure 3.5.16 and Figure 3.5.17 refers to this change in the tilt angle dialed in on the micrometer required to find the intensity dip of the zero angle.

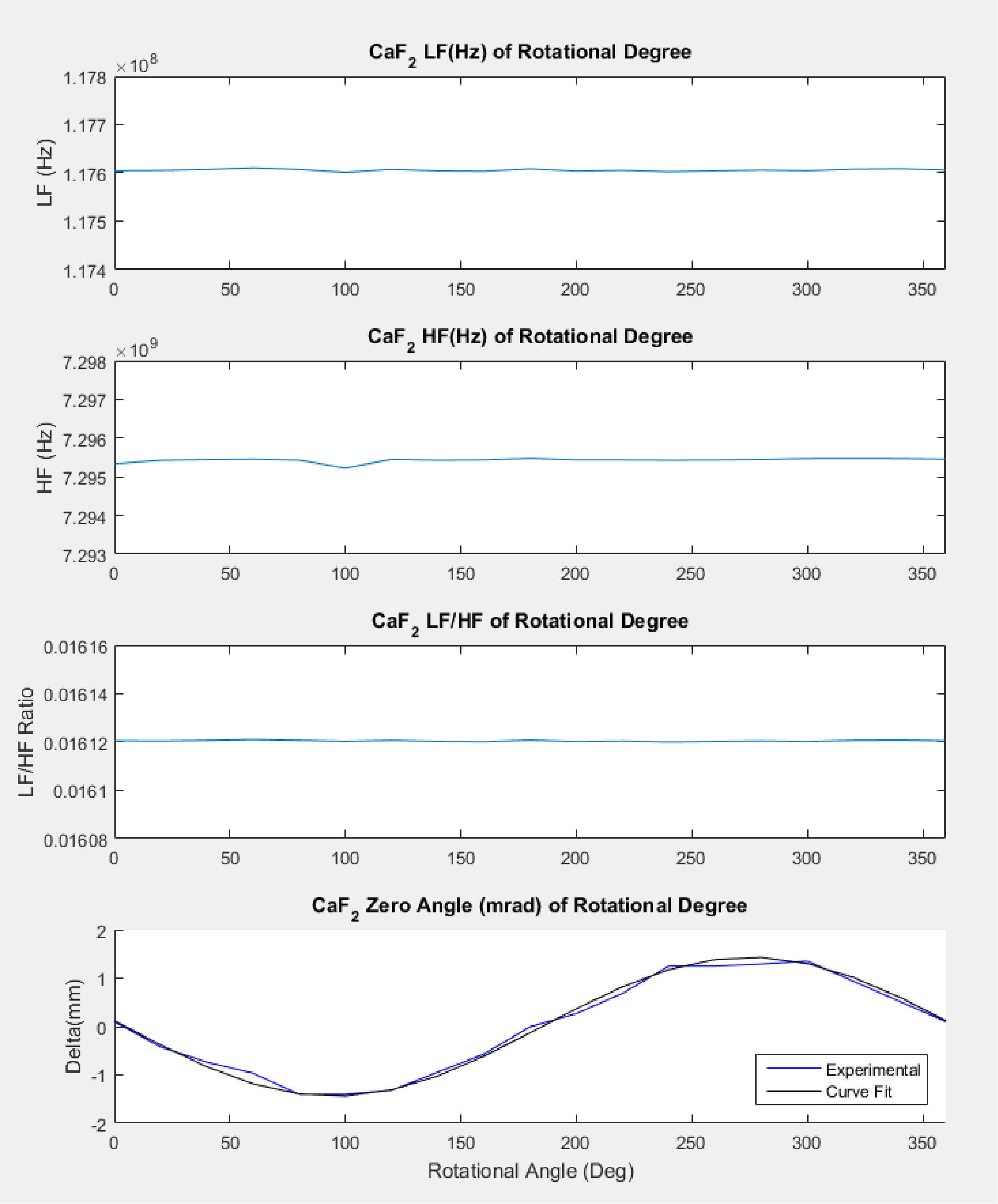

Figure 3.5.16: Plot demonstrating LF, HF, ratio, and zero angle data for the rotational experiment with CaF$_2$.

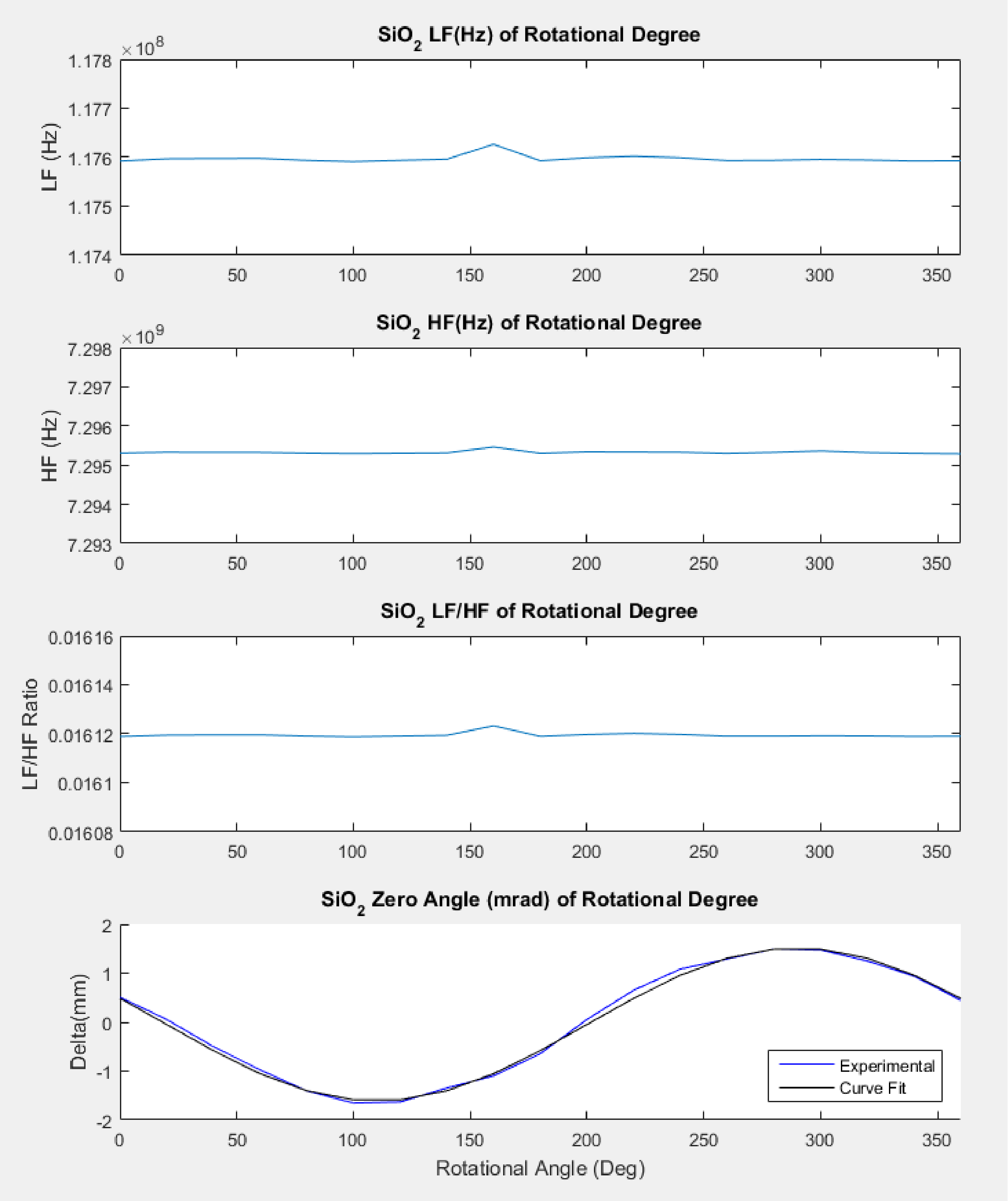

Figure 3.5.17: Plot demonstrating LF, HF, ratio, and zero angle data for the rotational experiment with SiO$_2$.

What was evident in this data was that while rotation greatly affected the position of the zero angle, after correcting for the delta when setting the sample to the desired angle (4 mrad pitch), there was a remarkable stability despite the rotation of the sample. Additionally, when inserting the sample purposefully incorrect, the change in zero angle witnessed was much more dramatic. In summary, it appears the observed effects did not have to do with the parallel faces of the sample or the crystalline structure.

One final experiment was planned to monitor the zero angle change due to rotation, however, this time the placement of the sample in the mount would be intentionally altered. The thought at this point was that what was being seen was in fact due to the extreme unlikelihood of placing the sample perfectly into the mount. The set screw that holds the sample in place does not press down on the center of the cylindrical sample and thus, depending on tightness, would cause some initial change in set position which would most likely cause the sinusoidal change in zero angle being witnessed. The Figure 3.5.18 below illustrates the set screw issue as described with an exaggerated tilt (pitch) angle.

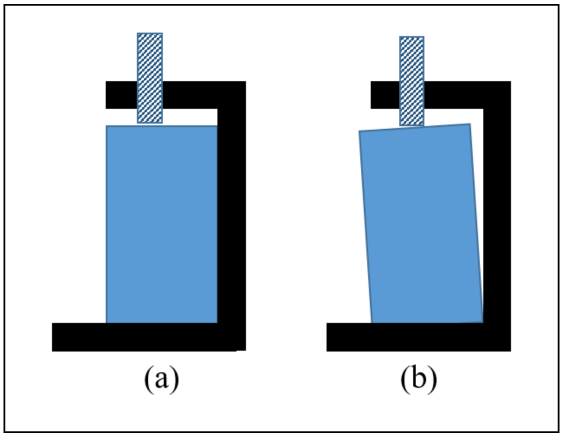

Figure 3.5.18: Simple depiction of the FPE mount, (a) demonstrates the perfect placement of an FPE, (b) demonstrates the potential effect of tightening the set screw that can change the zero angle. The crystal is oriented in this figure so the laser path is left and right.

Notice, that only the pitch angle has changed slightly when tightening the screw, however, when rotated this would cause also a change in the yaw angle which, if left uncorrected, would certainly produce a data set that is unusable. This hypothesis was confirmed and is realized in Figure 3.5.19. The tilt (pitch) of the crystal is controlled by a micrometer, and the necessary micrometer value to find the zero angle is presented as a function of crystal rotation angle.

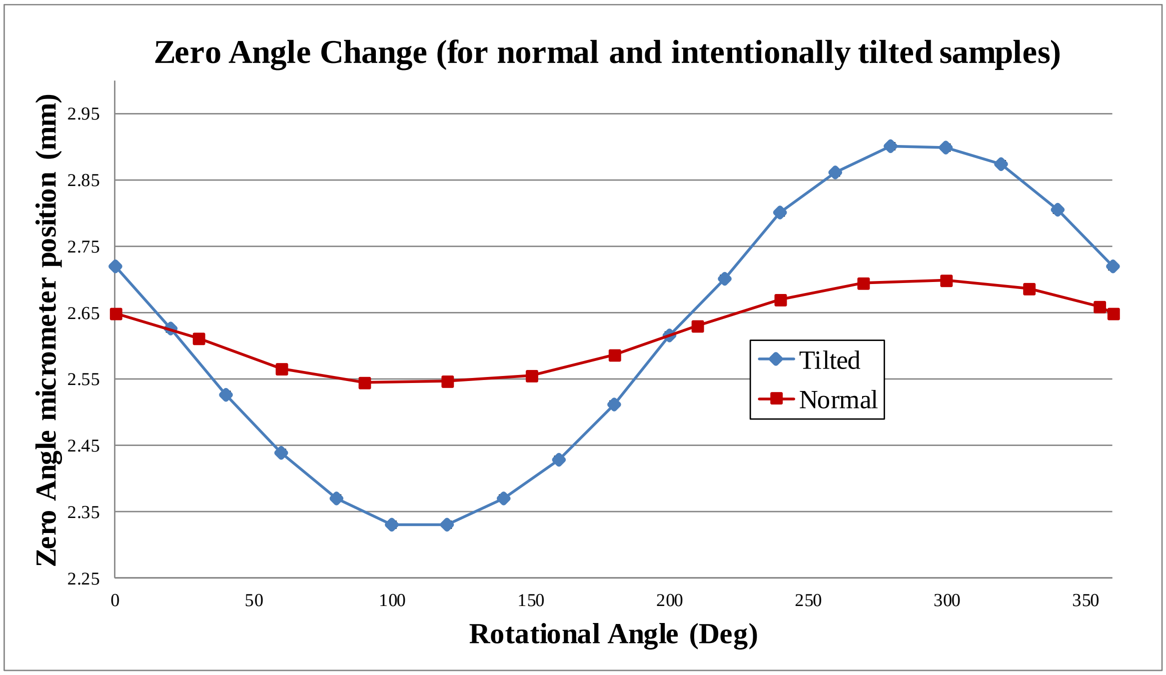

Figure 3.5.19: Plot depicting the tilt setting to find the zero angle as a function of rotation for a sample placed normally and the same sample placed intentionally at a dramatic tilt.

It is clearly seen here that the effect of intentionally inserting the FPE incorrectly (at an angle) into the cavity is an increase the variation that the zero angle changes due to rotation.

It has been shown that when the pitch, yaw, and roll angles are held at a relative constant the repetition rate of the cavity and the FPE are remarkably stable even as the rotation is changed. This relaxes the requirement of always placing the sample at the same rotational angle for each scan while ensuring that the data produced will be usable and reliable. Additionally, this effect can be used in future research to determine how well an FPE has been placed into a cavity, a method that could be useful in many laser physics applications.

3.6 Control Samples and Daily Variation

While, the data from these repeatability and characterization experiments suggests very stable and precise data, it became apparent that over a period of weeks there seemed to be some drift back and forth in the data. Specifically, the frequency ratio would fluctuate to a greater degree than observed in the repeatability analysis. This is shown for the two control samples, A15-1 and A15-2, over a period of measurements spanning two weeks.

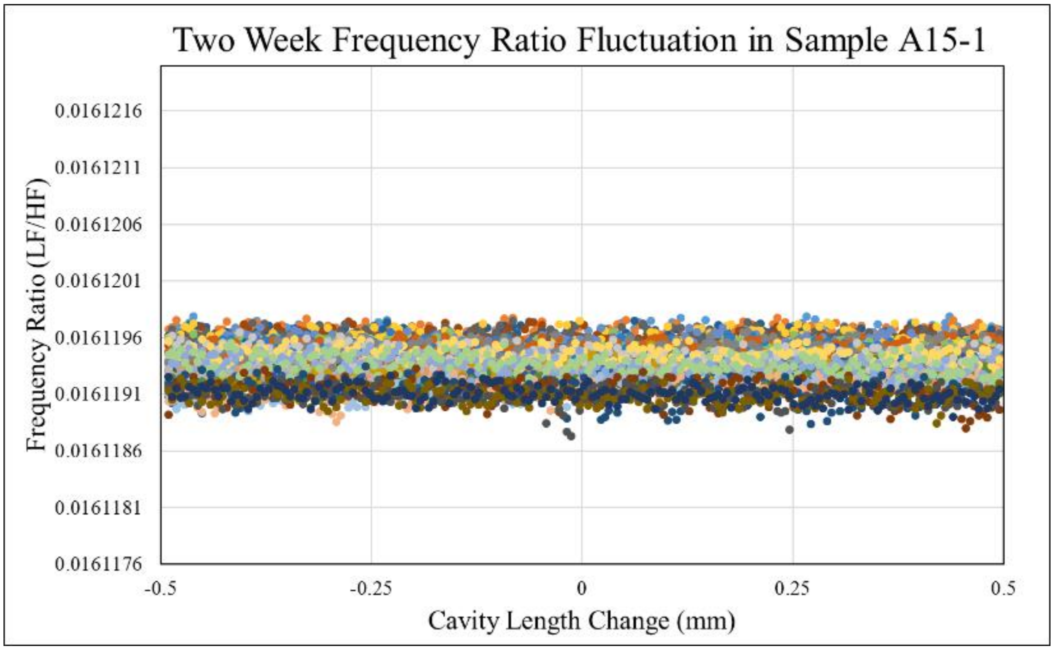

Figure 3.6.1: Demonstration of the change in the frequency ratio for sample A15-1 over a period of two weeks. The standard deviaiton of the entire population was 1.37x10^{-6}

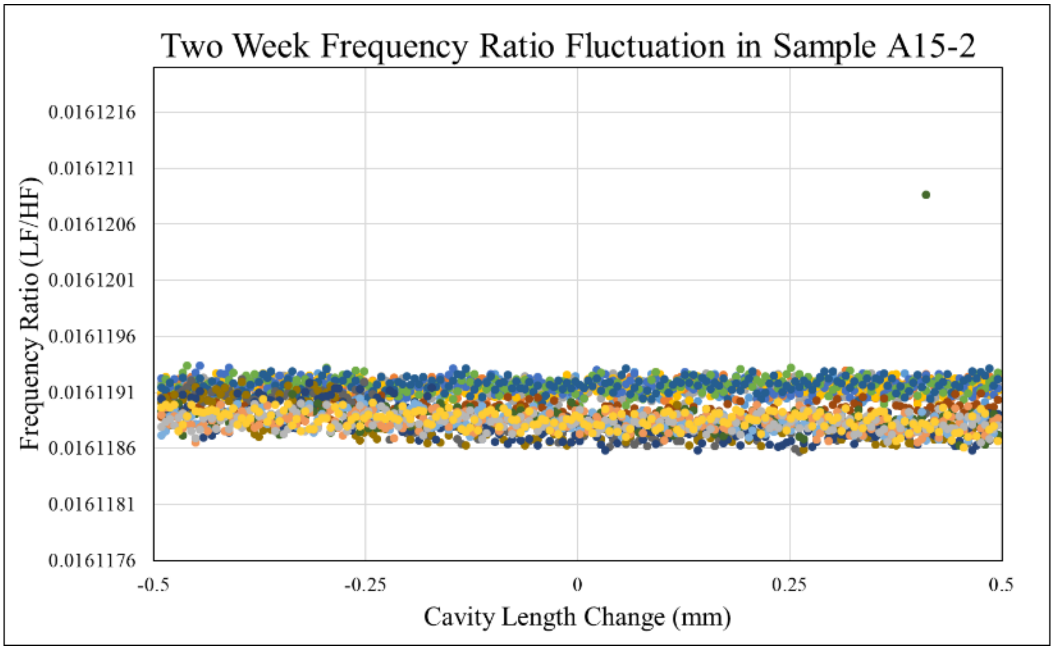

Figure 3.6.2: Demonstration of the change in the frequency ratio for sample A15-2 over a period of two weeks. The standard deviaiton of the entire population was 1.536x10^{-6}

This data demonstrates the daily variation as measured in the two control samples and contrary to the stability in the single day repeatability experiments it seems that over a longer period of time the data drifts back and forth. After close examination, it was determined when considering the laboratory environment that one of the factors in this change is a correlation between the frequency ratio and the humidity and pressure within the lab. A closer examination of this is provided in Section 5.2 and an analysis of the data trends with the laboratory environment is provided in Appendix B. A correction was generated utilizing control samples and this was done for all the data produced in the latter portion of this work. The measured LF/HF ratio of a test sample can be compared with the LF/HF ratio of control samples to correct for environmental changes. By tracking the daily change in the control samples a simple arithmetic correction is applied to the irradiated sample data to extract the measured refractive index change. This correction was completed by measuring the control samples and the irradiated samples on the same day with similar laboratory environments. By doing this both before and after a sample was irradiated, the baseline measured for the irradiated sample could be adjusted based on the daily variation in the control samples in order to update the irradiated baseline to a value that is representative of what it would have been, had it been measured on the same day with the same laboratory environment as the post-irradiation measurement.

3.7 Calibration and Repeatability Conclusions

There were several things to take away from these repeatability analysis experiments. The first is the vast superiority of performing a cavity length scan instead of an angle scan. The measurement stability of the cavity length scan leads to a standard deviation nearly 100 times better than that of the angle scans. These values also take into account the repeatability of placement since between each trial the sample was removed and placed back into the mount by hand. In addition, the ability to largely ignore crystal rotation when removing and inserting the FPE into the cavity, provided that the other angles remain consistent, is very useful. The only repeatability issue that remains is that over a period of days the frequency ratio as measured tends to drift, even with no intentional system changes. This can be due to any number of factors in the laser cavity including the laboratory environment and the functioning of the laser itself. One of the largest battles to be fought daily is dust. Dust accumulating on the mirrors, lenses, and prisms in the cavity has a dramatic effect on not only the data stability but also the overall ability to mode-lock the laser. However, as mentioned, this daily variation is corrected for by measuring control samples along with the irradiated sample in order to adjust the baseline measurement for their radiated sample enabling the necessary comparison for refractive index change.

Chapter 4: Irradiation Methodology

4.1 Crystal Irradiation Methodology

The next stage of this research included the irradiation of physical CaF_2 crystal samples. This was accomplished utilizing three experimental apparatuses. The first utilized a Nuclear Chicago (NH-3) Neutron Howitzer containing a 6 Curie (Ci) PuBe neutron source. The second used the 350-keV Cockroft-Walton accelerator at Sandia National Laboratory's Ion Beam facility, which was calibrated to produce a D-D (Deuterium-Deuterium) and D-T (Deuterium-Tritium) fusion neutron yield. The third and final set of experiments was performed using the Oregon State University TRIGA reactor.

The primary purpose of these irradiation experiments was intended to demonstrate measurements of neutron induced refractive index change and a beginning calibration to allow for assessment of unknown neutron fields in the future using these refractive index measurement techniques. This will ultimately allow for the ground work in applying this work towards its goal of high precision dosimetry. Each sample's thickness and diameter was measured mechanically with a micrometer having the accuracy of 1/10 of 1/1000 of an inch. The latter translates to an accuracy of about 2.54 microns. This allowed for a moderate check of the length change and thus the density change of the material being irradiated. Table 4.1.1 shows the original measurement results for samples numbering A15-1 to A15-10. However, only samples A15-3 through A15-6 were irradiated.

Table 4.1.1: Table showing the physical measurements of the first set of CaF_2 samples.

	CaF_2 Pre-Irradiation (03/28/2016)		
	d (mm)	t (mm)	volume (cc)
A15-1	25.273	15.189	7.620
A15-2	25.298	15.187	7.634
A15-3	25.306	15.189	7.640
A15-4	25.273	15.187	7.619
A15-5	25.284	15.187	7.625
A15-6	25.273	15.184	7.617
A15-7	25.281	15.184	7.622

Table 4.1.2 shows the dimensions of samples B15-1 through B15-5 as measured on January 24, 2017. Samples B15-1 and B15-2 were used as controls for the OSU irradiation experiment while B15-3 through B15-5 were irradiated by OSU.

Table 4.1.2: Table showing the physical measurements of the second set of CaF_2 samples.

	CaF_2 Pre-Irradiation (01/24/2017)		
	d (mm)	t (mm)	volume (cc)
B15-1	19.981	14.975	4.696
B15-2	19.975	14.970	4.691
B15-3	19.975	14.970	4.691
B15-4	19.972	14.972	4.690
B15-5	19.980	14.971	4.694

4.1.1 NH-3 Neutron Howitzer Irradiation

The first irradiation apparatus was the NH-3 neutron howitzer. Within this apparatus three experiments were completed with the intention to serve as a basic proof-of-principle in an extremely low neutron flux environment that was easily accessible at UNM. These three experiments included a 24 hour one time irradiation, a sequential irradiation from zero to 221 days, and one final sequential irradiation from zero to 6.5 days. Several factors that must be kept in mind during this research is not only the cumulative radiation absorbed in a sample but also the average energy of the neutrons interacting with the material and the flux of the neutrons (i.e., what is the rate at which neutrons are interacting with the material). The average energy of the neutrons generated from the PuBe source in the howitzer is about 5 MeV but they have a broad spectrum. An evaluation of the possible neutron spectrum from the PuBe source is presented in Section 4.2.1. A representative image of a commercial NH-3 Neutron Howitzer is included as Figure 4.1.1. The sample to be irradiated is placed inside one of the two ports depicted half way down the circumference of the cylindrical housing.

Figure 4.1.1: Photo of the NH-3 Neutron Howitzer by Nuclear Chicago

4.1.2 Sandia National Labs Irradiation

The second irradiation apparatus utilized a facility at Sandia National Laboratory to generate to yield Deuterium-Deuterium (DD) and Deuterium-Tritium (DT) fusion neutrons. The experiment was completed in two stages. The first was a campaign of irradiations that yielded in an absorbed dose of 3.15 Gy after which refractive index measurements were performed. The second stage was an additional irradiation of the same CaF_2 sample adding an absorbed dose of 1.56 Gy which brought the total absorbed dose in the sample to 4.71 Gy. This experiment was intended to provide another proof-of-principle test to determine the long-term damage of the CaF_2 sample exposed to a higher neutron flux environment at two different neutron energies. The neutrons generated in this irradiation experiment were generated with the 350-keV Crockroft-Walton accelerator at Sandia National Laboratory's Ion Beam facility by accelerating deuterium ions into either an ErD_2 or ErT_2 targets to yield D-D and D-T fusion neutrons, respectively [57]. For this work, the sample was located at 0 degrees relative to the beam which yielded mono-energetic neutrons having energies of 2.91 MeV and 14.79 MeV for the D-D and D-T reactions, respectively. The fluence for the CaF_2 sample was determined by Sandia National Laboratory utilizing the Associated Particle Method [58]. The sample experimental schematic of the setup utilized to generate D-T neutrons is shown in Figure 4.1.2.

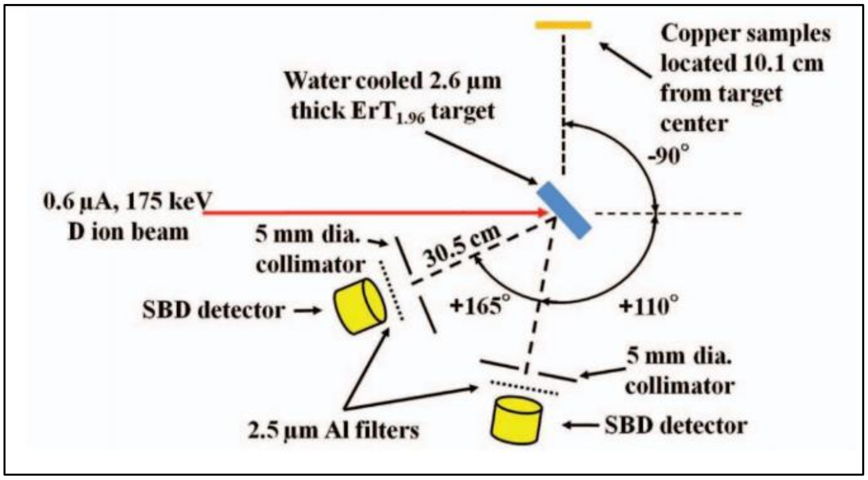

Figure 4.1.2: Example schematic of experimental setup for generating D-T neutrons at Sandia National Laboratory

4.1.3 Oregon State University Irradiation

The third irradiation apparatus utilized the outer ring of OSU's TRIGA reactor. It was primarily intended to produce an much greater fluence of incident neutrons on the CaF_2 samples than was able to be performed by the NH-3 Howitzer or the Sandia apparatus. These three samples were subjected to a fast and near-fast neutron (100 keV – 10 MeV) flux of $2.51\text{x}10^{13} \pm 4.75\text{x}10^{12}$ n/cm^{2}s, sufficient to cause numerous, high energy PKAs in CaF_2. Three samples were irradiated at varied lengths of time in order to achieve a neutron fluence of $1.70\text{x}10^{16}$, $1.70\text{x}10^{17}$, and $1.70\text{x}10^{18}$ neutrons/cm^2 for samples B15-4, B15-5, and B15-3, respectively.

4.2 Estimating Radiation Fluence, Energy Fluence, and Dose with MCNP

In order for accurate data tracking and ultimately correlation with refractive index change an accurate estimation of fluence, energy fluence and absorbed dose must be determined. For the first irradiation experiment, using the NH-3 neutron Howitzer, the fluence, energy fluence, and dose was calculated using an MCNP code designed to model the neutron Howitzer. Utilizing an f4 tally the flux in the sample will be calculated and using an f6 tally the rate of energy deposited in the sample the dose rate can be estimated. This option in MCNP generates a value of rate of energy deposited with the units of $MeV/(g * s)$. This leaves only a simple conversion to get the value into a desirable form. Due to the complications of modeling the Sandia National Labs irradiation setup the fluence was determined by staff performing the experiments. However, given the fairly monoenergetic nature of the D-D and D-T neutrons delivered, the calculation of energy fluence and dose is a simple conversion using MCNP output. Similarly, energy fluence and dose data for the OSU irradiation experiments was obtained in the same fashion using MCNP as a guide.

4.2.1 NH-3 Neutron Howitzer MCNP Modeling

The first step is to estimate the dose received in the irradiated CaF_2 in the NH-3. A full model of the NH3 Neutron Howitzer, developed by Steve Su, was modified to incorporate a CaF_2 and the neutron flux profile and dose rate profile were determined using an F6 tally in MCNP. A crucial piece of this puzzle is the definition of the source spectrum. The source in the NH-3 Neutron Howizer is a Plutonium-Beryllium (PuBe) source, with neutrons from the Be(a,n) reaction and directly from Pu fission. Source spectra has been derived for various PuBe sources with varying Pu content [59]. For this research the Pu content in the PuBe source was assumed to be 83%. It is worth noting that the difference in the source spectrum for 77%, 83% and 95% are minimal as shown in Figure 4.2.1. The average neutron energy from the 83% Pu content PuBe source was calculated to be approximately 5.09 MeV.

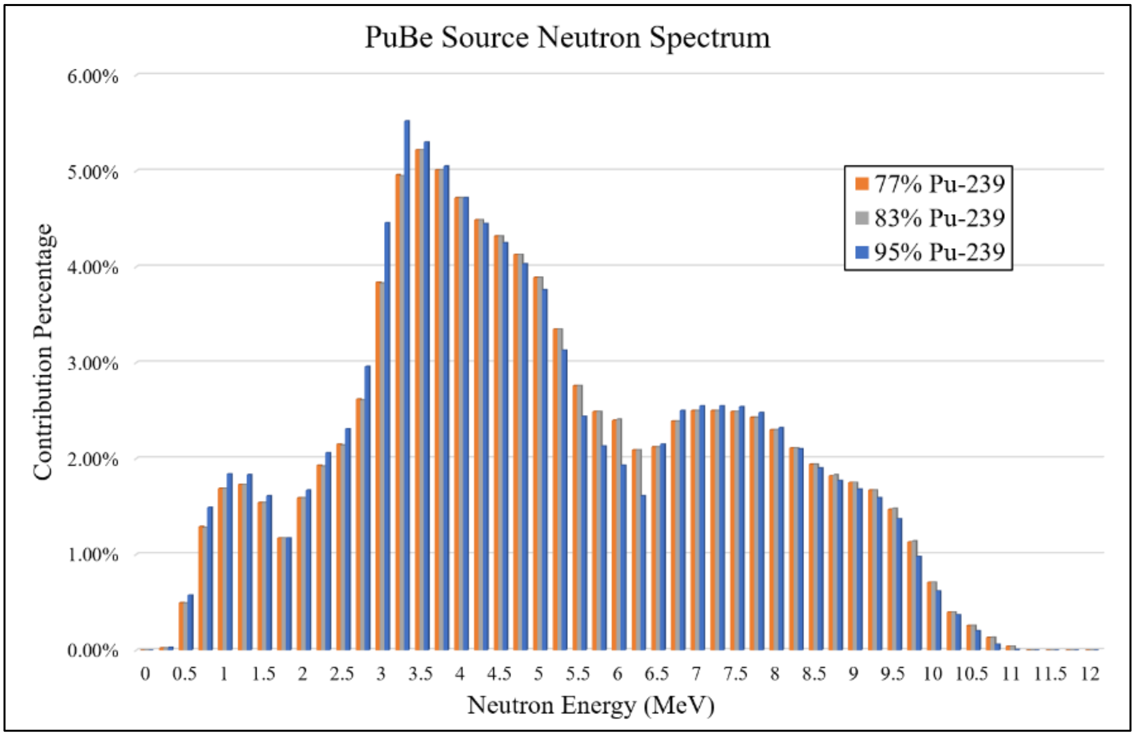

Figure 4.2.1: Source Spectrum for in a PuBe source with varying Pu content [59].

The MCNP code was modified to use the spectrum shown in Figure 4.2.1 to represent the NH-3 system, to more accurately estimate the flux and the dose in a CaF_2 sample. The geometry of the NH-3 Neutron Howitzer built within MCNP is shown in Figure 4.2.2 observing the XY plane and in Figure 4.2.3 observing the XZ plan. The number designations in the figures correspond to layers as follows:

1. Paraffin
2. Aluminium
3. Air
4. PuBe source

5. Aluminum

6. Air

7. Aluminum

8. Lucite

9. Calcium Fluoride (CaF_2)

10. Air

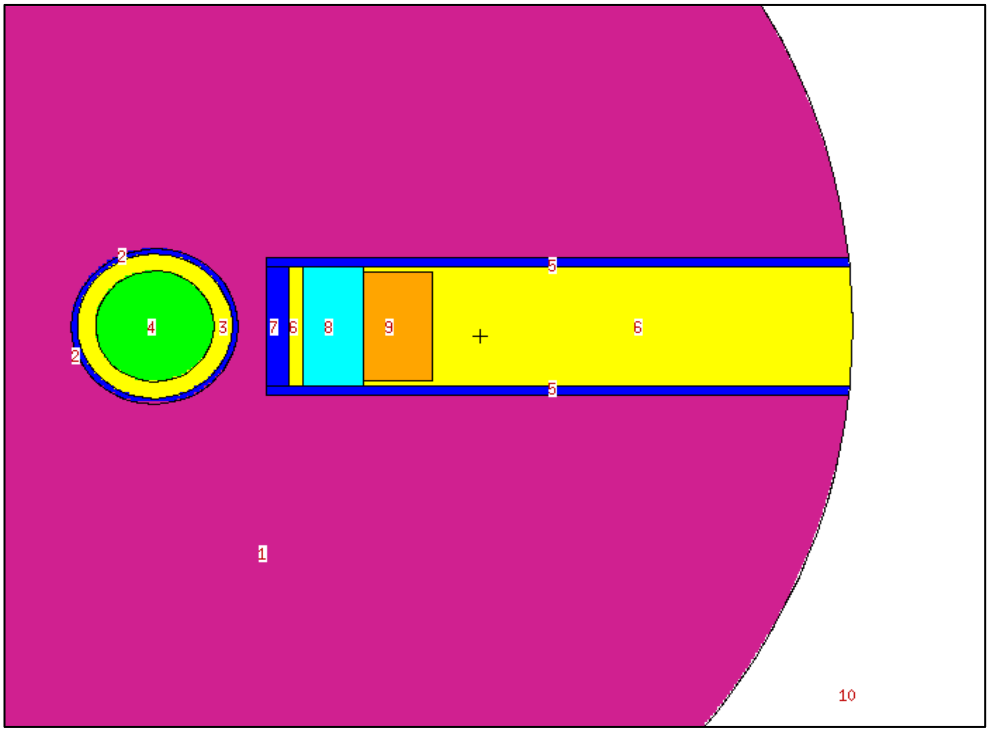

Figure 4.2.2: XY-plane view of the MCNP geometries for the NH-3 Neutron Howizer with 15 mm CaF_2 sample inserted (as region 9).

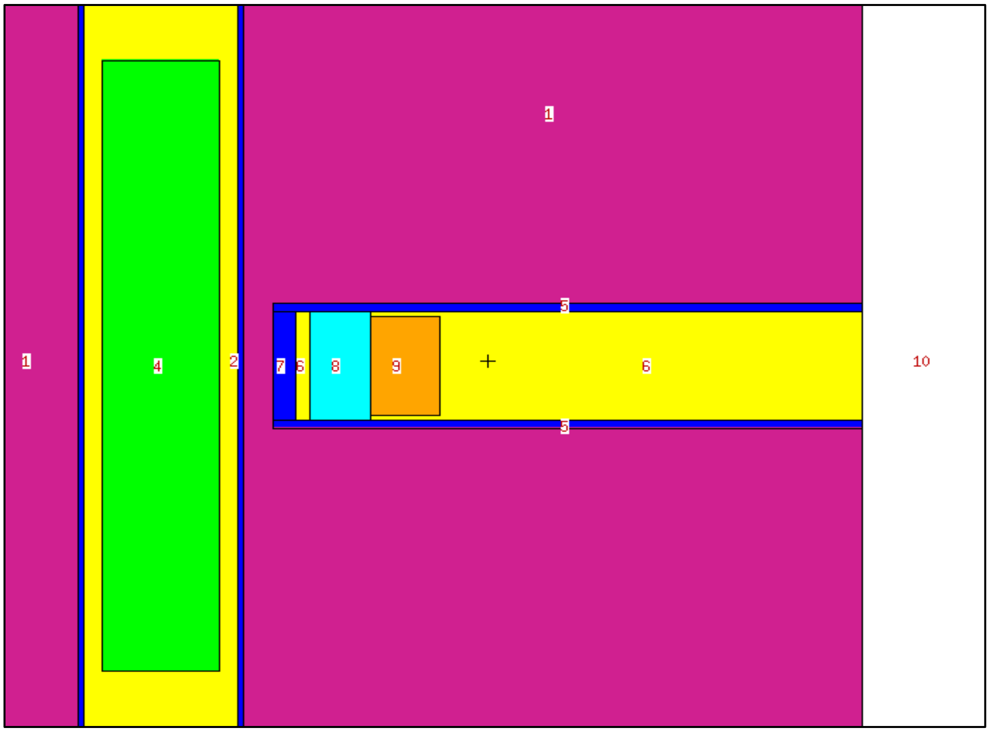

Figure 4.2.3: XZ-plane view of the MCNP geometries for the NH-3 Neutron Howizer with 15 mm CaF_2 sample inserted (as region 9).

Using an F4 and F6 tally the average neutron flux and energy deposition can be calculated inside a specified region. Setting that region to surface 9 as shown in Figure 4.2.2 and Figure 4.2.3 allows for the calculation inside the CaF_2 sample. MCNP uses energy bins to calculate flux and energy distribution. The flux per energy bin for the 6.5 mm and 15 mm thick CaF_2 samples is shown in Figure 4.2.4. Both thicknesses were considered for measurements, though only 15 mm samples were eventually used. This figure shows the distribution by energy of the flux in the CaF_2. By adding the energy bins together one can get a value for the total flux. Because MCNP normalizes the flux and energy distribution to a single neutron. In order to get the actual flux, the output from MCNP must be multiplied by the source strength. The source strength due to lack of documentation on the utilized source was determined by published data for PuBe sources and is given to be approximately 1.2×10^7 n/s [60]. This gives the results for flux in the CaF_2, presented per energy bin in Figure 4.2.4.

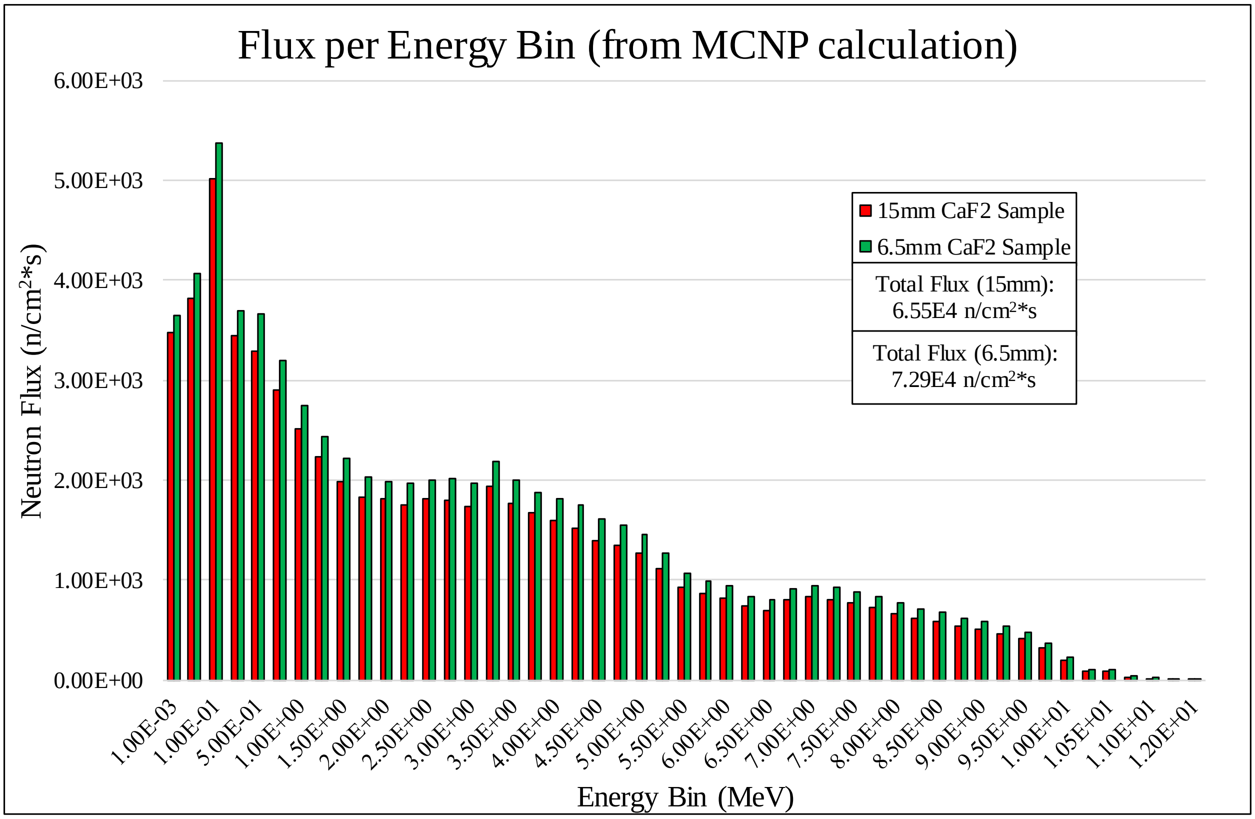

Figure 4.2.4: MCNP calculated flux distribution in CaF_2 samples.

From these flux quantities, the energy flux can be calculated using Equation 28.

$$\psi = \varphi E_{bin} \qquad \text{(Eq. 28)}$$

where ψ is the energy flux and φ is the neutron flux. Using an F4 and F6 tally the average neutron flux and energy deposition can be calculated inside a sample further leading to the dose estimation. Figure 4.3.6 shows the energy flux as a function of Energy. Again, creating a sum of all of the energy bins will give a value for total Energy Flux.

From this quantity, a simple calculation of dose can be obtained using the neutron kerma factor and making the assumption that the chamber is in charged particle equilibrium [61]. Due to the largely homogenous interaction of the neutrons within the crystal and the minimal range of the PKAs (i.e., charged particles) this approximation is acceptable. The only place this would not be a solid approximation is at the surface of the crystal were some atoms are not moving or may leave the crystal if they are struck by highly energetic neutron. The dose, D, can be determined from the kerma factor, K, which is

$$D = K = \Phi F_n \qquad \text{(Eq. 29)}$$

for a monoenergetic neutron fluence with the neutron kerma factor, F_n, for that energy. The kerma depends on the energy transferred to charged particles, and dose depends on energy absorbed, but these are close and the two quantities are treated as such. The neutron kerma factor F_n can be obtained from literature for a variety of materials and neutron energies [62]. For the 15 mm thick CaF_2 crystal sample, assuming an average neutron energy of 5 MeV and using the previously determined flux spectrum in Figure 4.2.4, the total energy flux is 1.88 x10^5 MeV·n/cm^2·s. The neutron kerma factor for 5 MeV neutrons is 6.62x10^{-10} rad·cm^2 [62]. Using this value and the energy flux, a dose rate of 3.86x10^{-5} rad/s or 3.86x10^{-7} Gy/s. Thus, the total dose over a 24 hr period would be 0.0159 Gy for the 15 mm thick sample. Due the slightly higher flux in the 6.5 mm sample the estimated dose rate is also slightly higher and comes out to 0.0208 Gy. These accuracy of these calculations is increased by discretizing the flux into bins that fit a defined kerma factor.

At this point, these calculations can be compared side by side with discretized calculations of dose utilizing the flux-to-dose conversion factors, which is a commonly utilized way of estimating dose, quoted by NCRP-38 and ANSI/ANS-6.1.1-1977. These flux-to-dose conversion factors and associated Q-values are shown in Table 4.2.1.

Table 4.2.1: Values of Dose Factor and Quality Factor for converting flux-to-dose per NCRP-38 and ANSI/ANS-6.1.1-1977.

Energy (MeV)	Dose Factor (rem/hr)/(n/cm^2·s)	Quality Factor
0.001	3.76 x10^{-6}	2.0
0.01	3.56 x10^{-6}	2.5
0.1	2.17 x10^{-5}	7.5
0.5	9.26 x10^{-5}	11.0
1.0	1.32 x10^{-4}	11.0
2.0	1.25 x10^{-4}	9.0
2.5	1.25 x10^{-4}	9
5.0	1.56 x10^{-4}	8.0
7.0	1.47 x10^{-4}	7.0
10.0	1.47 x10^{-4}	6.5
14.0	2.08 x10^{-4}	7.5

Using these values and the flux bins from Figure 4.2.4 an estimation of dose can be created tracking the dose based on the number of days the sample remains in the NH-3 neutron howitzer. This is done through fitting the discretized energy bins into a dose factor bin. Due to the nature of the typical application (biological dose equivalent) of this table the values are quoted in rem/hr. However, because this work is only concerned with absorbed dose a simple conversion utilizing the Q-factor is performed. The Q-, or Quality Factor, is a conversion factor between absorbed dose and equivalent dose. Since, absorbed dose is the standard quantity for this work the Q factor was divided out to obtain the final absorbed dose estimation. From this point the flux is multiplied by the dose factor giving a dose rate in rad/hr. This can further be adjusted to units of Gy/hr simply by dividing by

100 since 1 Gy = 100 rad. A comparison of calculated absorbed dose in a 15 mm thick cylindrical sample of CaF_2 is demonstrated in Table 4.2.2. The comparison is between dose as calculated using neutron kerma factors and dose calculated using flux-to-dose conversion factors from NCRP-38 and ANSI/ANS-6.1.1-1977.

Table 4.2.2: Comparison of Dose values calculated by kerma factor and by dose factor using a discretized sampling of the flux spectrum as generated by the MCNP code.

Days in NH-3 Howitzer	Dose (Gy) from Kerma Factor	Dose (Gy) from Dose Factor
0	0.00	0.00
7	0.111	1.38
22	0.350	4.35
41	0.653	8.10
56	0.891	11.07
85	1.353	16.80
98	1.559	19.37
144	2.292	28.46
221	3.517	43.67

It was clear at this point that there was something amiss in the comparison of these calculations. Upon further examination, it was discovered that the flux-to-dose conversion factors in the MCNP manual are based on the kerma factors for human tissue as their primary application is for biological equivalent dose. Because, this work is focused on CaF_2, and the kerma factors for CaF_2 are quite different than that of human tissue, kerma factors were used to obtain dose values for this work. Please note that the utilization of kerma factors to estimate dose is accurate for charged particle equilibrium (CPE) environments which is a reasonable assumption for our samples. CPE for the recoil atoms is established very close to the crystal face so, except for a thin region near the crystal faces, CPE is a reasonable estimation. A full list of these kerma factors is included in Table 4.2.3.

Table 4.2.3: Kerma Factors for CaF$_2$ as quoted from Caswell [62].

Energy (MeV)	Kerma Factor (rad·cm^2)
0.002	7.36x10^{-13}
0.004	8.91x10^{-13}
0.006	1.15x10^{-12}
0.011	1.60x10^{-12}
0.020	2.49x10^{-12}
0.036	6.07x10^{-12}
0.063	1.06x10^{-11}
0.082	1.03x10^{-11}
0.086	1.49x10^{-11}
0.090	2.25x10^{-11}
0.094	3.67x10^{-11}
0.098	5.34x10^{-11}
0.105	3.85x10^{-11}
0.250	4.19x10^{-11}
0.500	5.71x10^{-11}
0.740	5.97x10^{-11}
1.05	7.69x10^{-11}

Energy (MeV)	Kerma Factor (rad·cm^2)
1.25	1.08x10^{-10}
1.50	1.06x10^{-10}
1.75	1.23x10^{-10}
1.95	1.44x10^{-10}
2.30	1.66x10^{-10}
2.50	2.15x10^{-10}
2.70	2.39x10^{-10}
3.10	2.99x10^{-10}
3.30	3.29x10^{-10}
3.50	3.75x10^{-10}
3.70	4.14x10^{-10}
3.90	4.54x10^{-10}
4.20	5.35x10^{-10}
4.60	6.21x10^{-10}
5.00	6.62x10^{-10}
5.40	7.46x10^{-10}
5.80	8.35x10^{-10}

Energy (MeV)	Kerma Factor (rad·cm^2)
6.00	8.45x10^{-10}
6.20	8.54x10^{-10}
6.60	8.83x10^{-10}
7.00	9.53x10^{-10}
7.40	9.95x10^{-10}
7.80	1.02x10^{-9}
8.00	1.05x10^{-9}
8.20	1.07x10^{-9}
8.60	1.13x10^{-9}
9.00	1.16x10^{-9}
9.40	1.21x10^{-9}
9.80	1.27x10^{-9}
10.50	1.38x10^{-9}
11.50	1.56x10^{-9}
12.50	1.72x10^{-9}
14.50	1.88x10^{-9}
15.5	1.96x10^{-9}

From these kerma factors a dose chart can be developed to show the accumulated dose in a sample placed in the NH-3 Howitzer over time. This dose chart is shown in Figure 4.2.5 as the secondary axis while the primary axis shows the total neutron fluence associated with a particular dose.

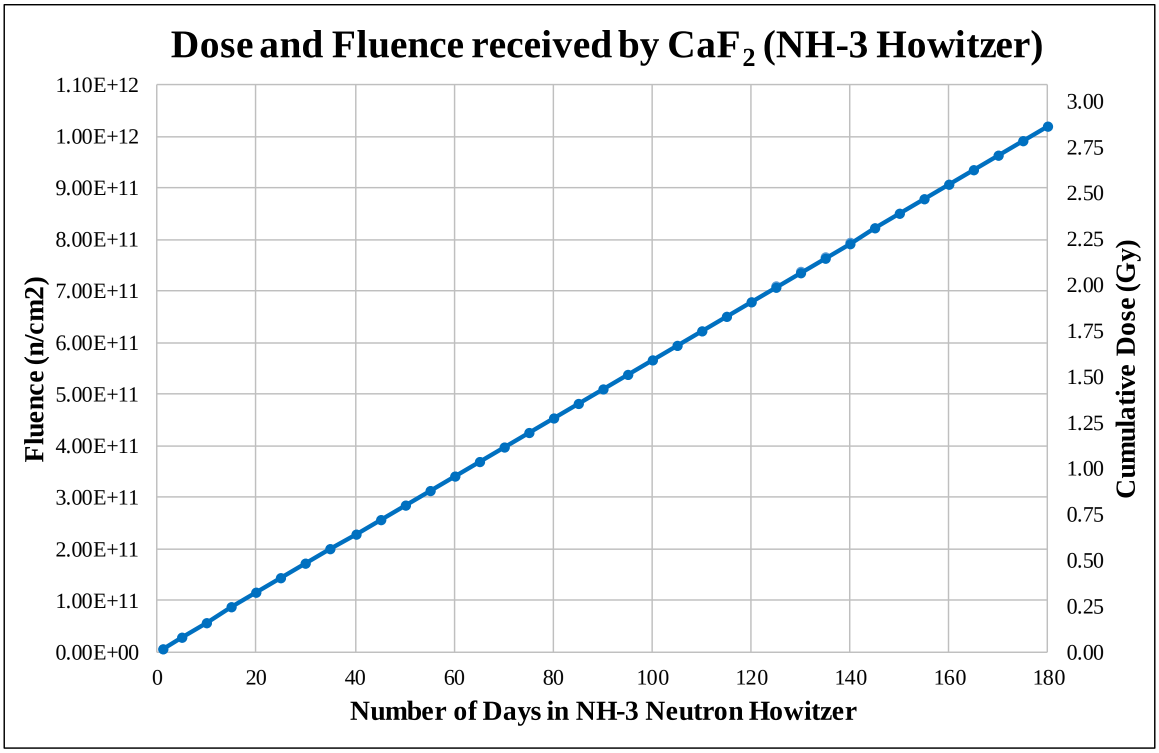

Figure 4.2.5: Estimated dose rate in CaF_2 samples based on the number of days in the NH-3.

4.2.2 Sandia National Labs Irradiation Dose Estimation

Due to the complexity and other issues of extensive modeling the D-D and D-T fusion aspects of the Sandia irradiations the neutron fluence was reported back after irradiation. Given the mostly monoenergetic nature of the D-D and D-T produced neutrons it is possible, using kerma factors, to estimate a dose on the sample.

Using the appropriate values from Table 4.2.3 and the fluence received from the Sandia irradiations, the absorbed dose for the D-D neutrons in the material was calculated to be 5.16 cGy. Additionally, for the D-T neutrons the dose was calculated to be 3.10 Gy. This makes the total absorbed dose in the material 3.15 Gy. In comparison, it would take about 198 days to achieve this cumulative dose had the sample been subject to the NH-3 neutron Howitzer. A combined comparison of refractive index change in the sample placed in the Howitzer and the sample irradiated at Sandia National Laboratories will be presented in Section 5.7. As previously mentioned sample A15-5 was irradiated further at Sandia National Labs such that upon the second refractive index measurement the total absorbed dose was calculated to be 4.71 Gy.

4.2.3 Oregon State University Irradiation Dose Estimation

In a similar way to the Sandia irradiation experiments Oregon State University provided some very helpful information towards calculating the fluence and dose received in the irradiated samples. They have generated flux profiles for their TRIGA reactor utilizing two primary calculation methods. The primary method is through MCNP similar to what has been done in this research for the NH-3 neutron howitzer. Additionally, they have utilized STAY-SL, a dosimetry unfolding application with activation, dosimetry, and flux error calculation developed and maintained by the Nuclear Energy Agency (NEA). The CaF_2 crystals were placed in the G-Ring In-Core Irradiation Tube (GRICIT-C) region of the TRIGA reactor. The results of the calculated flux profile in this region are plotted in Figure 4.2.6.

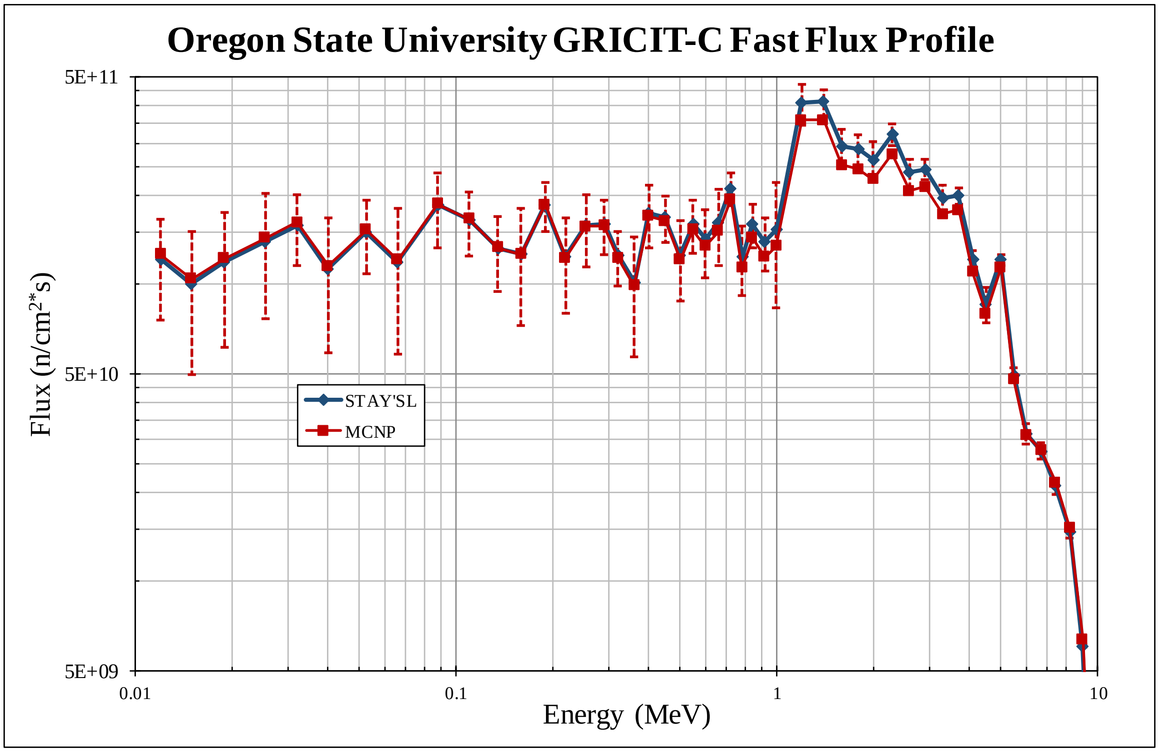

Figure 4.2.6: Plot of the MCNP and STAY'SL flux profile in the GRICIT-C region of the OSU TRIGA reactor. All doses in this work were calculated using the MCNP flux values.

Utilizing the data in Figure 4.2.6 a discretized calculation of dose can be performed in a similar way for both the Howitzer and the Sandia irradiation experiments were calculated. Utilizing the values already quoted in Table 4.2.3 and creating energy bins for the flux values in Figure 4.2.6 dose values were generated for these irradiated samples. As previously mentioned, sample B15-4 received a total neutron fluence of 1.70x10^{16} n/cm^2, sample B15-5 received a total neutron fluence of 1.70x10^{17} n/cm^2, and sample B15-3 received a total neutron fluence of 1.70x10^{18} n/cm^2. The dose calculated by this method for each of these irradiations was 1.99x10^4 Gy, 1.99x10^5 Gy, and 1.99x10^6 Gy (or 19.9 kGy, 199 kGy, and 1.99 MGy), respectively. By comparison, in order to achieve this dose within the NH-3 Howitzer the sample would have to be irradiated for about 420 millennia.

Chapter 5: CaF_2 Irradiation Results and Analysis

5.1 Overview

The experimental thrust of this research is the ability to perform precise measurements of the change of refractive index in a CaF_2 crystal sample. An array of CaF_2 samples were irradiated according to the plan laid out in Section 4.1. Table 5.1.1 shows the range of neutron fluences, energy fluences, absorbed doses received by the various CaF_2 samples. Values separated by a dash (–) indicate that the sample was irradiated continuously and measurements were taken at various points between the lower and upper bounds indicated. Values separated by an ampersand (&) indicate that the sample was irradiated a fixed number of times and measured at the values indicated.

Table 5.1.1: Master table showing the neutron fluence, energy fluence and absorbed dose values associated with each irradiated CaF_2 sample. Doses were calculated using MCNP and provided fluence values for energies above 2 keV. Per Chapter 2, 2 keV is close to the required neutron energy to create a PKA that will cause a damage cascade.

Master Table of CaF_2 Irradiation Values				
Sample ID	Irradiation Source	Neutron Fluence (n/cm^2)	Energy Fluence (MeV/cm^2)	Absorbed Dose (Gy)
A15-1	N/A	N/A	N/A	N/A
A15-2	N/A	N/A	N/A	N/A
A15-3	Howitzer	$5.95x10^9$	$2.97x10^{10}$	0.0159
A15-4	Howitzer	$4.16x10^{10}$ – $1.31x10^{12}$	$2.08x10^{11}$ – $6.57x10^{12}$	0.11 – 3.52
A15-5	Sandia	$1.85x10^{11}$ & $2.68x10^{11}$	$2.37x10^{12}$ & $3.49x10^{12}$	3.15 & 4.71
A15-6	Howitzer	$1.04x10^{10}$ – $3.88x10^{10}$	$5.20x10^{10}$ – $1.94x10^{11}$	0.028 – 0.104
B15-1	N/A	N/A	N/A	N/A
B15-2	N/A	N/A	N/A	N/A
B15-3	OSU	$1.70x10^{16}$	$1.95x10^{16}$	$1.99x10^4$
B15-4	OSU	$1.70x10^{17}$	$1.95x10^{17}$	$1.99x10^5$
B15-5	OSU	$1.70x10^{18}$	$1.95x10^{18}$	$1.99x10^6$

Contain within this chapter are the results of the periodic measurements taken of each of the samples mentioned in Table 5.1.1. All calculated doses only include incident neutrons greater than or equal to 2 keV due to the required PKA energy for semi-permanent damage as calculated in Chapter 2.

5.2 *Obtaining Results*

This section will serve to indicate the basic process for how results are obtained combining all of the theory and practice discussed to this point. In order to obtain accurate and consistent results despite some of the difficulties presented in this work the first step was to establish two or more control samples that served to correct for variation due to laboratory environment, cavity parameter drift, and other unquantified errors. Frequency ratio measurements for the control samples were completed before and after every irradiation experiment along with the measurement of the irradiated sample (or non-irradiated sample in the case of the pre-irradiation baseline measurements). By utilizing the frequency ratio results for the control samples, the correction described in Section 5.4 for the correction of the Howitzer data was utilized. This correction is added to the original baseline measurement of the frequency ratio for the pre-irradiated sample, correcting the baseline to appear as if it had been measured the same day as the post-irradiation measurement. Then the division of the pre-irradiation frequency ratio by the corrected post-irradiation measurement was completed, per Equation 30 (also shown previously as Equation 25), where the subscript 0 represents the pre-irradiation values and the subscript 1 represents the post-irradiation values, to find a super ratio.

$$\mathbb{R} = \frac{\mathcal{R}_0}{\mathcal{R}_1} = \frac{n_{p,fp,1}}{n_{p,fp,0}} = \frac{n_{p,fp,0} + \Delta n_{p,fp}}{n_{p,fp,0}} = 1 + \frac{\Delta n_{p,fp}}{n_{p,fp,0}} \qquad \text{(Eq. 30)}$$

At this point, Equation 30 is solved for $\Delta n_{p,fp}$ to obtain the change in refractive index of the crystal. After this a comparison of the super ratio of the control samples was completed. The super ratio between control samples should not change. However, a change was witnessed and therefore suggests some other unquantified variation in the system. The variation in the super ratio value was applied to the uncertainty in the change of refractive index for each measurement, thus obtaining the final reported results.

5.3 Correcting for Daily Variation in Frequency Ratios

As previously discussed, the primary forms of measurement that produce the data to be analyzed come in the form of the repetition rate of the cavity in frequency units, ν_{rt}, and the repetition rate of the FPE, ν_{fp}, in frequency units. Dividing ν_{rt} by ν_{fp} results in the standard frequency ratio we used for analysis of the sample as demonstrated by Eq. 24. This ratio is obtained for each measurement pre- and post-irradiation, for multiple samples.

Also, as mentioned in Section 3.6, a minimum of two control samples were also measured on each day an irradiated sample was measured, allowing for a correction to be made as to the daily variation in the frequency ratio. In the case of the NH-3 neutron Howitzer irradiations, samples A15-1 and A15-2 were measured as control samples. and Later, B15-1 and B15-2 were also added as control samples. Samples A15-3, A15-4, and A15-6 were irradiated. During the course of this research it was clear that over a period of days there were changes noticed in the frequency ratios between non-irradiated samples, so these are important to correct for when analyzing irradiated samples. This is completed in the way described in Section 3.6. These day to day changes result in a change in the frequency ratio in controlled samples, shown in Figure 5.3.1.

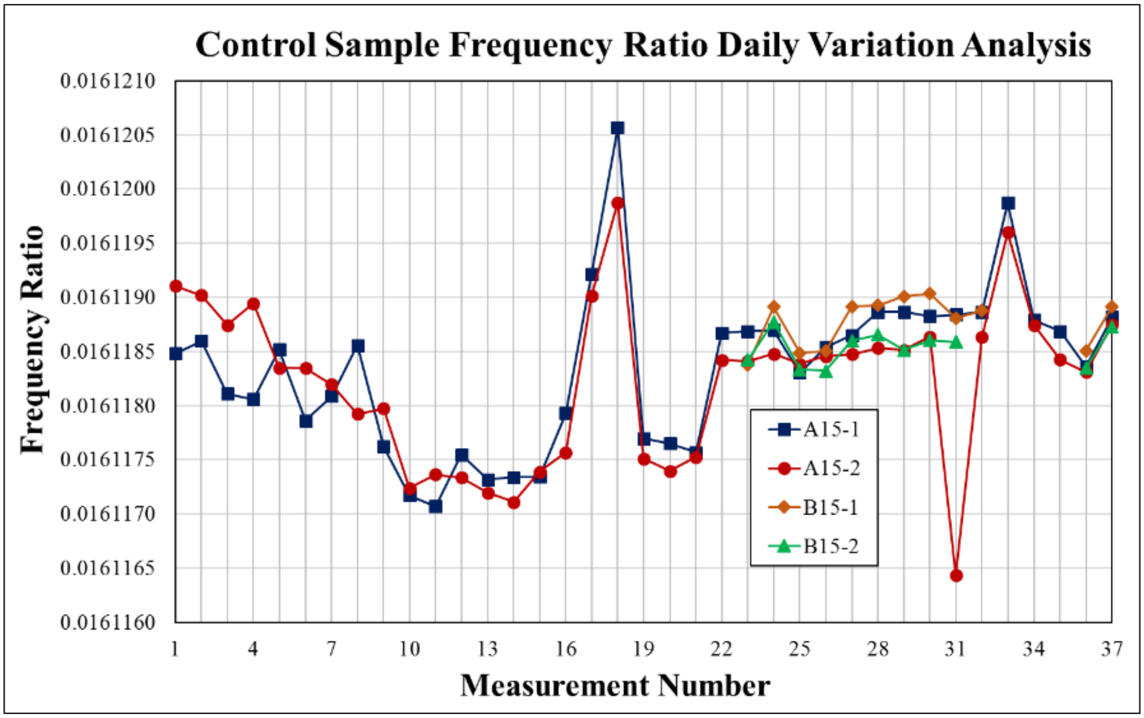

Figure 5.3.1: Variation in frequency ratio of unirradiated control samples A15-1 and A15-2, as well as the later included control samples B15-1 and B15-2. The total time period of measurements occurred between June 29, 2016 and May 5, 2017.

This change in frequency ratio, in turn, creates an incorrect illusion of the change of refractive index in the controlled samples. As mentioned in the calibration and stability chapter, these daily variations have been identified to be due, in part, to the laboratory environment, specifically to humidity and pressure. Details on this are discussed in Appendix B.

A close monitoring of the lab from July 21, 2016 through February 17, 2017 has revealed an average temperature of 23.2 ± 0.7 ˚C, an average humidity of 26 ± 11 %, and an average pressure of 847.0 ± 4.8 mbar, a small variation in all three values. This date range is representative of the daily laboratory environment and measurements were taken during each experiment in order to track changes that could be caused by the laboratory environment.

Repeating this experiment under much more stable laboratory environments for four control samples that were used for the OSU TRIGA irradiation data yielded a more stable plot of the frequency ratio. It should be noted that the span of dates for these measurements was only 4 days. This data also supports the expectation that this daily variation is largely tied to laboratory environments since the laboratory environment was more stable for these measurements. The environment averaged a temperature of 23.1 ± 0.5 ˚C, an average humidity of 20 ± 2%, and an average pressure of 843.8 ± 4.4 mbar. A plot of the results from this secondary test on non-irradiated control samples is shown in Figure 5.3.2. The y-axis values are the same as in Figure 5.3.1 for comparison.

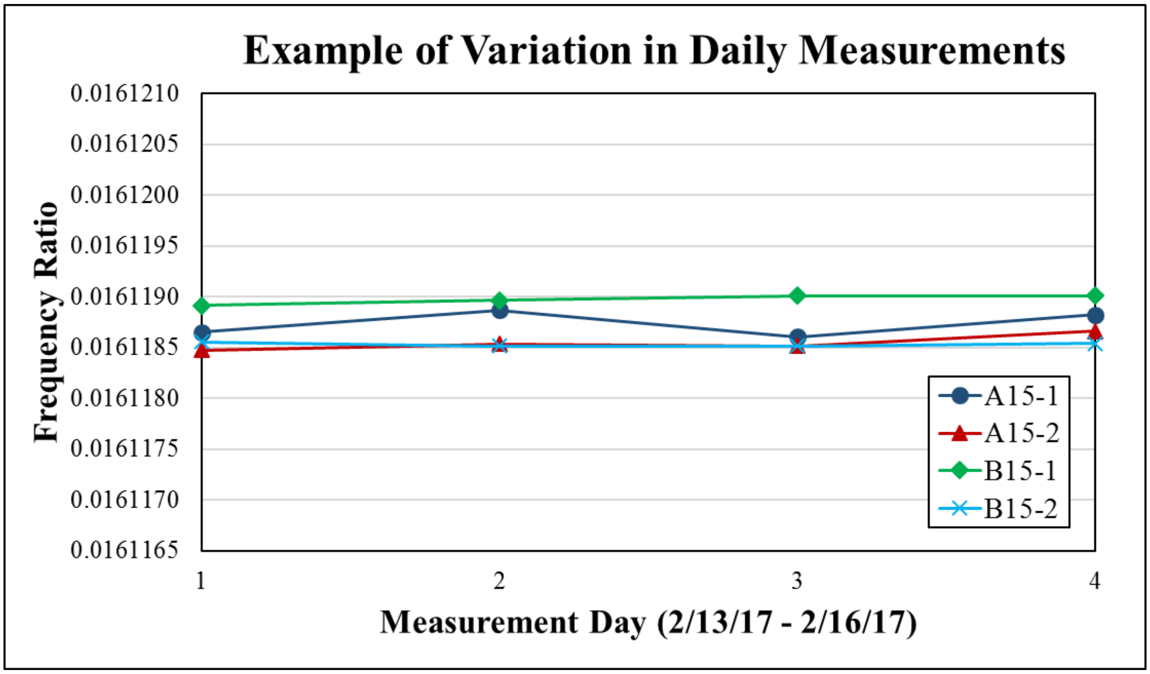

Figure 5.3.2: Secondary daily variation experiment with much better laboratory environment stability.

The data in Figure 5.3.2 demonstrates a higher stability in the data. However, there is still some notable deviation, particularly with sample A15-1. It should also be noted, for future error analysis, that when considering the variation in these four data points of sample A15-1, there is an “apparent” refractive index change averaging 9.62x10^{-6}.

This daily variation phenomenon can be corrected for (with some uncertainty) by determining the change in refractive index of the irradiated samples by utilizing the control sample data. By obtaining the frequency ratio for the control samples on the same days as the irradiated samples are measured, it is possible to create a correction for the irradiated data utilizing the data obtained for the control samples. Without this correction, due the precise nature of the changes being measured, the data would appear to be random following the pattern created by the drift of the laser cavity on a given day which can be minutely effected by temperature and humidity as well as more noticeably effected by dust and changes in the cavity required to maintain mode-locking. Changes in the cavity due to the current setup are necessary and inevitable and on occasion, they too can be corrected for utilizing a correction algorithm based on this data. An ancillary examination of potential reasons for the cause of these daily changes was completed. This examination is included as Appendix B.

In order for a data correction to be made, the difference between the daily measurement and the original day measurement is acquired and subtracted from the measurement of the irradiated sample for that day. This is demonstrated by the correction algorithm in Equation 31.

$$\mathcal{R}_{Correctyed,n} = \mathcal{R}_{Raw,n} - \Delta\mathcal{R}_{C,n} \qquad \text{(Eq. 31)}$$

$$where\ \Delta\mathcal{R}_{C,n} = \{\mathcal{R}_{c,n} - \mathcal{R}_{c,0}\}$$

In these equations R_0 is the original baseline measurement for the controlled sample. $R_{C,n}$ designates the frequency ratio of the control sample on day n and $\Delta R_{C,0}$ is the original baseline measurement for the control. $\Delta R_{C,n}$ is the daily correction that is calculated using the change in the frequency ratio of the control sample between day n and the original baseline. $R_{raw,n}$ is the ratio of the test crystal for day n. By subtracting the daily correction from the raw ratio result of the irradiated sample a corrected value is generated which can then be combined with the original baseline of the irradiated sample to produce the super-ratio and then the change in refractive index. In the event of multiple control samples ΔR_C is calculated multiple times and the results are averaged before being added to $\mathcal{R}_{Raw,n}$ to extract the corrected ratio for the test crystal, $\mathcal{R}_{Corrected,n}$. After the baseline ratio is corrected for the irradiated sample the change in refractive index can be calculated by utilizing Equation 25 and Equation 26 from Section 3.3.4.

Given that the correction is necessary it is also necessary to apply some uncertainty to the stated correction. This can be accomplished by utilizing the scatter of the super-ratio of the control samples. Ideally, the super-ratio of control samples should remain constant when compared day to day. The daily variation is expected as previously discussed, but for measurements on the same day, without major environmental changes between measurements, should remain constant. By tracking the separation of the control samples, as seen in Figure 5.3.1, and applying the super ratio an uncertainty value can be applied to each corrected data point. The uncertainty, developed using the daily change in the super-ratio, represented in refractive index change, is demonstrated in Figure 5.3.3.

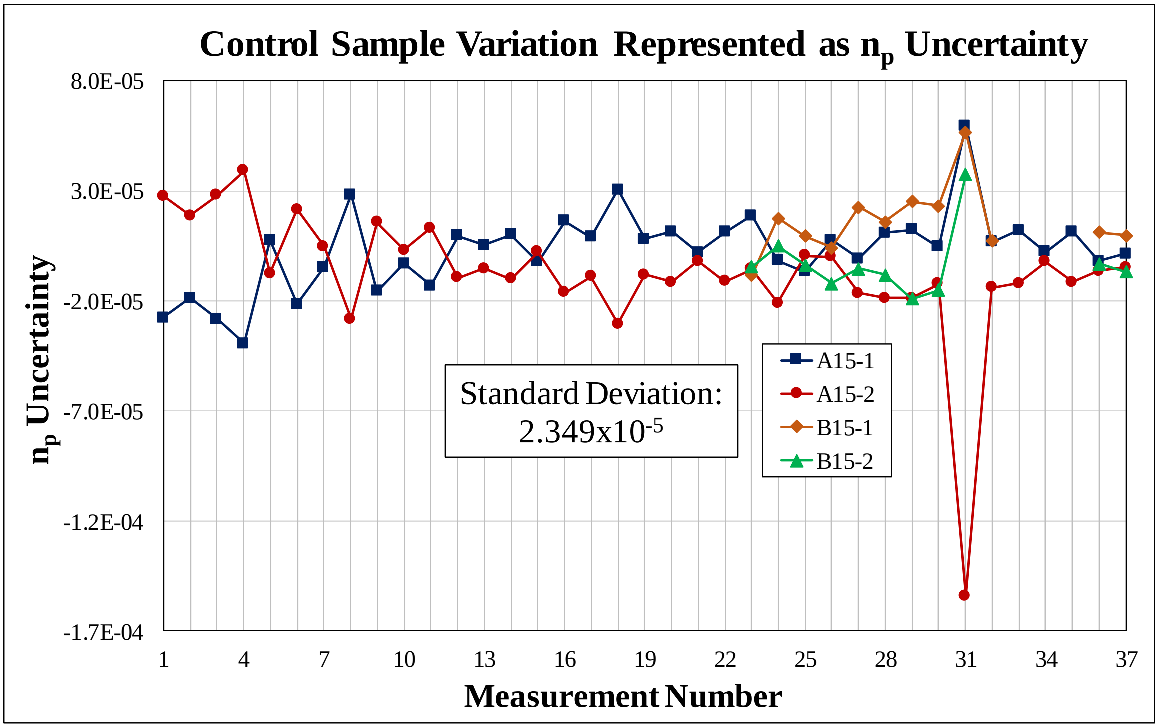

Figure 5.3.3: Confidence error in measurement correction by measurement day to be applied to the refractive index change calculated in the irradiated sample.

The uncertainty is ultimately determined by the standard deviation of data shown in Figure 5.3.3. This value applied to all refractive index change calculations after this point is $2.35\text{x}10^{-5}$ which for the remainder of this work will be simplified to $2.4\ \text{x}10^{-5}$.

For early data, these uncertainty calculations were based on only two unirradiated control samples. However, two additional control samples were added in for the later data, after recognizing the relatively high uncertainty associated with each data point. Several major cavity changes took place during the time frame this data was acquired and thus the uncertainty due these major cavity changes affecting the cavity dispersion, which in turn affects the group velocities and the group index of refraction, are included in this uncertainty calculation. Thus, for this work, the uncertainty calculation is considered quite robust. A further tightening of this uncertainty is desirable to lower dose applications but is outside of the scope of this work.

5.4 NH-3 Neutron Howitzer Irradiation Experiments

The first neutron howitzer experiment was a single irradiation of sample A15-3. The sample was placed inside the NH-3 Howitzer for 23 hours and 56 minutes for a dose of 0.0159 Gy. The sample was measured on four separate occasions after irradiation the average refractive index change measurement was $-1.1\text{x}10^{-5} \pm 0.5\text{x}10^{-5}$ (the uncertainty being the standard deviation of the four measurements). However, when the uncertainty, calculated above, is included the measured change in the refractive index falls within the noise of the uncertainty.

In order to increase refractive index change above uncertainties longer irradiations were planned for the NH-3 Howitzer. This primary Howitzer experiment ultimately included an accumulated irradiation of 221 days equating to approximately 3.52 Gy in sample A15-4. The correction was applied (as well as the uncertainty), using the two control samples A15-1 and A15-2, to sample A15-4 after each removal from the NH-3 howitzer to be measured. After each measurement, the sample was placed back into the howitzer for continued irradiation. The calculated change in refractive index in sample A15-4 is shown in Figure 5.4.1, plotted against absorbed dose as calculated from the NCRP-38 values quoted in the MCNP manual [63]. The uncertainty bars are representative of the uncertainty calculated from and displayed in Figure 5.3.3.

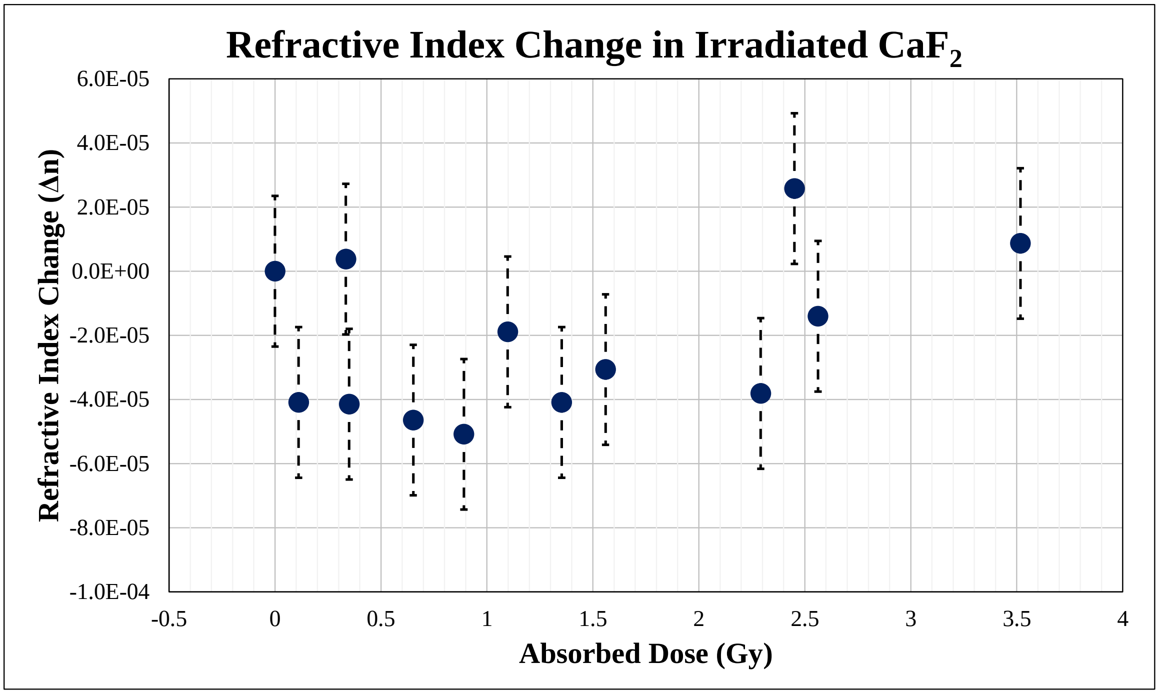

Figure 5.4.1: Demonstration of the Change in Refractive Index in CaF_2 *sample A15-4 which was exposed to PuBe Source Neutron Irradiation in the NH-3 Neutron Howitzer for 221 days.*

Figure 5.4.1 presents an inconclusive data set that seems to suggest that no refractive index change is being measured or the change that is occurring is smaller the uncertainty associated with the current measurement scheme. The modeling and simulation portion of this work suggests that radiation damage is a largely cumulative effect and thus the measured change is expected to consistently change over absorbed dose. Because of the witnessed jumps in data one final howitzer irradiation was completed to ensure that this data variation is due to the data uncertainty rather than a refractive index change. This was completed with sample A15-6 to add additional data points between zero days and seven days. The data produced is shown in Figure 5.4.2.

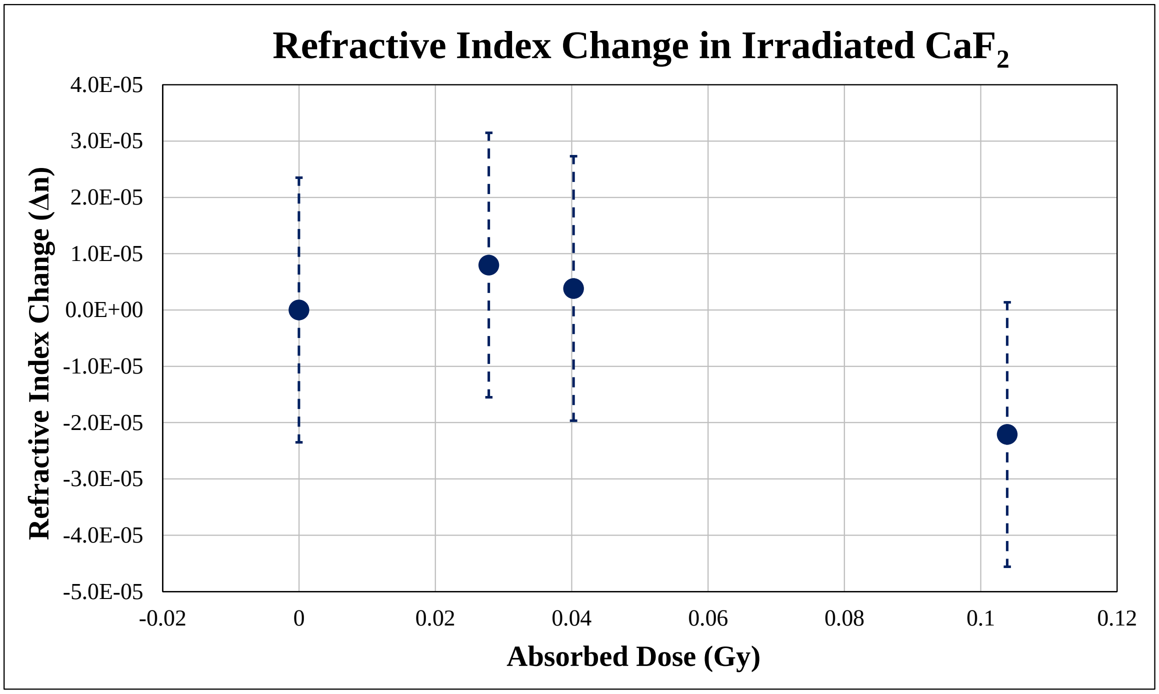

Figure 5.4.2: Final Neutron Howitzer irradiation with sample A15-6 irradiated from 0 to 7 days.

Figure 5.4.2 demonstrates that, while the changes are not quite as dramatic as those witnessed with the A15-4 irradiation, the jumps in the data points are consistently within the overall uncertainty and any witnessed refractive index change is lost within the uncertainty.

5.5 Sandia National Laboratories D-D and D-T Irradiation Experiment

The next result to consider was the irradiated sample (A15-5) exposed to Deuterium-Deuterium and Deuterium-Tritium fusion produced neutrons. This sample was exposed to a fluence of 2.35×10^{10} D-D neutrons/cm^2, at 2.91 MeV, and 1.55×10^{11} D-T neutrons/cm^2, at 14.79 MeV. Again, utilizing the flux-to-dose conversion factors the absorbed dose received in this sample was 3.15 Gy. Figure 5.5.1 demonstrates the measured refractive index change and shows all of the accumulated data measured for the Sandia irradiated

CaF_2 samples (A15-5) including three baseline measurements and eight post-irradiation measurements.

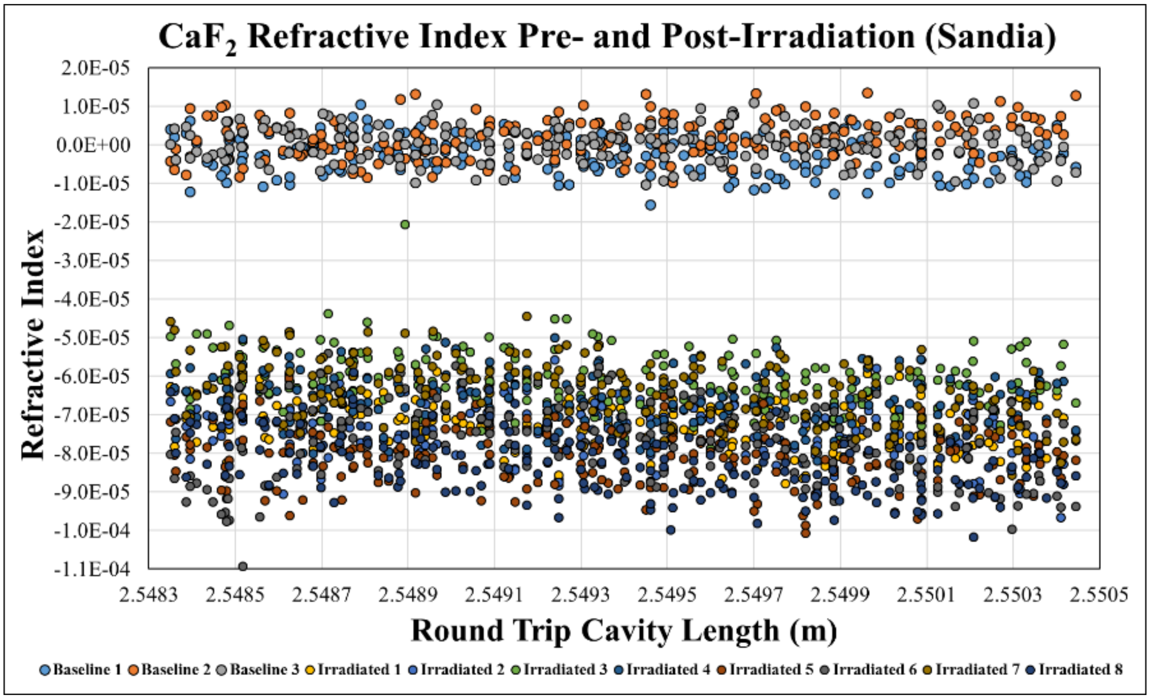

Figure 5.5.1: Demonstration of the full data set for the Sandia irradiated sample (A15-5) measured on eight separate occasions post irradiation and three separate pre-irradiation measurements.

The irradiated sample and the controls were measured eight times post-irradiation. Utilizing a correction accounting for the daily change in frequency ratio a change in refractive index averaging $-6.4\times10^{-5} \pm 1.1\times10^{-5}$ was measured. Recalling that each measurement contains a set of at least 200 data points this change can also be represented by the individual data points.

While, there is a distinction between the baseline and the irradiated data points, it is also clear that there is a decent amount of variation in the data points even after applying the corrections. In Figure 5.5.1, measurements from different days are represented by the different colors, “irradiated 1” is a different day from “irradiated 2” and so on. There is an obviouse variation between the average RI measurements day by day, as represented previously in Figure 5.3.1. The level of variation must be considered in relation to the fact that the change in refractive index is so small for this particular sample. If this is the average amount of variation when measuring future samples that have received a higher dose of radiation, the variation will be much less significant. To visualize this Figure 5.5.2 displays the point by point mean of the measurements with their associated standard deviations. This plot gives a clearer example of the witnessed refractive index change in the FPE.

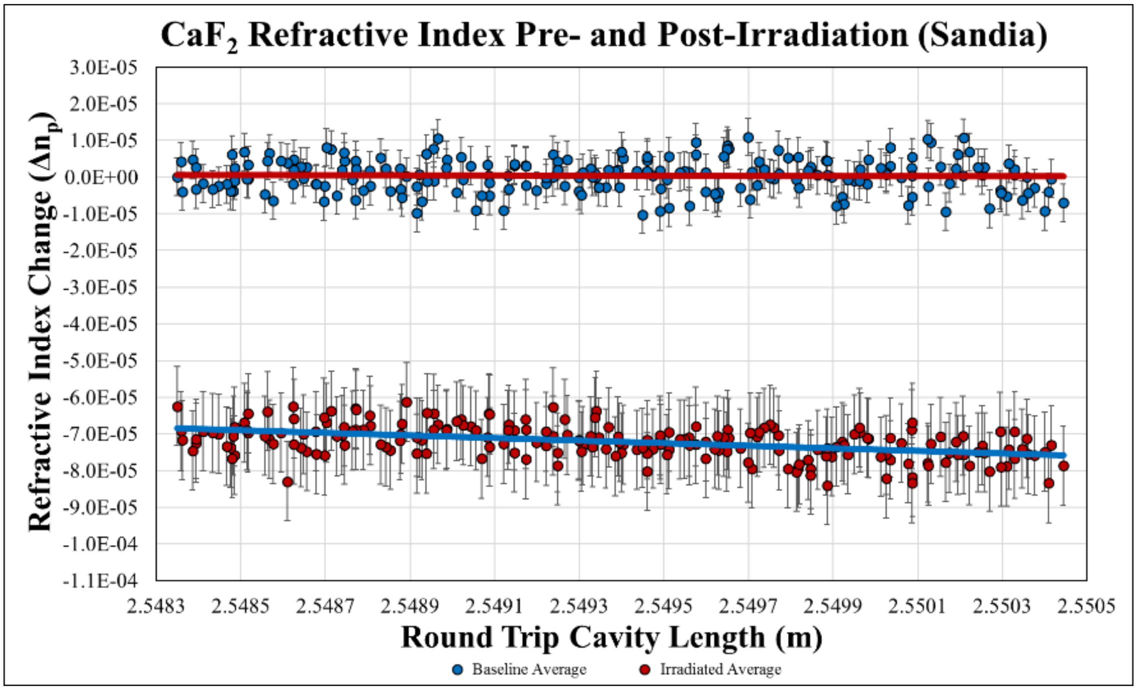

Figure 5.5.2: Mean values for the baseline and irradiated measurents for the Initial Sandia irraidated sample having recieved 3.15 Gy in absorbed dose.

As mentioned previously three measurements were utilized for the the pre-irradiation measurement of sample A15-4. The average of these three trials necessarily became the reference zero refractive index change point because the preirradiated sample had no change in and of itself. After the pre-irradiation measurement was corrected for daily variation utilizing the control samples A15-1 and A15-2. Within Figure 5.5.2 a single measurement of the pre-irradiated baseline is shown to demonstrate the variation in the baseline trials, while the post-irradiation measurement is a point-by point average of the eight separate post-irradiation measurements. Thus, the refractive index change value at each cavity length position is shown, relative to this zero. Additionally, there appears to be an exaggerated decline in the post irradiation measurement with increased cavity length with a greater negative slope than the baseline data. This particular phenomena is not completely understood, although it can also be stated that when comparing single cavity length scans that the slope of the ratio changes from time-to-time. A couple of factors that could play into this variation are the relative straight placement of the translation stage that the cavity end mirror is placed. Thus, if the end stage is not perfectly perpendicular to the beam path it could present drift similar to this.

It certainly appears here that there was a measured refractive index change however when again considering the uncertainty determined from Figure 5.3.3 rather than just the standard deviation of the data the plot becomes a change is a bit more ambiguous as shown in Figure 5.5.3. However, there still seems to be a clear change in refractive index for the first of the two Sandia irradiations.

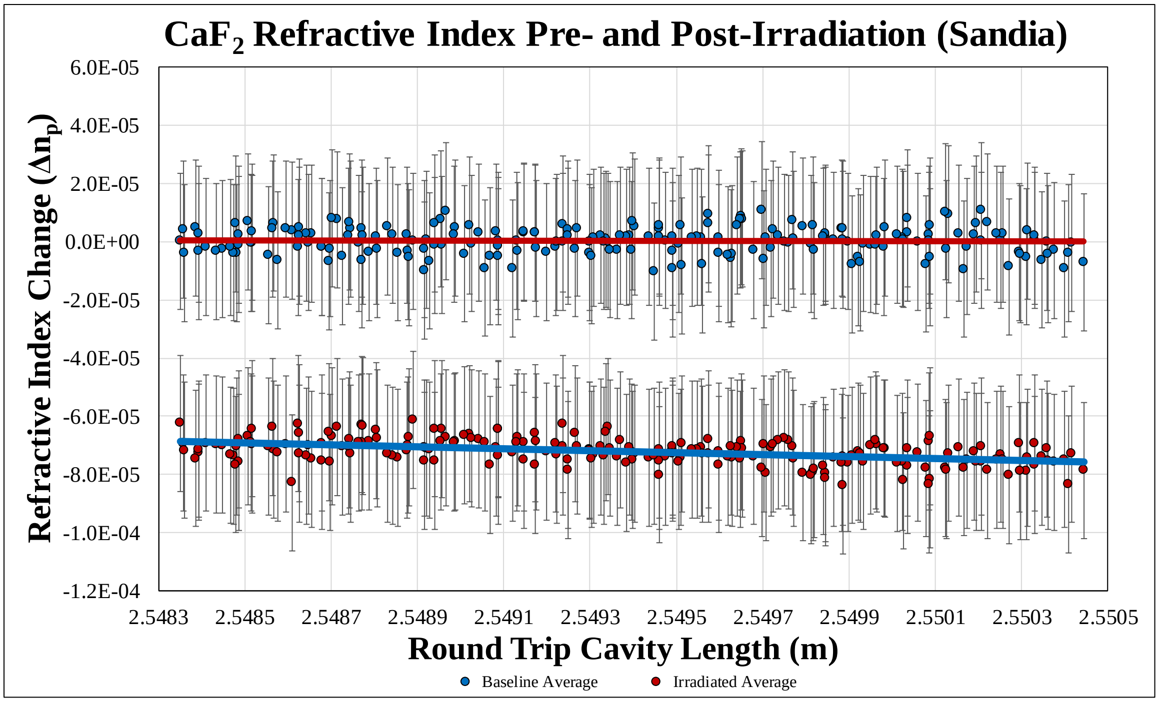

Figure 5.5.3: Initial Sandia irradiation results including overall uncertainty.

These results become much more ambiguous after the additional Sandia irradiation occurred. The additional irradiation added about 1.56 Gy of total absorbed dose in the sample. This brought the total absorbed dose to 4.71 Gy. The expectation given the previous irradiation data and the results from the modeling and simulation portion of this work was that the refractive index would decrease with more accumulated dose. However, the measured refractive index change in sample A15-5 after the second irradiation changed in the opposite direction of the expectation. Although, because of the uncertainty in the data this change is still within the expected error and perhaps what was measured with after the first Sandia irradiation was in fact not due to the change in refractive index but rather the daily variation in the data. The results of both irradiations of sample A15-5 are shown in Figure 5.5.4 demonstrating the positive index change measured after an additional 1.56 Gy of absorbed dose in the sample. A measurement, that if true, goes against understanding laid out earlier in this work. However, due to the previously analyzed daily variation it is not uncommon to see these changes when the refractive index change is small enough to be contained within the overall uncertainty of the measurements.

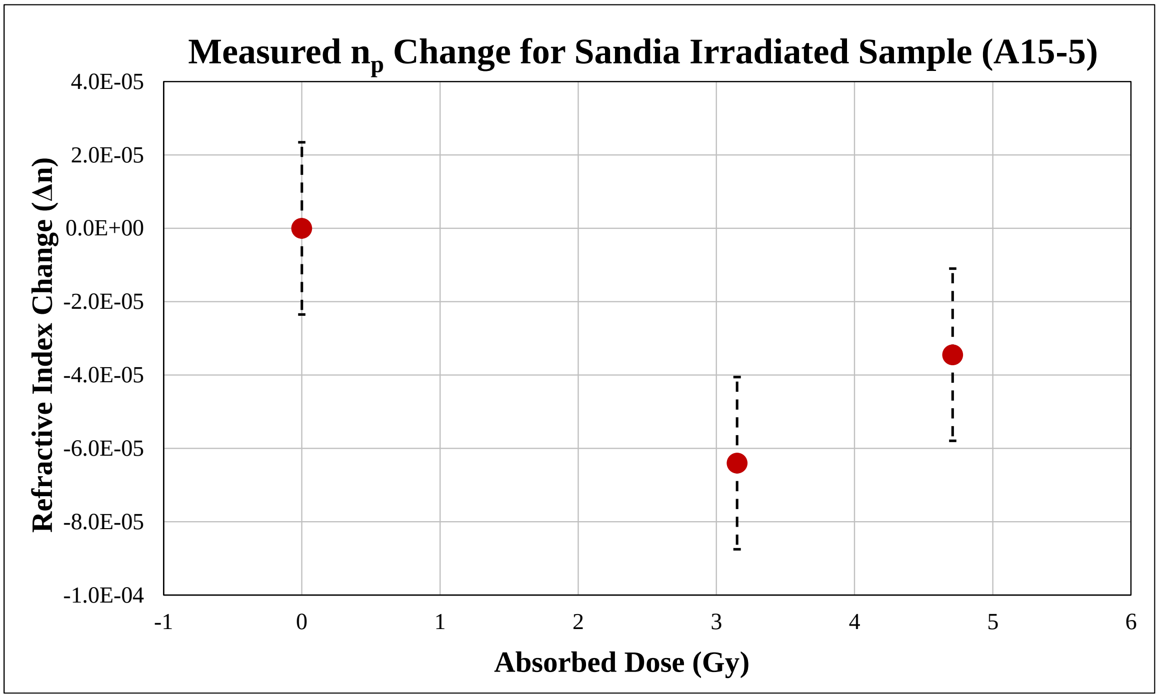

Figure 5.5.4: Refractive index change results for Sandia irradiations of sample A15-5.

5.6 OSU TRIGA Irradiation Experiment

All three of the samples irradiated at Oregon State University were returned in the time frame required for the completion of this work. These samples were B15-4, having received a total fast neutron fluence of 1.70×10^{16} n/cm^2, B15-5, having had received a total fast neutron fluence of 1.70×10^{17} n/cm^2 and sample B15-3, which received a total fast neutron fluence 1.70×10^{18} n/cm^2. Unexpectedly, these samples returned with a darkened color and were no longer clear. This is demonstrated in a side by side comparison of samples B15-5 (irradiated) and B15-1 (non-irradiated control) in Figure 5.6.1. This photograph demonstrates the darkening of the irradiated sample B15-5.

Figure 5.6.1: Side-by-side comparison of the OSU irradiated sample B15-5 and the non-irradiated control sample B15-1. This photograph demonstrates a darkening in the crystal due to the harsh environment of the OSU TRIGA reactor.

It is known that CaF_2 is quite susceptible to color centers which is expected to be the reason behind this darkening. A spectral analysis of the B15-5 demonstrated a transmission percentage in the region of operation for the nested cavity (792 nm) of only 48.08%. This value is compared to the non-irradiated transmission value of 94.5%. Needless to say, it was impossible to mode-lock this particular sample without addressing the darkening issue. It was noticed, however, that after attempting to mode-lock the cavity with this FPE inserted that in the small region where the laser beam passed through the crystal the darkening was “bleached” as shown in Figure 5.6.2. This effect is commonly understood as color centers are caused the trapping of electrons in quantum potential wells in a material. Thus, if the electrons in these potential wells are given enough energy to leave the well by perhaps, photons passing through the material the color centers tend to disappear.

Figure 5.6.2: Demonstration of the "bleaching" effect that occurred after attemping to mode-lock the cavity with this FPE inserted.

Utilizing this understanding, sample B15-5 was exposed to approximately 2 hours of high intensity green light. The high intensity of this light caused physical crystal heating and due to the possibility of annealing some of the radiation damage in the material from external heating the exposure to green light was deemed to not be the best approach for sample bleaching. It was, however, successful in bleaching to a degree as demonstrated by Figure 5.6.3.

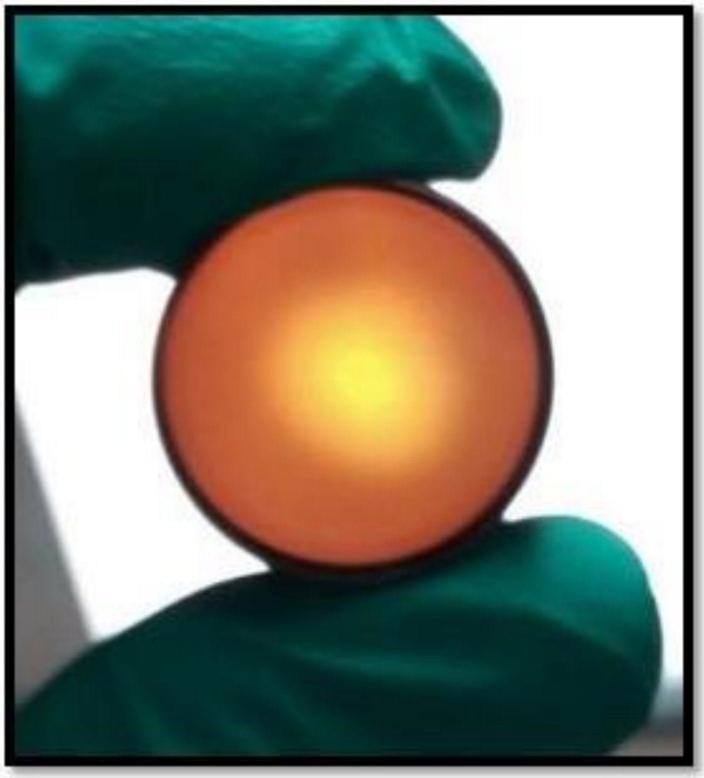

Figure 5.6.3: Sample B15-5 after approximately 2 hours exposure to high intensity green light effectively "bleaching" out color center in the CaF_2 sample.

The approach decided upon was based on the literature observed fact that ultraviolet (UV) light exposure is the most effective way to remove color centers because of the small wavelength and high energy nature of the photons. Thus, a high intensity UV arc lamp was utilized to expose the entire crystal. Additionally, utilizing UV light while at high energy is not sufficient to displace atoms from lattice sites and thus there was no expectation of impact on the index of refraction change measurements. After an exposure period of 36 hours the sample was removed from the UV light source and tested in the spectrometer to reveal a new transmission value, at 792 nm, of 84.72%. The visible result of this 36 hour “bleaching” is demonstrated in Figure 5.6.4.

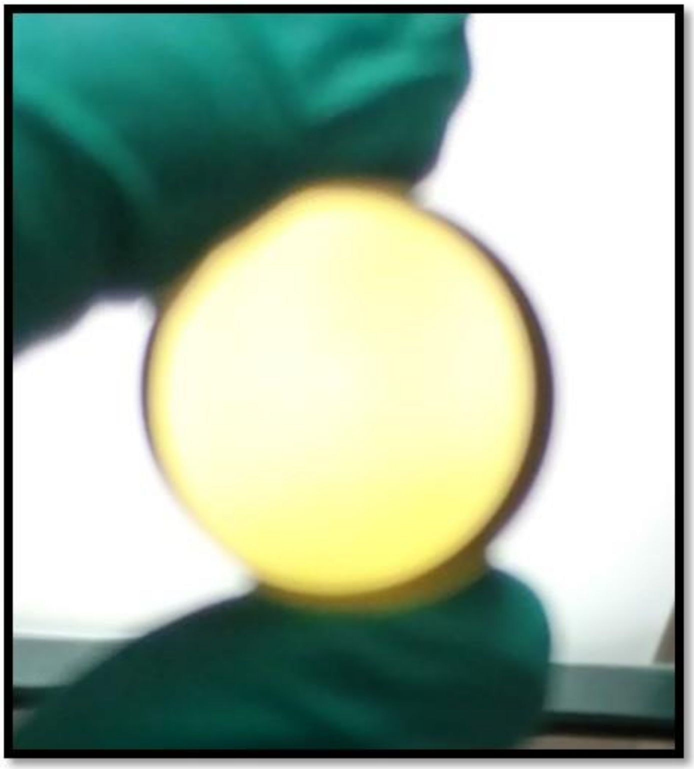

Figure 5.6.4: Sample B15-5 after 36 hours exposure to high intensity UV light, resulting in a transmission value at 792 nm of 84.72%.

This increase in transmission however, was still not sufficient to achieve mode-locking in the nested cavity and thus, more UV exposure was performed. Sample B15-5 was exposed to an additional 60 hours of high intensity UV light. The result of this additional exposure increased the transmission value at 792 nm to 89.33% resulting in a visible change demonstrated by Figure 5.6.5.

Figure 5.6.5: Sample B15-5 after a total of 96 hours of exposure to high intensity UV light, resulting, in an transmission value at 792 nm of 89.33%.

After this additional exposure, the nested cavity was right on the verge of mode-locking at 792 nm but even with increase laser power output it wasn't quite able to achieve mode-locking. However, with these three data points for transmission and exposure time to UV irradiation an estimation of the   This increase in transmission however, was still not sufficient to achieve mode-locking in the nested cavity and thus, more UV exposure was needed. However, due to the failure of the 200 W helium-xenon arc lamp it could not be completed as part of this work. Although, through a simple logarithmic calculation an estimate of the required exposure time was determined to be about 310 total hours exposure to a 200 W helium-xenon arc lamp in order to restore the sample closely to its original transmission state. Sample B15-5 was exposed to a total of approximately 276 hours of UV light at which mode-locking was able to occur after reaching a transmission percentage of 91.11%.

Sample B15-3, which was irradiated with $1.70\text{x}10^{18}$ fast n/cm^2, was measured for photon transmission immediately after the sample was returned and was only at 0.073% at 792 nm and appeared completely black when held up to a bright light. After 48 hours of UV exposure it recovered to 6.73% transmission at 792 nm. In total B15-3 was exposed to about 478 hours of UV light before mode-locking was achieved at a transmission percentage of 89.64%.

Sample B15-4 was the final sample returned, having received a total fast neutron fluence of $1.70\text{x}10^{16}$. The sample was in the reactor for 0.6 hours, compared to the 6 hours for B15-5 and 60 hours for B15-3. Upon return A15-4 had a transmission of 85.46% at 792 nm and was able to achieve mode locking at 92.14% after 48 hours of UV exposure.

An image of all three samples after various degrees UV exposure is included as Figure 5.6.6. At the point this image was taken all three irradiated samples were able to mode-lock and frequency ratio data was taken.

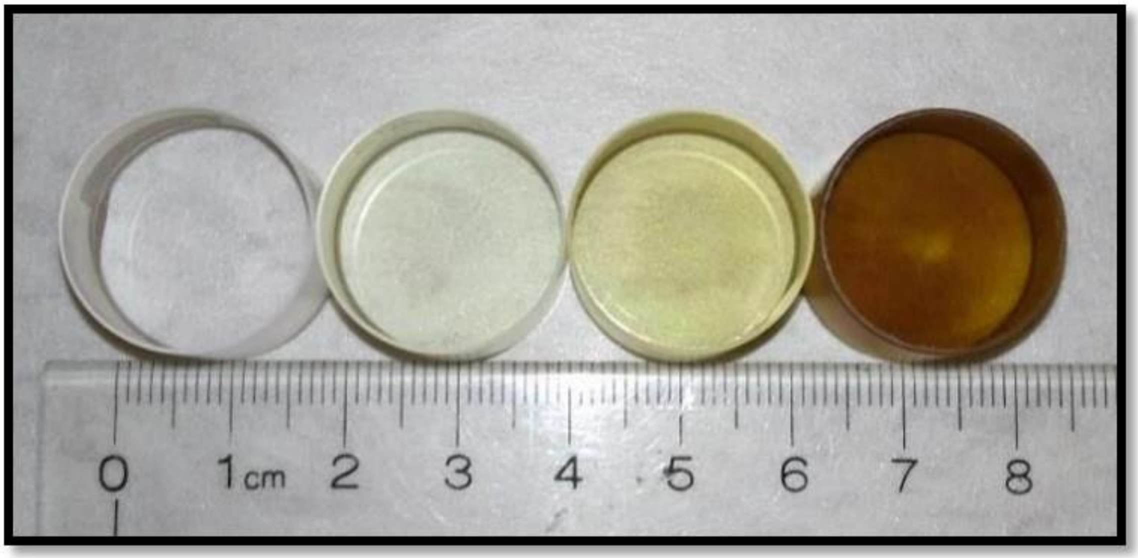

Figure 5.6.6: Image of unirradiated and irradiated CaF_2 crystals. Unirradiated on left and irradiated organized from left to right with least to most irradiation.

From these measurements, refractive index change was calculated and after applying the overall uncertainty Figure 5.6.7 demonstrates the results of the OSU irradiation experiments.

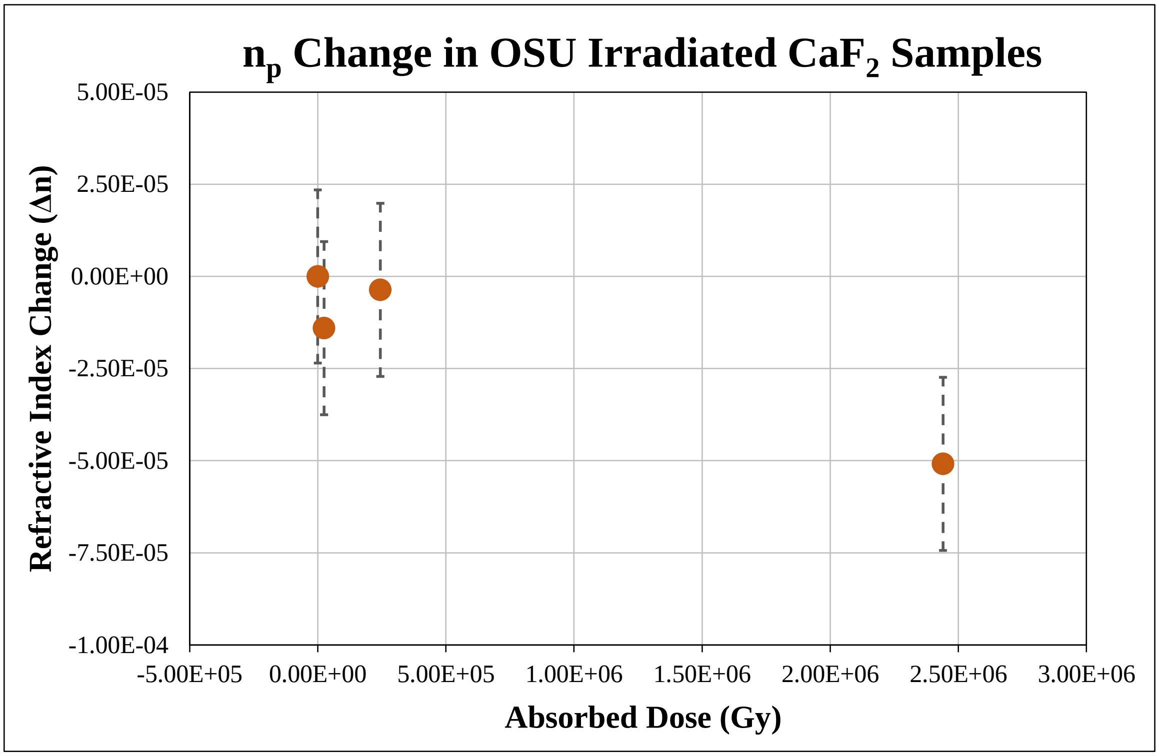

Figure 5.6.7: Refractive index change measurement results from OSU irradiated samples. B15-4 was irradiated to 1.99x10^4 Gy. B15-5 was irradiated to 1.99x10^5 Gy. B15-3 was irradiated to 1.99x10^6 Gy.

The data shown in Figure 5.6.7 demonstrates an overall downward trend in the data despite the results from B15-4. However, still due to the uncertainties a definitive refractive index change cannot be stated because of the small amount of refractive index change measured. Additional irradiations at higher neutron fluence, or a more thorough examination of the causes of the daily uncertainty, are required to confirm this trend in the data the results of the OSU irradiation experiments.

5.7 Combining Experiment Results

An important aspect of this research is the universal nature of measuring and relating the change in refractive index to a definable standard quantity within the nuclear realm. This is shown in Primak's work as a function of neutron fluence (n/cm^2) [5]. However, this is a somewhat deceptive quantity to correlate with refractive index change because as the modeling and simulation portion of this research has shown the energy of the neutron is a very important quantity, with number of displacements increasing with energy. Simply correlating refractive index change to neutron fluence the energy is erroneously ignored. If only neutron fluence was used, separate types of irradiation could never be compared or fit into the model unless they share and identical energy neutron source. If, however, a quantity including energy is utilized a model for refractive index change could be shared among different irradiation sources.

The ideal quantity for overall comparison is absorbed dose, the energy absorbed per mass of target material. Assuming the standard for calculating dose is uniform between comparisons the utilization of this quantity should enable comparison of refractive index change in separate samples having been exposed to separate irradiation sources. In the case of this research, the different irradiation sources are (1) the NH-3 neutron howitzer, (2) the Sandia D-D and D-T fusion produced neutron source, and (3) the Oregon State University TRIGA reactor.

To demonstrate this approach a plot was generated showing the refractive index change against absorbed dose (Figure 5.7.1) as calculated by the kerma factors defined earlier in Table 4.2.3.

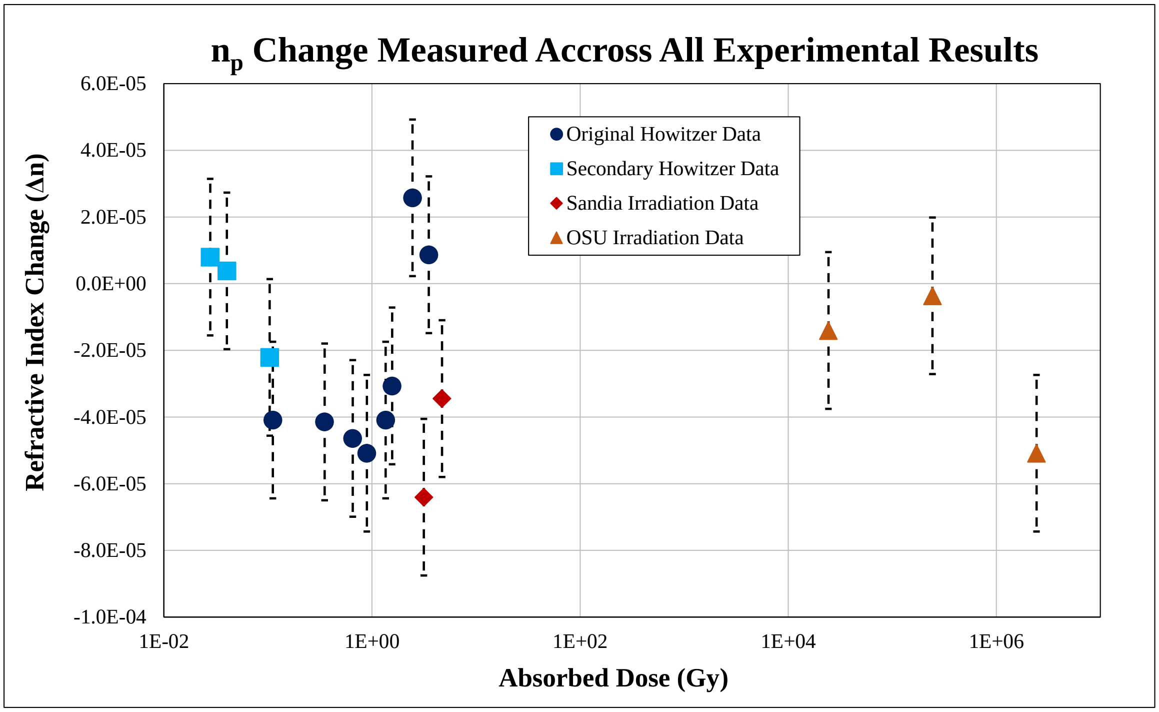

Figure 5.7.1: Refractive index change measured in all irradiated CaF_2 samples as a function of absorbed dose.

At first glance Figure 5.7.1 seems to show little correlation in the overall set of data collected from the various irradiations and measurement taken throughout this work. However, we will look more closely at this in the next section.

5.8 Data Trends

There are many things to take into account when considering data trends and overall quality of the full amount of data produced in this work.

The first consideration is expected refractive index change. This goes back to the Primak experiment with SiO_2 [5], the original inspiration for this work. It has been surmised though the modeling portion of this work and seen in Primak's experiments that refractive index decreases as density decreases. However, the neutron fluences experience in Primak's work [5] were one to three orders of magnitude greater than those included in this work. A recreation of the refractive index potion of the crystalline SiO_2 from Primak's work is shown in Figure 5.8.1 along with two curve fits of the data.

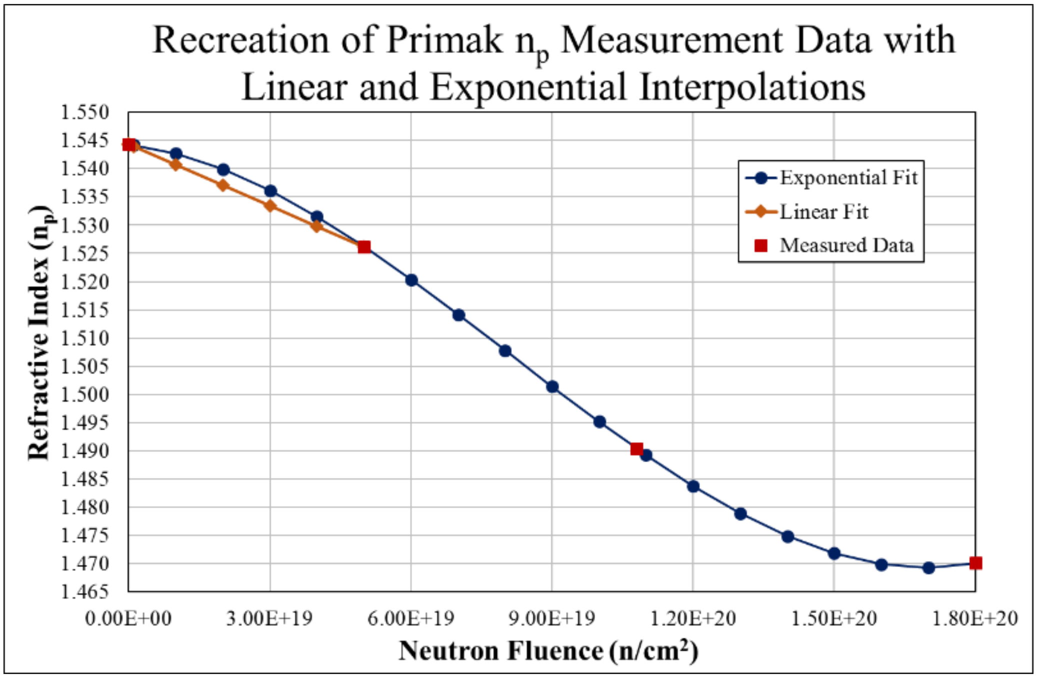

Figure 5.8.1: Recreation of Primak [5] refractive index measurement data.

Figure 5.8.1 shows an exponential interpolation of the Primak data as well as a linear interpolation of the first two data points. Utilizing these interpolations and assuming that CaF_2 crystals will behave in a similar way to the SiO_2 crystals, an estimation of the expected refractive index can be calculated for the neutron fluences and doses that have been explored in this research. Give that the overall uncertainty of this work was calculated to be $2.4x10^{-5}$ in order to witness a refractive index change that is outside of this uncertainty a minimum fluence of $1.70x10^{18}$ n/cm^2 (or dose of $1.99x10^6$ Gy) would have to be incident on a CaF_2 crystal. Sample B15-3 was the only measured sample to have achieved a fast neutron fluence of $1.70x10^{18}$ n/cm2 and thus if the behavior is similar in CaF_2 and SiO_2 the expected refractive index change is $-1.022x10^{-4}$ and $-3.62x10^{-4}$, for the exponential and linear interpolations, respectively. It should be noted that the measured refractive index change for sample B15-3 was $-5.1\text{x}10^{-5} \pm 2.4\text{x}10^{-5}$ which nearly contains the exponentially derived refractive index change expectation. With regard the rest of the data, per both the linear and exponential interpolations, anything below a fluence of $1.70\text{x}10^{18}$ n/cm^2 would be within the noise of the overall uncertainty.

The next consideration is the overall trend of the data. While it seems from Figure 5.7.1 that a trend would be difficult to extract one must consider that the x-axis is logarithmic and not linear. Thus, in order to better observe a potential linear data trend (which would be expected for these small fluence/dose values), a linear plot should be observed. Included as Figure 5.8.2 is a linear plot of this data with a linear curve fit followed by a semi-log plot of the data in Figure 5.8.3.

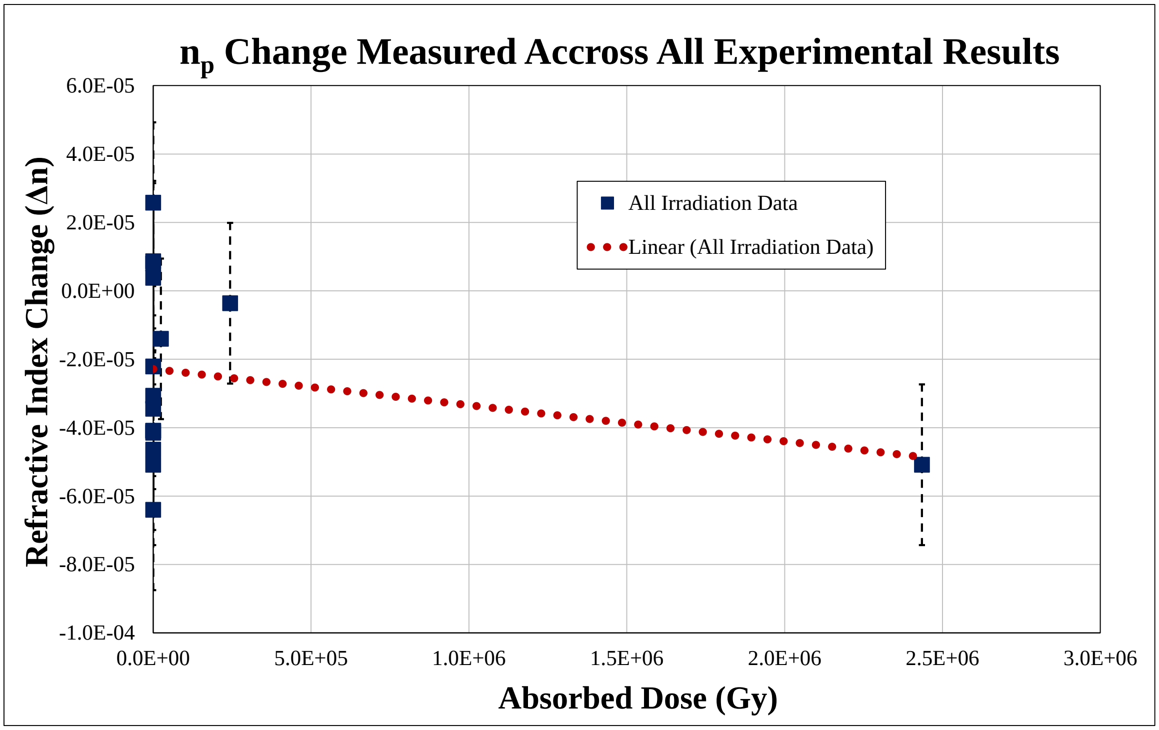

Figure 5.8.2: Plot of irradiation data on a linear scale demonstrating a decreasing trend in refractive index on average. The dotted line represents a linear curve fit of the data.

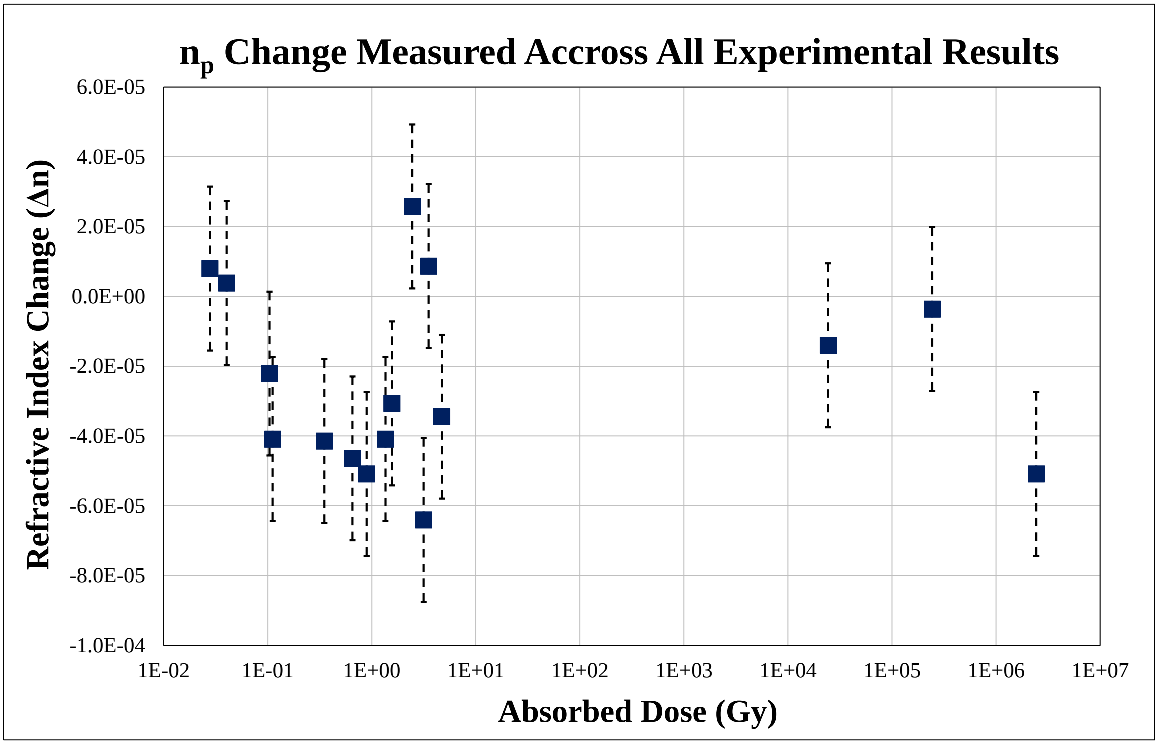

Figure 5.8.3: Plot of all irradiation data on a semi-log scale.

It seems that, overall there is a downward trend in the refractive index change measurements. This is however difficult to state with a large certainty for several reasons. The relatively low fluence of neutrons results in a low expected refractive index change. Additionally, the uncertainty of the overall data detracts from being able to definitively state a downward trend. In order to confirm this trend another irradiation at a fluence greater than 10^{18} n/cm^2 (corresponding to a dose greater than 1.99 MGy) is necessary or the overall uncertainty in the data must be decreased and the experiments must be repeated with a higher accuracy.

Another consideration that could be major factor in the frequency ratio measurements is the position of the various laser cavity components at the time of measurement. Due to the natural drift in the laser over time, periodic re-alignments were necessary and at times major cavity adjustments were required. When considering the NH-3 Howitzer data. The point at which the data begins to increase for the first time was directly after a small cavity adjustment and the large jump in the Howitzer data at about 2.5 Gy was directly after a major cavity adjustment in which prisms, focusing mirrors, and the end mirrors were adjusted. It should be noted that there is the possibility that the major cavity adjustment has a significant effect on the overall results. Additionally, all the OSU irradiation measurements were taken after this major cavity adjustment.

However, upon consideration of this fact there seemed to be little information to be gleaned from this fact especially after plotting both the measurements taken before and after this change, separately. There was no correlation in the slope of the data between the before-the-change and after-the-change measurements. It is, nevertheless, still possible that these changes in the cavity parameters can have effects on the frequency ratio and should be explored further to confirm or rule out any correlation.

Chapter 6: Conclusions

There were two primary facets to this research. Each focuses on the change in CaF_2 due to neutron irradiations from various sources. The modeling and simulation aspect of this work focused on the singular atomic scale collisions and their small and medium scale effects on crystal structure. A further examination was the change in refractive index of a crystal due to experimental exposure to neutron irradiation.

6.1 Neutron Damage and Effects Modeling

The results of the modeling and simulation portion of this research were limited in their applicability due to the inability to span the gap of the meso-scale within the time constraints of the current work. However, the research into single PKA damage cascade provides enlightenment into radiation damage cascades within CaF_2. CaF_2's crystalline structure, provides self-annealing properties on the picosecond scale. Through the examination of the damage cascades it was determined that the crystalline structure of CaF_2 provided a self-annealing of nearly 90% of the maximum displacements created. This means the crystal structure allows for 90% of the maximum displacements to either return to their original lattice site or be replaced by another atom of the same type. Prior to this work, the determination of the TDE of Ca and F atoms in CaF_2 had not been done utilizing molecular dynamics simulations, and as such is a valuable determination for the future of CaF_2 radiation damage research. In the end, the molecular dynamics analysis confirms a linear increase in the damage associated with a crystalline FPE with the energy of the incident neutrons in a PKA energy range from 100 eV to 5 keV.

6.2 Crystal Irradiation and Refractive Index Tracking

The results of the experimental aspect of this research are less than exciting but certainly intriguing. Refractive index change measurements were completed for a variety of irradiations performed in three different experimental apparatuses. Due to the current overall uncertainty calculated for this method many of the data points acquired were unable to be distinguished from the uncertainty noise. Additionally, the inevitability of periodic cavity re-alignments and the necessity of one major cavity adjustment in this work may have contributed to an additional error in the OSU data and the tail end of the NH-3 Neutron Howitzer Data. It was shown that the data point for B15-3, irradiated in the OSU TRIGA reactor was the only sample to achieve a fluence great enough to, in theory, change the refractive index beyond the overall uncertainty. However, potentially due to the aforementioned cavity adjustment, the OSU data appeared to have a refractive index change that was less than expected. When considering a linear scale there is certainly a downward trend in the data but in order to confirm this trend additional irradiations at fluences greater than $1.70\text{x}10^{18}$ are required. Additionally, a thorough examination of the effect of major and minor cavity adjustments are required for future exploration of this method as well as causes of the high overall uncertainly in measurement.

Regardless, an uncertainty of $2.4\text{x}10^{-5}$ (potentially smaller with further examination) in refractive index change measurements is a significant achievement in and of itself. This inevitably demonstrates an exceptional stability of the measurement technique, and testifies to the precision of this type of dosimetry with crystal FPEs.

Chapter 7: Future Work

7.1 Meso-Scale Modeling and Refractive Index Change Prediction

The focus of simulations was on a thorough modeling of the displacement thresholds of individual Ca and F atoms in CaF_2. This is extremely important as most damage is microscopic, and this contributes to most of the radiation effects [1]. It would be useful to be able to predict measurable bulk effects stemming from the small-scale effects. Future work applicable to this research could include bridging this gap utilizing theory developed and demonstrated by Norget, Torrens, and Robinson (NRT) [27] and also Nucleation Rate Theory [64]. By utilizing the parameters in this research, namely, the Threshold Displacement Energy values as well as the atomic binding energy values, a more applicable form of modeling can be completed. From here, a correlation could be made enabling a modeling and simulation based prediction of refractive index change due to specified neutron irradiation. Another useful examination would be utilizing MCNP to determine neutron particle track information (PTRAC) that can be exported to programs like SRIM to model the full-scale damage cascades caused by all the neutrons interacting in CaF_2 for a specific irradiation.

7.2 Irradiation Experimentation

It is expected that further irradiation experiments will continue to examine the correlation demonstrated in this research further. Being able to trace the change of refractive index all the way to the point it is rendered amorphous of the crystal due to irradiation damage would provide a full analysis of CaF_2. Additionally, CaF_2 is just one of a large set of materials that can be utilized for this type of dosimetry. This work could be repeated both in modeling, simulation, and experiment with a variety of crystals. Readily available, commercially produced FPE windows include sapphire, other fluoride compounds and crystalline quartz. Early examination of CaF_2 samples irradiated at OSU showed strong color center formation and darkening of the material. This is expected as halides are used for optically stimulated luminescence dosimeters which rely on trapped electron states. This provides an electron effect based mode for examining ionizing radiation, but non-darkening crystals would make refractive index measurements easier. Expanding beyond this work to include other crystal types will further demonstrate the viability of utilizing these techniques in neutron dosimetry applications.

7.3 Fiber Analysis

In order to approach the goal of real time analysis while a sample is being irradiated the laser cavity will need to be refined, minimized, and made portable or at the very least semi-portable. One way that this can be accomplished is by utilizing optical fibers and solid state lasers. The coupling and development of this would be another full dissertation in and of itself. However, it is a topic that needs to be considered for applying this technique to neutron dosimetry. The implementation of this research is limited in nature unless a development of a more portable version of this technique can be developed.

7.4 Uncertainty and Error Analysis

It has been made clear throughout this work that a thorough uncertainty and error analysis is needed to decrease the overall uncertainty that made the measurement of refractive index change so difficult in this research. This can be accomplished through a periodic changing of cavity parameters while tracking the frequency ratio change.

Additionally, a thorough analysis of the correlation of the laboratory environment should be completed to assess a more direct correlation between the laboratory environment and the frequency ratio drift.

7.5 Additional Irradiation and Crystal Variety

Lastly, due to the darkening of CaF_2 crystals at fast neutron fluences above 10^{16} it will be difficult to continue to higher fluences with CaF_2. Therefore another material must be considered. Fortunately, the change in refractive index effect is expected to be similar for all crystalline materials and thus there are many materials from which to chose. Two of the most readily available optical windows (to act as an FPE) are crystalline SiO_2 and AlO_3. Continuing to higher neutron fluences and doses in either of these crystals would be extremely beneficial in further validating this work.

References

[1] C. Dethloff, E. Gaganidze and J. Aktaa, "Quantitative TEM analysis of precipitation and grain boundary segregation in neutron irradiated EUROFER 97," *Journal of Nuclear Materials,* vol. 454, pp. 323-331, 2014.

[2] S. Zinkle and E. Hodgson, "Radiation-induced changes in the physical properties of ceramic materials," *Journal of Nuclear Materials,* vol. 191, no. A, pp. 58-66, 1992.

[3] A. Sand, S. Dudarev and K. Kordlund, "High-energy collision cascades in tungsten: Dislocation loops structure and clustering scaling laws," *EPL,* vol. 103, no. 46003, 2013.

[4] X. Yi, A. Sand, D. Mason, M. Kirk, S. Roberts, K. Kordlund and S. Dudarev, "Direct observation of size scaling and elastic interaction between nano-scale defects in collision cascades," *EPL,* vol. 110, no. 36001, 2015.

[5] W. Primak, "Fast-Neutron-Induced Changes in Quartz and Vitreous Silica," *Physical Review,* vol. 110, no. 6, pp. 1240-1254, 1958.

[6] S. Girard, J. Kuhnhenn, A. Gusarov, B. Brichard, M. Ban Uffelen, Y. Ouerdane, A. Boukenter and C. Marcandella, "Radiation Effects on Silica-Based Optical Fibers: Recent Advances and Future Challenges," *IEEE Transactions of Nuclear Science,* vol. 60, no. 3, pp. 2015-2036, 2013.

[7] A. I. Gusarov, D. Doyle, A. Hermanne, F. Berghmans, M. Fruit, G. Ulbrich and M. Blondel, "Refractive-Index Changes Caused by Proton Radiation in Silicate Optical Glasses," *Applied Optics,* vol. 41, no. 4, pp. 678-684, 2002.

[8] K. Masuda, "Intracavity coherent interaction of mode-locked pulse train with resonant medium," Doctoral Dissertation, University of New Mexico, 2014.

[9] K. Masuda and A. Hecht, "Novel techniques for high precision refractive index measurements, and application to assessing neutron damage and dose in crystals," *Nuclear Instruments and Methods in Physics Research A,* vol. 784, pp. 198-201, 2015.

[10] G. Cheymol, H. V. J.-F. Long and B. Brichard, "High Level Gamma and Neutron Irradiation of Silica Optical Fibers in CEA OSIRIS Nuclear Reactor," *IEEE Transactions on Nuclear Science,* vol. 55, no. 4, pp. 2252-2258, 2008.

[11] S. Plimpton, "Fast Parallel Algorithms for Short-Range Molecular Dynamics," *J Comp Physics,* vol. 117, pp. 1-19, 1995.

[12] H. D. Holland, "The Effect of Nuclear Radiation on the Structure of Zircon," *Acta Crystallographica*, vol. 8, pp. 291-300, 1955.

[13] D. R. Orlander, Fundamental Aspects of Nuclear Reactor Fuel Elements, United States: Technical Information Center, Office of Public Affairs, Energy Research and Development Administration, 1976.

[14] S. Tavernier, "Interaction of Particles in Matter," in *Experimental Techniques in Nuclear and Particle Physics,* Springer Berlin Heidelberg, 2010, pp. 23-53.

[15] S. Tavernier, Experimental Techniques in Nuclear and Particle Physics, Heidelberg: Springer, 2010.

[16] C. A. Becker, "Interatomic Potentials Repository Project," NIST - Material Measurement Laboratory, 13 May 2016. [Online]. Available: http://www.ctcms.nist.gov/potentials/. [Accessed 27 May 2016].

[17] C. A. Becker, F. Tavazza, Z. T. Trautt and R. A. Barque de Macedo, "Considerations for choosing and using force fields and interatomic potentials in materials science and engineering," *Frontiers in Methods for Materials Simulations,* vol. 17, no. 6, pp. 277-283, 2013.

[18] I. Malitson, "A Redetermination of Some Optical Properties of Calcium Fluoride," *Applied Optics,* vol. 2, no. 11, pp. 1103-1107, 1963.

[19] O. Heavens, Optical Properties of Thin Solid films, New York: Dover Publications, Inc., 1991.

[20] B. J. Cowen and M. S. El-Genk, "On force fields for molecular dynamics simulations of crystalline silica," *Computational Materials Science*, vol. 107, pp. 88-101, 2015.

[21] R. S. Averback and T. Diaz de la Rubia, "Displacement Damage in Irradiated Metals and Semiconductors," *Solid State Physics*, vol. 51, pp. 281-402, 1998.

[22] C. Erginsoy, G. H. Vineyard and A. Englert, "Dynamics of Radiation Damage in a Body-Centered Cubic Lattice," *Physical Review*, vol. 133, no. 2A, pp. A595-A606, 1964.

[23] M.-J. Caturla, D. L. Rubia, T. Diaz and G. Gilmer, "Point defect Production, Geometry and Stability in Silicon: a Molecular Dynamics Simulation Study," *Symposium A – Materials Synthesis and Processing Using Ion Beams,* vol. 316, pp. 141-146, 1993.

[24] L. Malerba and J. M. Perlado, "Basic mechanisms of atomic displacement production in cubic silicon carbide: A molecular dynamics study," *Physical Review B,* vol. 65, no. 4, p. 045202, 2002.

[25] W. Windl, T. J. Lenosky, J. D. Kress and F. V. Arthur, "First-principles investigation of radiation induced defects in Si and SiC," *Nuclear Instruments and Methods in Physics Research B,* vol. 141, pp. 61-65, 1998.

[26] E. Holmstrom, A. Kuronen and K. Nordlund, "Threshold defect production in silicon determined by density functional theory molecular dynamics simulations," *Physical Review B,* vol. 78, no. 4, p. 045202, 2008.

[27] M. J. Norgett, M. T. Robinson and I. M. Torrens, "A proposed method of calculating displacement dose rates," *Nuclear Engineering and Design,* vol. 33, no. 1, pp. 50-54, 1975.

[28] A. E693-12, "Standard Practice for Characterizing Neutron Exposures in Iron and Low Alloy Steels in Terms of Displacements Per Atom (DPA)," ASTM International, Conshohocken, 2012.

[29] B. J. Cowen and M. S. El-Genk, "Probability-based threshold displacement energies for oxygen and silicon atoms in a-quartz silica," *Computational Materials Science,* vol. 117, pp. 164-171, 2016.

[30] D. Chen, "Molecular Dynamics Simulation of Damage Cascade Formation in Ion Bombarded Solids," Masters Thesis, Texas A&M University, 2011.

[31] N. A. Capps, "Molecular Dynamics Simulations of Cascade Evolution near Pre-Existing Defects," Masters Thesis, University of Tennessee, 2013.

[32] G. Kinchin and R. Pease, "The Displacement of Atoms in Solids by Radiation," *Reports on Progress in Physics,* vol. 18, pp. 1-51, 1955.

[33] J. Brinkman, "Production of Atomic Displacements by High-Energy Particles," *American Journal of Physics,* vol. 24, pp. 246-267, 1956.

[34] A. Seeger, "On the Theory of Radiation Damage and Radiation Hardening," in *Proceedings of the Second United Nations International Conference on the Peaceful Uses of Atomic Energy,* Geneva, 1958.

[35] OECD/NEA, "Primary Radiation Damage in Materials," OECD/NEA, https://www.oecd-nea.org/science/docs/2015/nsc-doc2015-9.pdf, 2015.

[36] M. Gillan, "Collective dynamics in super-ionic CaF2: I. Simulation compared with neutron-scattering experiment," *J. Phys. C: Solid State Phys.*, vol. 19, pp. 3391-3411, 1986.

[37] N. de Leeuw and T. Cooper, "A computational study of the surface structure and reactivity of calcium fluoride," *J. Mater. Chem.*, vol. 13, pp. 93-101, 2003.

[38] K. Fa, A. Nguyen and J. Miller, "Hydrophobic Attraction As Revealed by AFM Force Measurements and Molecular Dynamics Simulation," *J. Phys. Chem. B,* vol. 109, pp. 13112-13118, 2005.

[39] S. Vyas, R. Grimes, V. Bulatov and M. Abramowski, "The Surface Structure of CaF2; A Comparison of Techniques," *Molecular Simulation,* vol. 26, pp. 307-321, 2001.

[40] M. W. Cooper, M. J. Rushton and R. W. Grimes, "A many-body potential approach to modelling the thermomechanical properties of actinide oxides," *Journal of Physics: Condensed Matter,* vol. 26, no. 10, 2014.

[41] M. L. Goldberger and K. M. Watson, Collision Theory, New York City: John Wiley & Sons, Inc., 1964.

[42] L. T. Chadderton, Radiation Damage in Crystals, London: Methuen & Co Ltd., 1965.

[43] R. Johnson and A. Orlov, Physics of Radiation Effects in Crystals, Amsterdam: Elsevier Science Publishers B.V., 1986.

[44] D. S. Billington and J. H. Crawford, Radiation Damage in Solids, Princeton: Princeton University Press, 1961.

[45] L. T. Chadderton and I. McC.Torrens, Fission Damage in Crystals, London: Methuen & Co Ltd, 1969.

[46] S. O. Kasap, Optoelectronics and Photonics: Priciples and Practices, Upper Saddle River, NJ: Prentice-Hall, Inc., 2001.

[47] E. Hecht, Optics, Pearson Education, Inc., 2017.

[48] P. W. Smith, "Mode-Locking of Lasers," *Proceedings of the IEEE,* vol. 58, no. 9, pp. 1342-1355, 1970.

[49] J.-C. Diels, Ultrashort Laser Pulse Phenomena, Albuquerque: Elsevier Inc., 2006.

[50] J. Ye and S. T. Cundiff, Femtosecond optical frequency comb: principle, operation, and applications, Norwell, MA: Springer, 2005.

[51] A. Lipson, S. Lipson and H. Lipson, Optical Physics, Cambridge University Press, 2010.

[52] K. Masuda, J. Hendrie, J.-C. Diels and L. Arissian, "Envelope, group, and phase velocities in a nested frequency comb," *Journal of Physics B: Atomic, Molecular and Optical Physics,* vol. 49, p. 095401, 2016.

[53] K. Zhao, Q. Zhang, M. Chini, Y. Wu, X. Wang and Z. Chang, "Tailoring a 67 attosecond pulse through advantageous phase-mismatch," *Optical Letters,* vol. 37, no. 18, pp. 3891-3893, 2012.

[54] J. Diels, J. Fontaine and F. Simoni, "Phase Sensitive Measurement," in *Proceedings of the International Conf. on Lasers*, McLean, VA, 1983.

[55] J.-C. M. Diels, J. J. Fontaine, I. C. McMichael and F. Simoni, "Control and measurement of Ultrashort Pulse Shapes (in amplitude and phase) with femtosecond accuracy," *Applied Optics,* vol. 24, no. 9, pp. 1270-1282, 1985.

[56] N. Corporation, "CMA Data Sheet," 2012.

[57] C. Ruiz, G. Chandler, G. F. D. Cooper, K. Hahn, R. Leeper, B. McWatters, A. Nelson, R. Smelser, C. Snow and J. Torres, "Progress in obtaining an absolute calibration of a total deuterium–tritium neutron yield diagnostic based on copper activation," *Review of Scientific Instruments,* vol. 83, no. 10D913, 2012.

[58] C. Ruiz, R. Leeper, F. Schmidlapp, G. Cooper and D. Malbrough, "Absolute calibration of a total yield indium activation detector for DD and DT," *Review of Scientific Instruments,* vol. 63, no. 10, pp. 4889-4891, 1992.

[59] Z. R. Harvey, "Neutron flux and energy characterization of a plutonium-beryllium isotopic neutron source by Monte Carlo simulation with verification by neutron activation analysis," Master's Thesis, UNLV, 2010.

[60] H. Vega-Carrillo, V. Hernandez-Davila, T. Rivera-Montalvo and A. Sanchez, "Characterization of a 239PuBe Isotopic Neutron Source," in *Proceedings of the ISSSD 2012,* 2012.

[61] F. H. Attix, Introduction to Radiological Physics and Radiation Dosimetry, New York, New York: John Wiley & Sons, Inc, 1986.

[62] R. Caswell, J. Coyne and M. Randolph, "Kerma Factors of Elements and Compounds for Neutron Energies Below 30 MeV," *Int. J. Appl. Radiat. Isot.,* vol. 33, pp. 1227-1262, 1982.

[63] NCRP-38, "Protection Against Neutron Radiation (1971)," NCRP, Bethesda, 1971.

[64] G. Was, Fundamentals of Radiation Materials Science: Metals and Alloys, New York: Springer, 2017.

[65] K. Birch and M. Downs, "An Updated Edlén Equation for the Refractive Index of Air," *Metrologia*, vol. 30, pp. 155-162, 1993.

Appendix A

A.1 LAMMPS TDE Equilibration Input File

```
# ============== Initialization ==============
units           metal
dimension       3
boundary        p p p
atom_style      charge #sphere

# ============== Atom Definition ==============
lattice  fcc 5.462
# From R. W. G. Wyckoff, Crystal Structures, 9th ed. (Interscience/John Wiley, New
# York, 1963), Vol. 1.
region CaF2Lattice block 0 1 0 1 0 1
create_box 2 CaF2Lattice
create_atoms 1 single 0 0 0
create_atoms 1 single 1 0 0
create_atoms 1 single 1 1 0
create_atoms 1 single 0 1 0
create_atoms 1 single .5 .5 0
create_atoms 1 single .5 0 .5
create_atoms 1 single 0 .5 .5
create_atoms 1 single 1 .5 .5
create_atoms 1 single .5 1 .5
create_atoms 1 single 0 0 1
create_atoms 1 single 1 0 1
create_atoms 1 single 1 1 1
create_atoms 1 single 0 1 1
```

```
create_atoms 1 single .5 .5 1
create_atoms 2 single .25 .25 .25
create_atoms 2 single .25 .75 .25
create_atoms 2 single .75 .25 .25
create_atoms 2 single .75 .75 .25
create_atoms 2 single  .25 .25 .75
create_atoms 2 single  .25 .75 .75
create_atoms 2 single .75 .25 .75
create_atoms 2 single .75 .75 .75
replicate 6 6 6

mass 1 40.0
mass 2 19.0
set type 1 charge 2.0
set type 2 charge -1.0

# ============== Force Fields ==============
pair_style hybrid/overlay table linear 15000 coul/long 15
kspace_style pppm 1e-5
pair_coeff 1 1 table Pot15_CaCa.lmptab Ca-Ca
pair_coeff 1 2 table Pot15_CaF.lmptab Ca-F
pair_coeff 2 2 table Pot15_FF.lmptab F-F
pair_coeff * * coul/long

# ============== Groups ==============
region rallatoms block 0 6 0 6 0 6
region rexterior block 1 5 1 5 1 5 side out
region rinterior block 1 5 1 5 1 5
```

```
region rinterior2 block 2 4 2 4 2 4
group crystal region rallatoms
group exterior region rexterior
group interior region rinterior
group in2_4 region rinterior2

# ============== Initialization ==============
compute 1 all temp
compute 2 all coord/atom 5.0
compute 3 all ke/atom
compute eng  all pe/atom
compute eatoms all reduce sum c_eng

# ============== Equilibration ==============
velocity crystal create 3.0 4928459

fix 1 all npt temp 293 293 .1 aniso .83993 .83993 1  #ABQ pressure = ~.83993 Bar
timestep 0.001
thermo 100
thermo_style custom step temp pe etotal press atoms vol density lx ly lz c_eatoms
dump id all custom 1000 dumpAll.dump mass type id x y z
dump id2 in2_4 custom 1000 dump2_4.dump mass type id x y z

#+200000 Equil
run 200000
variable natoms equal "count(all)"
variable teng equal "c_eatoms"
variable length equal "lx/6"
```

```
variable ecoh equal "v_teng/v_natoms"

print "Total energy (eV) = ${teng};"
print "Number of atoms = ${natoms};"
print "Lattice constant (Angstoms) = ${length};"
print "Cohesive energy (eV) = ${ecoh};"
print "Equilibration Completed!"

undump id
undump id2
unfix 1
write_restart 6xEquil.restart
```

A.2 LAMMPS TDE Input File (Example)

```
#  Looped TDE calc
variable i loop 500
label loop_i
clear
log 20eV_all.log append
print "Running simulation 20eV $i"
variable s equal 'floor(random(10,100000,1000))'
print "Random Seed = $s"
read_restart 6xEquil.restart

# ============= Force Fields =============
pair_style hybrid/overlay table linear 15000 coul/long 15
kspace_style pppm 1e-5
pair_coeff 1 1 table Pot15_CaCa.lmptab Ca-Ca
```

```
pair_coeff 1 2 table Pot15_CaF.lmptab Ca-F
pair_coeff 2 2 table Pot15_FF.lmptab F-F
pair_coeff * * coul/long

# ============== Groups ==============
group PKA id 1549     # Define PKA as a Ca atom (different for F TDE calc)

# ============== Initialization ==============
variable t equal "random(0,6.283185307,1000)"
variable p equal "random(0,3.141592654,1000)"
variable theta equal $t
variable phi equal $p
print "Theta (rad) = ${theta}"
print "Phi (rad) = ${phi}"
variable mkg equal '40.078 * 1.66054E-24 / 1000'
variable Ej equal '20 * 1.60218E-19'
variable speed equal 'sqrt(2 * v_Ej / v_mkg) * 0.01'
print "Energy (eV) = ${Ej}"
print "Mass (kg) = ${mkg}"
print "Speed (A/ps) = ${speed}"
variable x equal v_speed*cos(v_theta)*cos(v_phi)
variable y equal v_speed*sin(v_theta)*cos(v_phi)
variable z equal v_speed*sin(v_phi)
print "Velocity (A/ps) in X = $x"
print "Velocity (A/ps) in Y = $y"
print "Velocity (A/ps) in Z = $z"
compute 1 all temp
compute 2 all coord/atom 5.0
```

```
compute 3 all ke/atom
compute eng  all pe/atom
compute eatoms all reduce sum c_eng
compute disp all displace/atom

# ============== Atomic Randomization  ==============
dump 20eV PKA custom 20000 20eVPKA.dump mass type id x y z vx vy vz c_disp[4]
dump_modify 20eV append yes

velocity all create 293 $s
fix 1 crystal npt temp 293 293 .1 aniso .83993 .83993 1    #ABQ pressure = ~.83993 Bar
timestep .001
thermo 200
thermo_style custom step time dt temp pe etotal press atoms vol density lx ly lz c_eatoms

run 2000
unfix 1

velocity PKA set v_x v_y v_z
timestep 0.000005
fix 5 all dt/reset 10 1.0e-6 0.00008 .0008

# ============== 15000 Run ==============
fix 1 exterior npt temp 293 293 .1 aniso .83993 .83993 1      #ABQ pressure = ~.83993 Bar
fix 2 interior nve
run 18000

variable natoms equal "count(all)"
```

```
variable teng equal "c_eatoms"
variable length equal "lx/6"
variable ecoh equal "v_teng/v_natoms"
print "Total energy (eV) = ${teng};"
print "Number of atoms = ${natoms};"
print "Lattice constant (Angstoms) = ${length};"
print "Cohesive energy (eV) = ${ecoh};"

unfix 1
unfix 2

next i
jump Ca20eV.in loop_i
```

A.3 LAMMPS Cascade Equilibration Input File

```
# ============== Initialization ==============
units           metal
dimension       3
boundary        p p p
atom_style      charge #sphere

# ============== Atom Definition ==============
lattice  fcc 5.444
region CaF2Lattice block 0 1 0 1 0 1
create_box 2 CaF2Lattice
create_atoms 1 single 0 0 0
create_atoms 1 single 1 0 0
```

```
create_atoms 1 single 1 1 0

create_atoms 1 single 0 1 0

create_atoms 1 single .5 .5 0

create_atoms 1 single .5 0 .5

create_atoms 1 single 0 .5 .5

create_atoms 1 single 1 .5 .5

create_atoms 1 single .5 1 .5

create_atoms 1 single 0 0 1

create_atoms 1 single 1 0 1

create_atoms 1 single 1 1 1

create_atoms 1 single 0 1 1

create_atoms 1 single .5 .5 1

create_atoms 2 single .25 .25 .25

create_atoms 2 single .25 .75 .25

create_atoms 2 single .75 .25 .25

create_atoms 2 single .75 .75 .25

create_atoms 2 single  .25 .25 .75

create_atoms 2 single  .25 .75 .75

create_atoms 2 single .75 .25 .75

create_atoms 2 single .75 .75 .75

replicate 60 60 60


mass 1 40.0

mass 2 19.0

set type 1 charge 2.0

set type 2 charge -1.0


# ============= Force Fields =============
```

```
pair_style table/gpu linear 65536 pppm
kspace_style pppm 1.0e-3
pair_coeff 1 1 CaF2GPUAll.table CaCa
pair_coeff 1 2 CaF2GPUAll.table CaF
pair_coeff 2 2 CaF2GPUAll.table FF
pair_write 1 1 65536 r 0.06 6.5 CCAll.txt CaCa 2 2
pair_write 1 2 65536 r 0.06 6.5 CFAll.txt CaF 2 -1
pair_write 2 2 65536 r 0.06 6.5 FFAll.txt FF -1 -1

# ============== Groups ==============
region rallatoms block 0 60 0 60 0 60
region rinterior block 3 57 3 57 3 57
region rexterior block 3 57 3 57 3 57 side out
region rinterior2 block 15 45 15 45 15 45
region rinterior3 block 20 40 20 40 20 40
group crystal region rallatoms
group interior region rinterior
group exterior region rexterior
group in15_45 region rinterior2
group in20_40 region rinterior3

# ============== Initialization ==============
compute 1 all temp
compute 2 all coord/atom 5.0                        #all to interior
compute 3 all ke/atom                                    #all to interior
compute eng  all pe/atom
compute eatoms all reduce sum c_eng
```

```
# ============== Equilibration ==============
velocity crystal create 3.0 4928459

fix 1 all npt temp 293 293 .1 aniso .83993 .83993 1  #ABQ pressure = ~.83993 Bar
timestep 0.0005
thermo 100
thermo_style custom step temp pe etotal press atoms vol density lx ly lz c_eatoms
dump id all custom 5000 dumpAll.dump mass type id x y z vx vy vz
dump id2 in15_45 custom 5000 dump15-45.dump mass type id x y z vx vy vz
dump id3 in20_40 custom 5000 dump20-40.dump mass type id x y z vx vy vz

#+10000 Equil
run 10000

variable natoms equal "count(all)"
variable teng equal "c_eatoms"
variable length equal "lx/60"
variable ecoh equal "v_teng/v_natoms"

print "Total energy (eV) = ${teng};"
print "Number of atoms = ${natoms};"
print "Lattice constant (Angstoms) = ${length};"
print "Cohesive energy (eV) = ${ecoh};"
print "Equilibration Completed!"

write_restart 60xEquil.*.restart
```

A.4 LAMMPS Cascade 1000 keV PKA Input File (Example)

```
read_restart 60xEquil.*.restart

# ============== Force Fields ==============
pair_style table/gpu linear 65536 pppm
kspace_style pppm 1.0e-3
pair_coeff 1 1 CaF2GPUAll.table CaCa
pair_coeff 1 2 CaF2GPUAll.table CaF
pair_coeff 2 2 CaF2GPUAll.table FF
pair_write 1 1 65536 r 0.06 6.5 1000eV-CCAll.txt CaCa 2 2
pair_write 1 2 65536 r 0.06 6.5 1000eV-CFAll.txt CaF 2 -1
pair_write 2 2 65536 r 0.06 6.5 1000eV-FFAll.txt FF -1 -1

# ============== Groups ==============
#region rallatoms block 0 60 0 60 0 60
#region rinterior block 3 57 3 57 3 57
#region rexterior block 3 57 3 57 3 57 side out
#region rinterior2 block 15 45 15 45 15 45
#region rinterior3 block 20 40 20 40 20 40
#region rinterior4 block 25 35 25 35 25 35
#region rinterior5 block 5 55 5 55 5 55
#group crystal region rallatoms
#group interior region rinterior
group PKA id 2138761

# ============== Initialization ==============
compute 1 all temp
```

```
compute 2 all coord/atom 5.0
compute 3 all ke/atom
compute eng  all pe/atom
compute eatoms all reduce sum c_eng
compute disp all displace/atom

# ============== Equilibration ==============
velocity PKA set 0 0 -693.89

timestep 0.0000005
thermo 500
thermo_style custom step time dt temp pe etotal press atoms vol density lx ly lz c_eatoms
dump id1 in5_55 custom 500 1000eV.in5_55.a.dump type id x y z c_disp[4] c_eng c_3

#+260000 Run
fix 1 exterior npt temp 293 293 .1 aniso .83993 .83993 1      #ABQ pressure = ~.83993 Bar
fix 2 interior nve
fix 3 all dt/reset 10 5.0e-7 .0002 .005
run 260000

variable natoms equal "count(all)"
variable teng equal "c_eatoms"
variable length equal "lx/60"
variable ecoh equal "v_teng/v_natoms"

print "Total energy (eV) = ${teng};"
print "Number of atoms = ${natoms};"
print "Lattice constant (Angstoms) = ${length};"
```

```
print "Cohesive energy (eV) = ${ecoh};"

undump id1
unfix 1
unfix 2
unfix 3
write_restart 1000eVCol.*.restart
```

Appendix B

B.1 Overview

It became apparent during the course of this work that over an extended period of time there was a noticeable change in the frequency ratio (the primary value used to track the change in refractive index) beyond the normal standard deviation for the measurements. Due to the nature of the mode-locked laser cavity there are many factors that could influence this value change over a large span of days. Given that the majority of the cavity is filled with air the logical first thing to consider is the ambient laboratory environment. As it turned out there wasn't much cause to move beyond this evaluation because there was a clear pattern displayed in relating these changes to the ambient laboratory environment. Three laboratory environment variables were tracked consistently throughout this research, temperature, relative humidity, and absolute pressure. These values were considered separately initially and then combined to assess the correlation of the changes with air density and ultimately the refractive index of the air. The data in this appendix corresponds to the control sample measurements on the same days on which the NH-3 neutron howitzer irradiated sample (A15-4) was measured to obtain refractive index change.

B.2 Repetition Rate Change with Laboratory Environment Changes

The first correlation to consider was the change in the repetition rate with respect to ambient laboratory environment changes. As discussed in the main body of this dissertation the repetition rate of the cavity and the FPE are the essential building blocks for quantifying refractive index change in a material. As such their change with respect to the laboratory environment is of great interest. When considering the three variables separately the temperature of the lab was negligible and when plotted against the change in the repetition rate for both the cavity and the FPE there was no visible correlation. However, later when considering air density and refractive index change for the air in the cavity the temperature plays a larger role.

First, the change in the repetition rate of the cavity was considered with respect to the relative humidity in the lab. The results are depicted in Figure B.1.

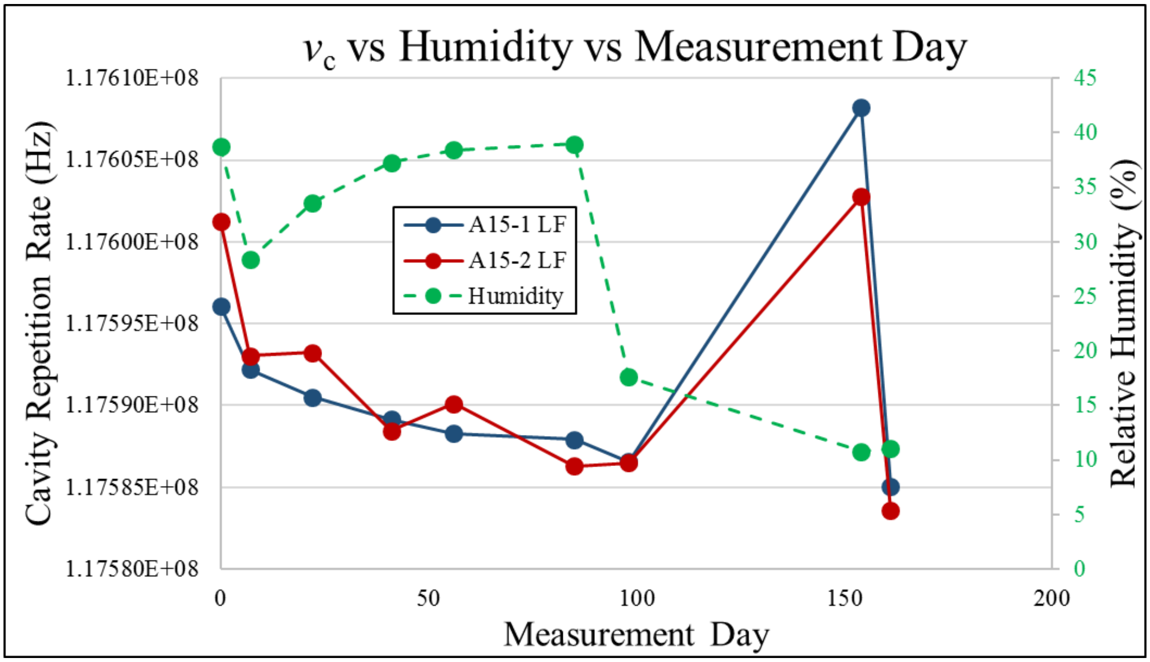

Figure B.1: Cavity repetition rate and relative humidity as measured on days the NH-3 Howitzer sample (A15-4) was measured for refractive index change.

The results shown in Figure B.1 are intriguing as they seem to follow an inverse relationship initially, however, on day 100 and after the relationship is severely diminished. Additionally, the frequency ratio was depicted with the pressure of the lab in mBar in Figure B.2.

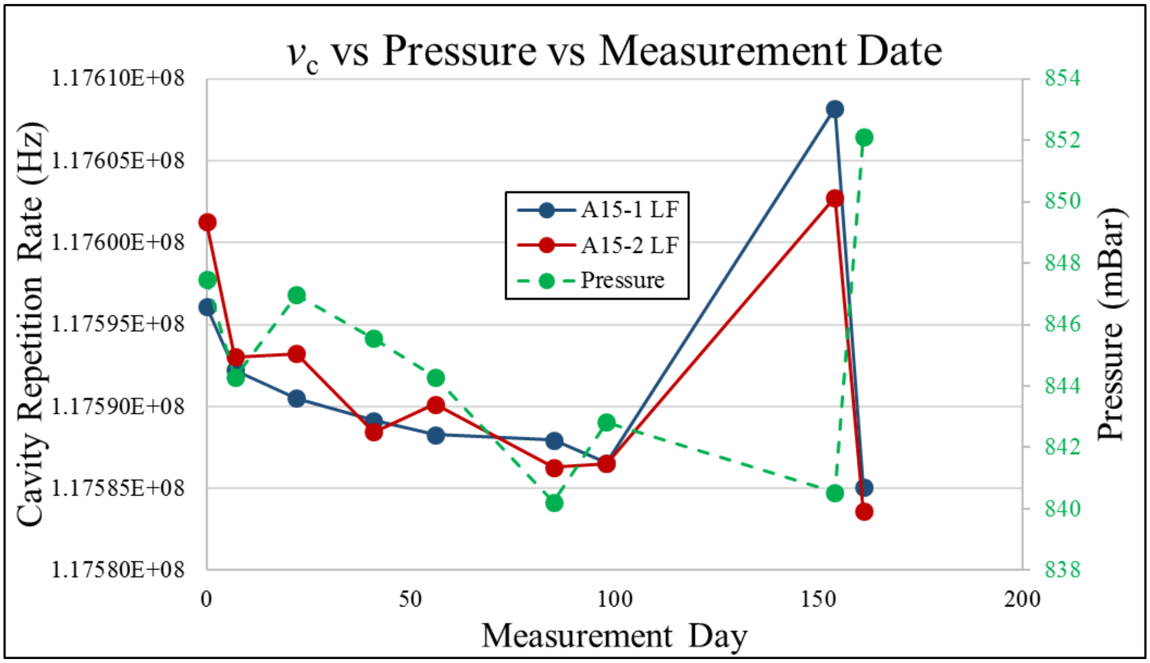

Figure B.2: Cavity repetition rate and relative humidity as measured on days the NH-3 Howitzer sample (A15-4) was measured for refractive index change

The results shown in Figure B.2 show similar behavior to the humidity results with the exception that they are reversed. The pressure results tended to follow a less consistent relationship early but around the same time frame as the humidity results the patter shifts and the repetition rate seems to adopt an inverse relationship to pressure. It appears that there is no definable relationship with humidity and pressure, alone. to the cavity repetition rate. It should be noted that Day 221 is excluded from Figure B.1 and Figure B.2 because of an extreme data jump. This was due to the choice to measure the frequncy ratios at a larger cavity length to increase stability. Frequency ratio results were not effected but plotting them here would deminish the ability to observe the correlations of the other data points. The consideration of the frequncy ratio in Section B.3 will include the data from 221.

B.3 FPE Repetition Rate with Laboratory Environment Changes

Second, the change in the repetition rate of the FPE was considered with respect to the relative humidity and pressure in the lab. It was not expected that the FPE data would produce any significant correlation, however, the lab environment can certainly affect this value and as such it must be considered. Figure B.3 and Figure B.4 show the change FPE repetition rate measured with relative humidity (Figure B.3) and pressure (Figure B.4) as measured on days that the NH-3 Howitzer sample A15-4 was removed and measured.

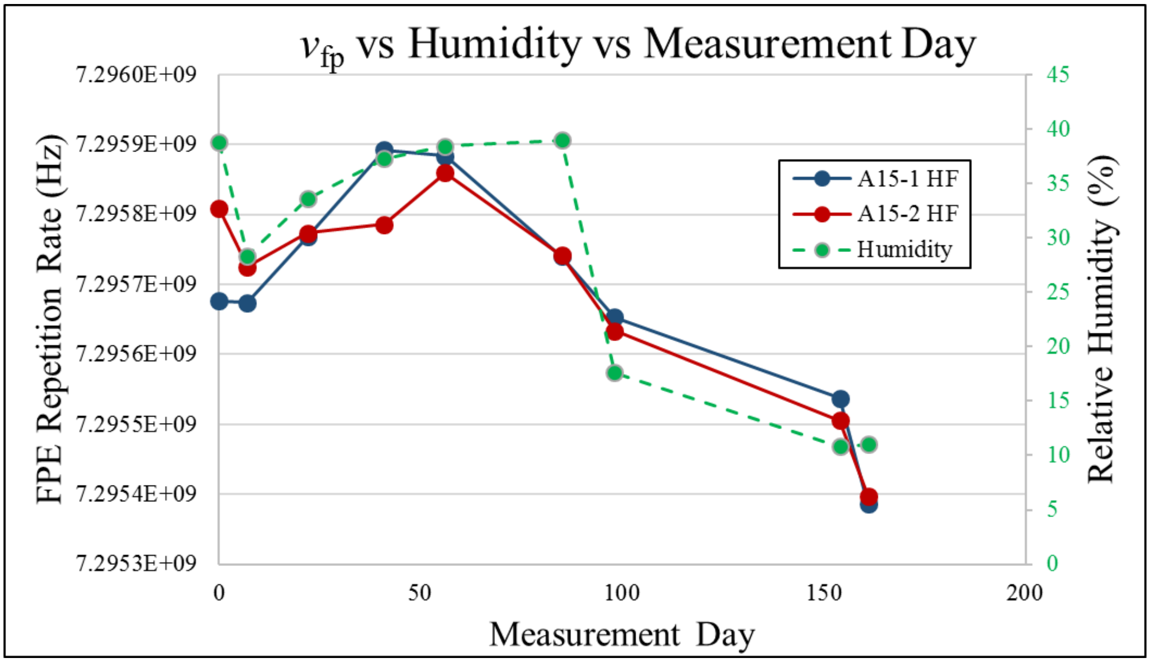

Figure B.3: FPE repetition rate and relative humidity as measured on days the NH-3 Howitzer sample (A15-4) was measured for refractive index change.

Figure B.3 shows that the FPE repetition rate varies quite similar to the relative humidity but it does not follow a strict pattern.

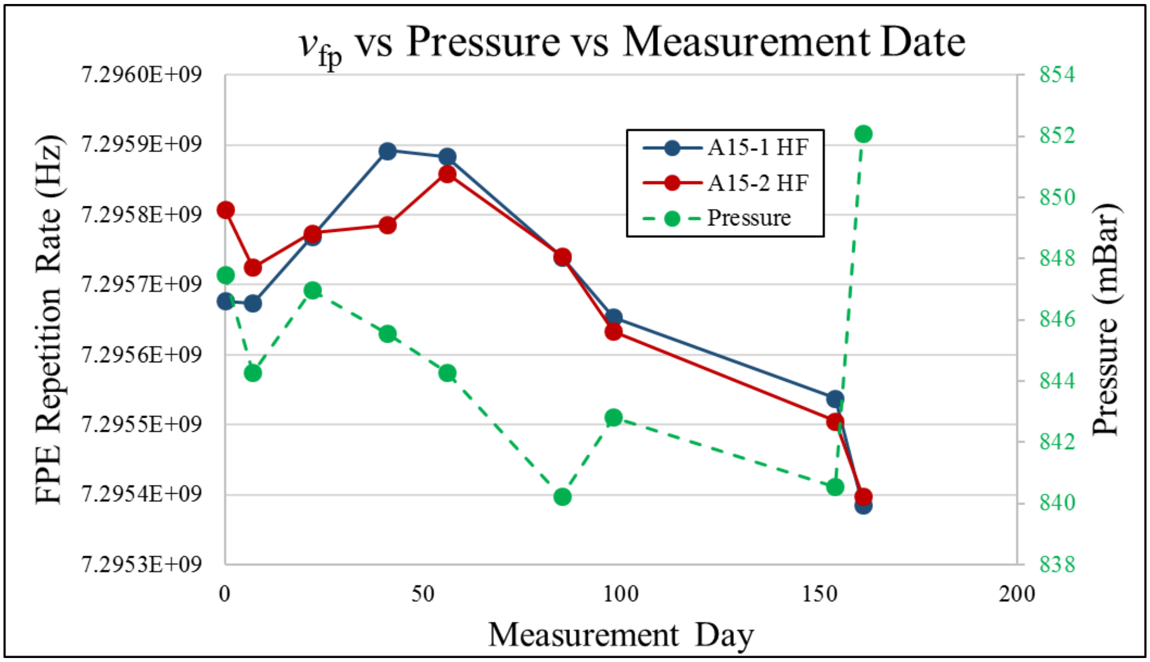

Figure B.4: FPE repetition rate and pressure as measured on days the NH-3 Howitzer sample (A15-4) was measured for refractive index change.

Figure B.3 shows little correlation between humidity and the FPE repetition rate. Although it seems to track the slope between several points at times. Again this suggests that humidity and pressure are not the only factors in the change in repetition rates but the may certainly have a partial correlation.

B.4 Frequency Ratio Delta with Laboratory Environment Changes

The next correlation to consider was the frequency ratio which combines the two separate repetition rates into a ratio. The frequency ratio is more heavily affected by the cavity repetition rate because the cavity repetition rate is affected more by the change in cavity length than the FPE repetition rate. As such, the results shown here are similar in appearance to Figure B.1 and Figure B.2, although, the results are a bit more dramatic. The frequency ratio plots for relative humidity and pressure are shown in Figure B.5 and Figure B.6, respectively.

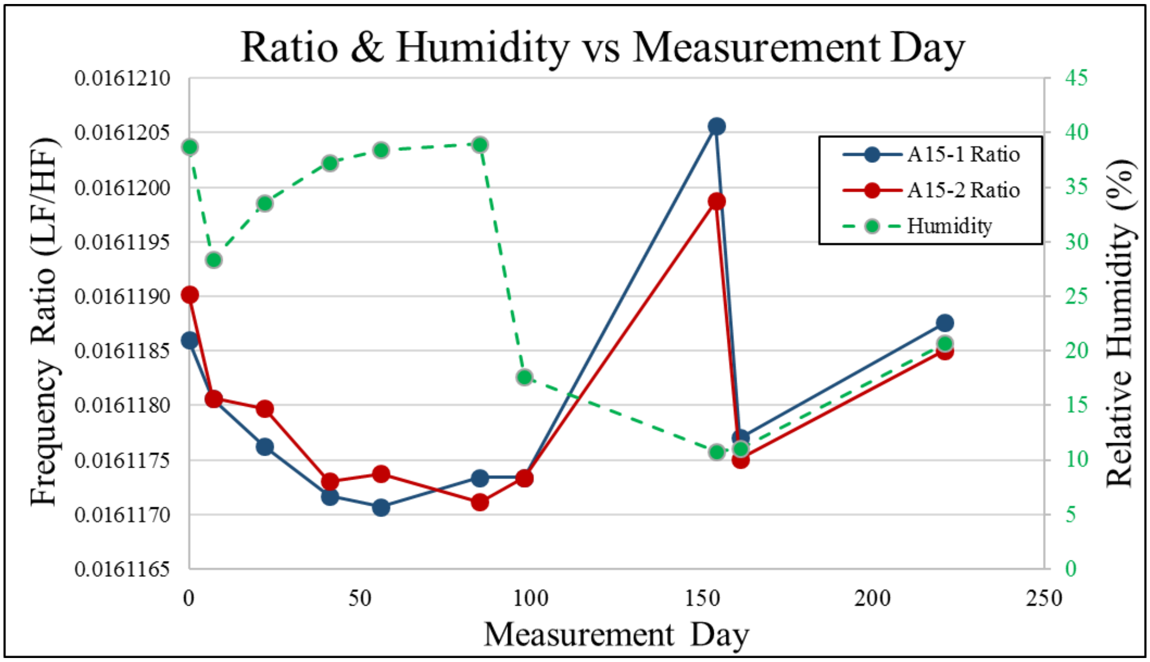

Figure B.5: Frequency ratio and relative humidity as measured on days the NH-3 Howitzer sample (A15-4) was measured for refractive index change.

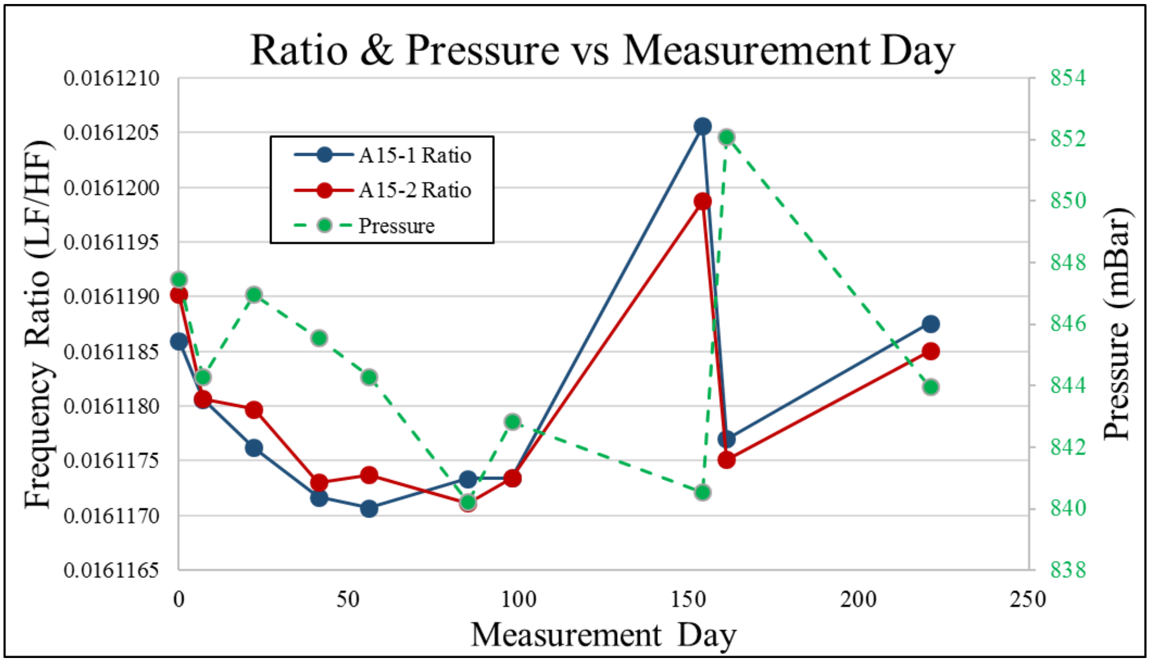

Figure B.6: Frequency ratio and pressure as measured on days the NH-3 Howitzer sample (A15-4) was measured for refractive index change.

Similar to the cavity repetition rate results vs laboratory environment the humidity seems to track inversely with the frequency ratio, however, with the additional day 221 data point added back in a clear direct relationship is seen between day 165 and day 221. The pressure again does not seem to have a correlation through 100 days, however, after the 100 day point there again appears an indirect correlation. Again, there is no definable correlation seen here although these plots certainly seem to suggest that both humidity and pressure have a partial role in the variation that is seen on a day to day basis.

B.5 Frequency Ratio with Air Density and Refractive Index of Air

Due to the nature of the laboratory setup air plays a major role in the determining of the necessary values to measure refractive index change. Considering the role that open-air plays in these measurements the properties of the air should be considered. As humidity, temperature, and pressure have already been considered separately the next step is to use them to calculate larger properties of air such as the air density and the refractive index of the air. The calculation of air density for moist air is a standard calculation from temperature, pressure, and humidity. Calculating refractive index, although, proportional to air density, is a bit more complicated. It is ultimately determined for the purposes of this work by the Edlén Equation [65]. This was completed to produce Figure B.7 and Figure B.8 for air density and refractive index of air, respectively.

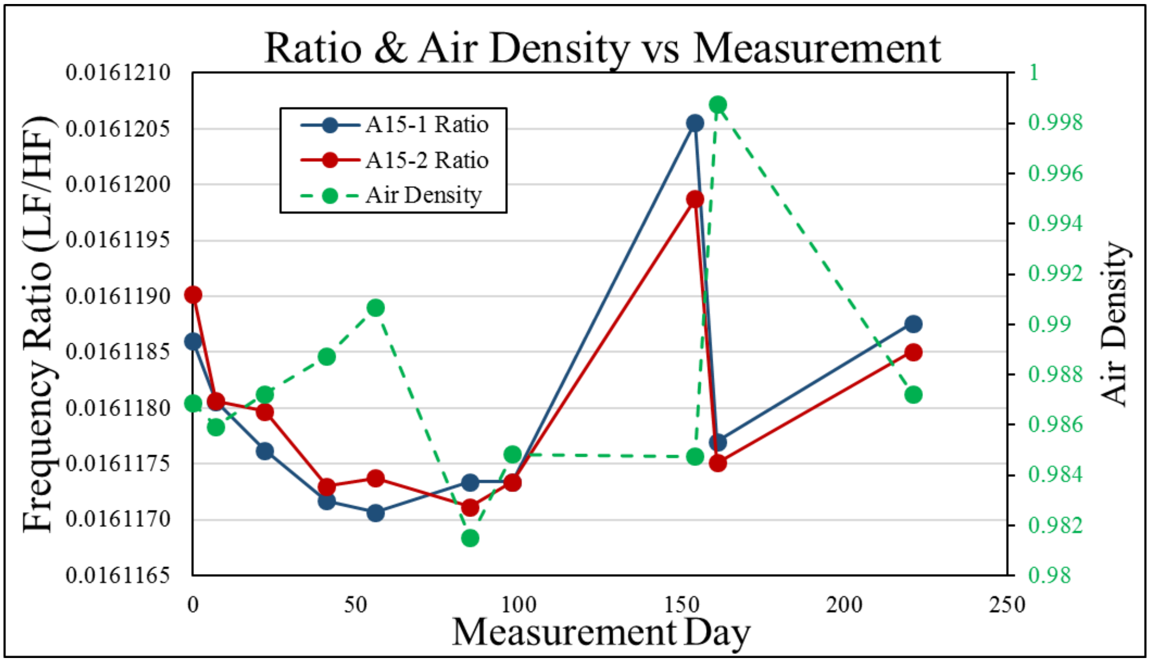

Figure B.7: Frequency ratio and air density as measured on days the NH-3 Howitzer sample (A15-4) was measured for refractive index change.

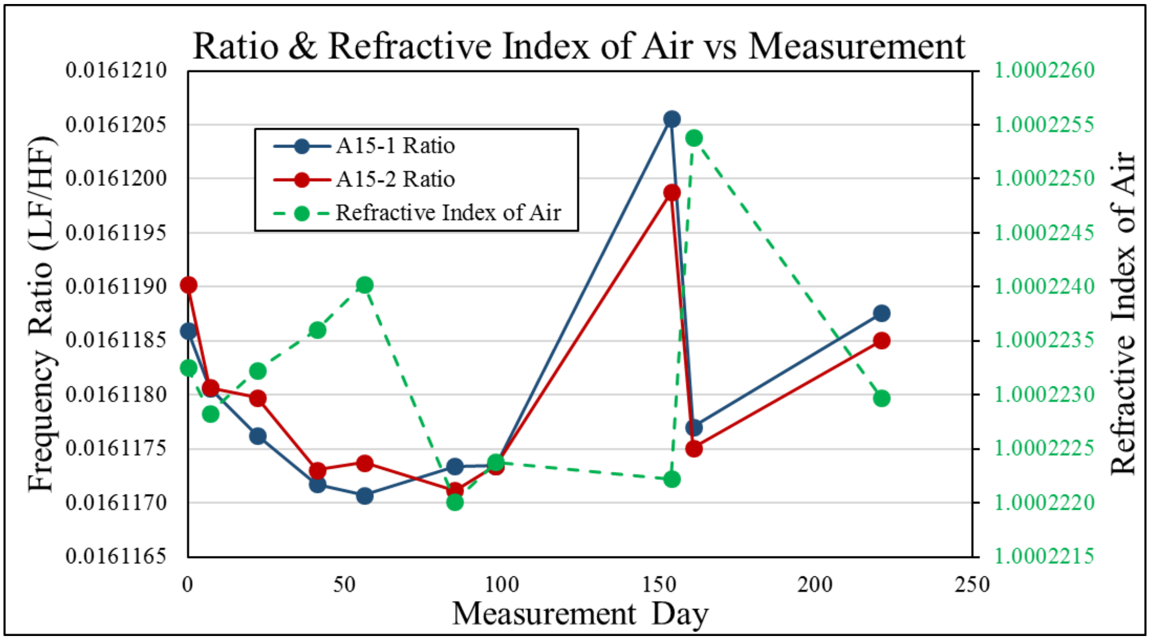

Figure B.8: Frequency ratio and refractive index of air as measured on days the NH-3 Howitzer sample (A15-4) was measured for refractive index change.

Figure B.7 and Figure B.8, while, combining temperature, humidity, and pressure, did not end up providing a comprehensive look at the daily variation in frequency ratio. In some ways by combining the humidity, temperature and pressure the plots seem to more consistently track inversely with the frequency ratio. However, there was still no clear and definitive pattern for which a correction could be adapted. In order to reduce the daily variation and thus the overall uncertainty of this method a more thorough analysis of the causes of the daily variation must be completed.